Supplement of Earth Syst. Sci. Data, 18, 3211–3288, 2026
https://doi.org/10.5194/essd-18-3211-2026-supplement

Open Access Earth System Science Data

Supplement of

Global Carbon Budget 2025

Pierre Friedlingstein et al.

Correspondence to: Pierre Friedlingstein (p.friedlingstein@exeter.ac.uk)

Global Carbon Budget 2025 - Supplementary Information

S.1 Methodology Fossil Fuel CO_2 emissions (E_{FOS})

S.1.1 Cement carbonation

From the moment it is created, cement begins to absorb CO_2 from the atmosphere, a process known as 'cement carbonation'. We estimate this CO_2 sink, from 1931 onwards, as the average of two studies in the literature (Cao et al., 2020; Guo et al., 2021 extended by Huang et al., 2023). The Global Cement and Concrete Association reports a much lower carbonation rate, but this is based on the highly conservative assumption of 0% mortar (GCCA, 2021). Modelling cement carbonation requires estimation of a large number of parameters, including the different types of cement material in different countries, the lifetime of the structures before demolition, of cement waste after demolition, and the volumetric properties of structures, among others (Xi et al., 2016). Lifetime is an important parameter because demolition results in the exposure of new surfaces to the carbonation process. The main reasons for differences between the two studies appear to be the assumed lifetimes of cement structures and the geographic resolution, but the uncertainty bounds of the two studies overlap.

S.1.2 Emissions embodied in goods and services

Our national emission statistics are in line with IPCC reporting guidelines and 'include greenhouse gas emissions and removals taking place within national territory and offshore areas over which the country has jurisdiction' (Rypdal et al., 2006), and are called territorial emission inventories. Consumption-based emission inventories allocate emissions to products that are consumed within a country and are conceptually calculated as the territorial emissions minus the 'embodied' territorial emissions to produce exported products plus the emissions in other countries to produce imported products (Consumption = Territorial – Exports + Imports). Consumption-based emission attribution results (e.g. Davis and Caldeira, 2010) provide additional information to territorial-based emissions that can be used to understand emission drivers (Hertwich and Peters, 2009) and quantify emission transfers by the trade of products between countries (Peters et al., 2011a). The consumption-based emissions have the same global total but reflect the trade-driven movement of emissions between countries in response to human activities.

We estimate consumption-based emissions from 1990 by enumerating the global supply chain using a global model of the economic relationships between economic sectors within and between every country (Andrew and Peters, 2013; Peters et al., 2011b). Our analysis is based on the economic and trade data from the Global Trade and Analysis Project (GTAP; Narayanan et al., 2015), and we make detailed estimates for the years 1997 (GTAP version 5), 2001 (GTAP6), and 2004, 2007, 2011, 2014, and 2017 (GTAP11.0), covering 57 sectors and 141 countries and regions. The detailed results are then extended into an annual time series from 1990 to the latest year of the Gross Domestic Product (GDP) data (typically one year less than the territorial emissions data), using GDP data by expenditure in current exchange rate of US dollars (USD; from the UN National Accounts main Aggregates database; UN, 2025) and time series of trade data from GTAP (based on the methodology in Peters et al., 2011b). We estimate the sector-level CO_2 emissions using the GTAP data and

methodology, add the flaring and cement emissions from our fossil CO_2 dataset, and then scale the national totals (excluding bunker fuels) to match the emission estimates from the carbon budget. We do not provide a separate uncertainty estimate for the consumption-based emissions, but based on model comparisons and sensitivity analysis, they are unlikely to be significantly different than for the territorial emission estimates (Peters et al., 2012b).

S.1.3 Uncertainty assessment for E_{FOS}

We estimate the uncertainty of the global fossil CO_2 emissions at ±5% (scaled down from the published ±10 % at ±2σ to the use of ±1σ bounds reported here; Andres et al., 2012). This is consistent with a more detailed analysis of uncertainty of ±8.4% at ±2σ (Andres et al., 2014) and at the high-end of the range of ±5-10% at ±2σ reported by (Ballantyne et al., 2015). This includes an assessment of uncertainties in the amounts of fuel consumed, the carbon and heat contents of fuels, and the combustion efficiency. While we consider a fixed uncertainty of ±5% for all years, the uncertainty as a percentage of emissions is growing with time because of the larger share of global emissions from emerging economies and developing countries (Marland et al., 2009). Generally, emissions from mature economies with good statistical processes have an uncertainty of only a few per cent (Marland, 2008), while emissions from strongly developing economies such as China have uncertainties of around ±10% (for ±1σ; Gregg et al., 2008; Andres et al., 2014). Uncertainties of emissions are likely to be mainly systematic errors related to underlying biases of energy statistics and to the accounting method used by each country.

S.1.4 Growth rate in emissions

We report the annual growth rate in emissions for adjacent years (in percent per year) by calculating the difference between the two years and then normalising to the emissions in the first year: $(E_{FOS}(t_0+1)-E_{FOS}(t_0))/E_{FOS}(t_0)\times 100\%$. We apply a leap-year adjustment where relevant to ensure valid interpretations of annual growth rates. This affects the growth rate by about 0.3% yr^{-1} (1/366) and causes calculated growth rates to go up approximately 0.3% if the first year is a leap year and down 0.3% if the second year is a leap year.

The relative growth rate of E_{FOS} over time periods of greater than one year can be rewritten using its logarithm equivalent as follows:

$$\frac{1}{E_{FOS}}\frac{dE_{FOS}}{dt} = \frac{d(lnE_{FOS})}{dt} \quad \text{(S1)}$$

Here we calculate relative growth rates in emissions for multi-year periods (e.g. a decade) by fitting a linear trend to $ln(E_{FOS})$ in Eq. (S1), reported in percent per year. We define the average growth rate over a decadal period to include the growth in the first year. For example, when calculating the growth rate of 2000-2009, we include the growth rate in the year 2000, thus the regression is for the years 1999-2009, otherwise the growth from 1999-2000 would not be included in either 1990-1999 or 2000-2009 time periods.

S.1.5 Emissions projection for 2025

To gain insight on emission trends for 2025, we provide an assessment of global fossil CO_2 emissions, E_{FOS}, by combining individual assessments of emissions for China, USA, the EU India, and Japan (four of the six countries/regions with the largest emissions), and the rest of the world.

The methods are specific to each country or region, as described in detail below.

China: We rely primarily on the National Bureau of Statistics' (NBS) Statistical Communique, published in late February with the first official data for the full year of 2025. Specifically, we use growth rates for coal, oil, and natural gas derived from the information on energy shares. For cement we use annual data from the NBS.

USA: We use emissions estimated by the U.S. Energy Information Administration (EIA) in their Short-Term Energy Outlook (STEO) for emissions from fossil fuels (EIA, 2025). We combine this with our estimate of emissions from cement production using the monthly U.S. cement clinker production data from USGS for January-November 2025, assuming changes in clinker production over the first part of the year apply throughout the year.

India: We use monthly emissions estimates for India updated from Andrew (2020b) through December 2025. These estimates are derived from many official monthly energy and other activity data sources to produce direct estimates of national CO_2 emissions, without the use of proxies.

EU: We use a refinement to the methods presented by Andrew (2021), deriving emissions from monthly energy data reported by Eurostat. Some data gaps are filled using data from the Joint Organisations Data Initiative (JODI, 2025). Sub-annual cement and cement-clinker production data are limited, but data for Germany, Poland and Spain, the three largest producers, are available, along with production indices for Italy and France. For all categories data are available through December 2025

Japan: We use a newly developed dataset of monthly emissions derived from official monthly activity data including energy flows and industrial production statistics (Kunimitsu & Andrew, *in preparation*). This gives robust estimates through December.

International transport: Given the divergence in behaviour of international shipping from countries' emissions since the COVID-19 pandemic, we project international bunkers separately. For aviation we use sub-annual data from the OECD (Clarke et al., 2022) extended using data on the number of flights from Airportia (https://airportia.com/flights-monitor/). For international shipping we combine information from the OECD's estimate of global shipping (Clarke et al., 2023), ShipAndBunker's collation of bunker sales data from the world's 20 top bunkering ports (https://shipandbunker.com/bi/bunker-volumes), VesselBot's estimates of container-ship emissions (https://www.vesselbot.com/resources/), and MarineBenchmark's estimates of global shipping emissions (https://www.marinebenchmark.com/insights/); all four of these sources agree qualitatively.

Rest of the world: For oil and gas emissions, we use the global oil demand forecast (EIA) and global gas demand forecast (IEA) and subtract the other regions explicitly modelled, and estimate uncertainty as the maximum absolute difference over the period available for such forecasts using the specific monthly editions of the respective forecasts. For coal and cement, we use the close relationship between the growth in GDP and the growth in emissions (Raupach et al., 2007) to project emissions for the current year. This is based on a simplified Kaya Identity, whereby E_{FOS} (GtC yr^{-1}) is decomposed by the product of GDP (USD yr^{-1}) and the fossil fuel carbon intensity of the economy (I_{FOS}; GtC USD^{-1}) as follows:

$$E_{FOS} = GDP \times I_{FOS} \quad \text{(S2)}$$

Taking a time derivative of Equation (S2) and rearranging gives:

$$\frac{1}{E_{FOS}}\frac{dE_{FOS}}{dt} = \frac{1}{GDP}\frac{dGDP}{dt} + \frac{1}{I_{FOS}}\frac{dI_{FOS}}{dt} \quad \text{(S3)}$$

where the left-hand term is the relative growth rate of E_{FOS}, and the right-hand terms are the relative growth rates of GDP and I_{FOS}, respectively, which can simply be added linearly to give the overall growth rate.

The I_{FOS} is based on GDP in constant PPP (Purchasing Power Parity) from the International Energy Agency (IEA) up to 2017 (IEA/OECD, 2019) and extended using the International Monetary Fund (IMF) growth rates through 2024 (IMF, 2024). Interannual variability in I_{FOS} is the largest source of uncertainty in the GDP-based emissions projections. We thus use the standard deviation of the annual I_{FOS} for the last decade as a measure of uncertainty, reflecting a $\pm 1\sigma$ as in the rest of the carbon budget.

World: The global total is the sum of each of the countries and regions.

S.1.6 Carbon Monitor

Refinement of near-real-time daily CO_2 estimates: Building on our previously documented methodology, we refine our estimates by establishing a new baseline for emissions and incorporating data from additional countries. First, instead of using a single baseline year (2019), the baseline emissions now cover the 2019–2021 period. This update mainly relies on the national greenhouse gas inventories (NGHGIs) submitted to UNFCCC, with IPCC sector emissions systematically mapped to the Carbon Monitor sectors. Second, we update the estimation for the power and industry sectors in the Rest of the World (ROW) region. To approximate emission changes in ROW, we use the average emission variations observed in countries with available data.

S.2 Methodology CO_2 emissions from land-use, land-use change and forestry (E_{LUC})

The net CO_2 flux from land-use, land-use change and forestry (E_{LUC}, called land-use change emissions in the rest of the text) includes CO_2 fluxes from deforestation, afforestation, logging and forest degradation (including harvest activity), shifting cultivation (cycle of cutting forest for agriculture, then abandoning), regrowth of forests following wood harvest or abandonment of agriculture, peat burning, and peat drainage. Land-management activities are only partly included in our land-use change emissions estimates (Table S1). Some land-use change and land-management activities cause emissions of CO_2 to the atmosphere, while others remove CO_2 from the atmosphere. E_{LUC} is the net sum of emissions and removals due to all anthropogenic activities considered. Our annual estimates for 1959-2024 are provided as the average of results from three bookkeeping models (Supplement S.2.2): the Bookkeeping of Land Use Emissions model (BLUE; Hansis et al., 2015), the compact Earth system model OSCAR (Gasser et al., 2020), and the Land-Use Change Emissions model (LUCE; Qin et al., 2024). Peat emissions are added from external datasets (Supplement S.2.2). BLUE and OSCAR are updated with new land-use forcing data covering the time period until 2024 (Supplement S.2.1). E_{LUC} data are extrapolated to provide a projection for 2025 (Supplement S.2.6). In addition, we use results from Dynamic Global Vegetation Models (DGVMs; see Supplement S.2.3 and Table 4) to help quantify the uncertainty in E_{LUC} (Supplement S.2.5), and thus better characterise the robustness of annual estimates and trends. In this budget, we follow the E_{LUC} definition as used by global carbon cycle models, which counts fluxes

due to environmental changes on managed land towards S_{LAND}, as opposed to the national greenhouse gas inventories (NGHGIs) under the UNFCCC, most of which include them in E_{LUC} and thus often report smaller land-use emissions (Grassi et al., 2023). Following the methodology of Grassi et al. (2023), we provide harmonised estimates of the two approaches further below (Supplement S.2.4).

S.2.1 Land-Use and Land Use Change Datasets

Bookkeeping models and DGVMs use the harmonised land-use change data LUH2-GCB2025 covering the period 850-2024 as input to estimate E_{LUC} (an update to the previously released LUH2 v2h dataset; Hurtt et al., 2017; Hurtt et al., 2020). LUH2-GCB2025 provides land-use change data at 0.25° spatial resolution based on data from the Food and Agriculture Organization of the United Nations (FAO, 2025a) as well as the HYDE3.5 dataset (Klein Goldewijk et al., 2017a, 2017b), considering subgrid-scale transitions between primary forest, secondary forest, primary non-forest, secondary non-forest, cropland, pasture, rangeland, and urban land (Hurtt et al., 2020; Chini et al., 2021).

S.2.1.1 HYDE3.5

The HYDE3.5 cropland/grazing/urban land dataset is constrained by FAO country-level statistics (FAO, 2025a; bulk download February 2025) for the years 1961-2023. HYDE uses satellite imagery from ESA-CCI from 1992-2018 for more detailed yearly allocation of cropland and grazing land, with the ESA-CCI area data scaled to match the FAO annual totals at country-level. The 2018 map is also used for the 2019-2024 period. The original 300 metre spatial resolution data from ESA is aggregated to a 5 arc minute resolution according to the classification scheme as described in Klein Goldewijk et al. (2017a).

As in GCB2024 we replace the FAO timeseries for China, based on province-level area totals from Yu et al. (2022) for the 1900-2019 period. For Brazil and Indonesia, we replace the full FAO time series with time series based on MapBiomas state-level area totals (available for 1985-2023 for Brazil and 2000-2023 for Indonesia) (MapBiomas Brasil, Souza et al., 2020, MapBiomas Indonesia). For Indonesia, MapBiomas replaces cropland only, which includes oil palm plantations as does FAO, while grazing land is taken from FAO. For the pre-1985 period, the per-capita cropland area in 1985 is calculated for each state of Brazil (based on MapBiomas) and scaled with the historical population development for each state of Brazil. A similar methodology is adopted for land cover change information from MapBiomas for Indonesia.

S.2.1.2 LUH2-GCB2025

LUH2-GCB2025 is an update of the comprehensive harmonised land-use data set version 2 (Hurtt et al., 2020), which includes fractional data on primary and secondary forest vegetation, as well as all underlying transitions between land-use states (Hurtt et al., 2011, 2017, 2020; Chini et al., 2021; Table S1). LUH2-GCB2025 covers the period 850-2024 and consists of 0.25° fractional areas of land-use states and all transitions between those states, including an updated wood harvest reconstruction and updated representation of shifting cultivation, crop rotation, and management information including irrigation and fertiliser application. The land-use states include five different crop types in addition to splitting grazing land into managed pasture and rangeland. Wood harvest patterns are constrained with Landsat-based tree cover loss data (Hansen et al. 2013).

The complete LUH2-GCB2025 forcing timeseries is updated to use the new HYDE3.5 land-use and population data. LUH2-GCB2025 uses the 2025 FAO national wood harvest production data for 1961-2023 along with the new HYDE3.5 population data to reconstruct the historical wood harvest time-series. Wood production data is linearly extended to the year 2024. In addition, the land-use time series is extended beyond the years that are directly informed by data in HYDE (e.g., beyond 2023 for those countries based on FAO country-level statistics) to include land-use states up to and including the year 2025 (and land-use transitions during the year 2024). A simple extension of the previous 5-year trend for each gridcell is applied. Updates in the land-use forcing are shown in Figure S1 in comparison to LUH2-GCB2023 and LUH2-GCB2024.

LUH2-GCB2025 provides a distinction between rangelands and pasture, based on inputs from HYDE. DGVM/BM groups in the past have requested more information on whether natural vegetation is lost in conversion to pasture or rangelands. LUH2 guidelines suggest that rangelands are established after clearing of forests and managed pastures are established after clearing of all other natural vegetation. Therefore, (1) rangeland establishment in forests is assumed to transform forests to grasslands, (2) rangeland establishment in non-forest primary vegetation degrades primary to secondary vegetation, and (3) rangeland establishment in non-forest secondary vegetation has no effect (e.g., browsing on shrubland; Ma et al., 2020). In the bookkeeping model BLUE, this case distinction is implemented based on a forest mask provided with LUH2-GCB2021.

S.2.2 Bookkeeping models

CO_2 emissions and removals from land-use change are calculated by three bookkeeping models. These are based on the original bookkeeping approach of Houghton (2003), which keeps track of the carbon stored in vegetation and soils before and after a land-use change event (transitions between various natural vegetation types, croplands, and pastures). Literature-based response curves describe the decay of vegetation and soil carbon, including carbon transfer to product pools of different lifetimes, as well as carbon uptake due to regrowth. In addition, the bookkeeping models represent long-term degradation of primary forest as lowered standing vegetation and soil carbon stocks in secondary forests and include forest management practices such as wood harvests.

All three GCB2025 bookkeepings models use transient carbon densities to estimate E_{LUC}, i.e., they consider the effects of environmental changes, such as atmospheric CO_2 increase and impacts of climate change, on vegetation and soil carbon densities. In the past, only the OSCAR estimates were based on transient carbon densities while the other bookkeeping models followed the original bookkeeping approach and used static carbon densities. The consideration of environmental changes to estimate E_{LUC} does not interfere with S_{LAND} estimates. In fact, considering environmental effects for E_{LUC} estimates and correcting S_{LAND} for the bias from Replaced Sinks and Sources (RSS; see Section S.4.1) delivers a conceptually consistent terrestrial carbon budget (Pongratz et al. 2014; Dorgeist et al., 2024) correcting for biases present in previous GCB assessments. OSCAR already includes the transient response in its E_{LUC} estimates (Gasser and Ciais, 2013; Gasser et al., 2020). The static carbon densities of BLUE and LUCE were both updated using time-varying data from DGVM following the method described in Dorgeist et al. (2024). Vegetation and soil carbon densities were used to derive scaling factors, benchmarked to their 1980 values. These scaling factors are applied to the original carbon densities of BLUE and LUCE. The updated carbon densities maintain the original spatial resolution but with temporal

changes following DGVMs. While this approach does not resolve interannual variability in environmental conditions - e.g., natural fires, droughts, or windthrow are not reflected in carbon densities in the year they occur - the carbon densities represent the average cycle of natural disturbances, as they are based on direct observations or literature. As the transient dynamics of the carbon densities are derived from DGVMs, also changes in disturbance regimes are accounted for, to the extent captured by the DGVMs.

The bookkeeping models differ in (1) computational units (spatially explicit treatment of land-use change at 0.25° resolution for BLUE and LUCE, country-level for OSCAR), (2) processes represented (see Table S1), and (3) carbon densities assigned to vegetation and soils for different types of vegetation (literature-based for BLUE, calibrated to DGVMs for OSCAR, mainly literature-based but additionally considering the impact of land cohort age on secondary land carbon stocks for LUCE). All three bookkeeping models include subgrid-scale transitions between all vegetation types, and they allocate pasture transitions proportionally to all natural vegetation that exists in a grid cell.

The three bookkeeping estimates used in this study differ with respect to the land-use change data used to drive the models. BLUE and LUCE use the harmonised land-use change data LUH2-GCB2025. OSCAR was run with both LUH2-GCB2025 and data from the Forest Resource Assessment (FRA) of FAO (using data from FAO, 2020), which provides statistics on forest-area change and management at intervals of five years. The data is based on country reporting to FAO and may include remote-sensing information in more recent assessments. Changes in land use other than forests are based on annual, national changes in cropland and pasture areas reported by FAO (FAO, 2021). FAO/FRA data were linearly extrapolated to 2024 using their 2015-2020 trends. The best-guess OSCAR estimate used in our study is a combination of results for LUH2-GCB2025 and FAO/FRA land-use data and a large number of perturbed parameter simulations weighted against a constraint (the cumulative S_{LAND} over 1960-2023 of last year's GCB).

Bookkeeping models do not directly capture carbon emissions from the organic layers of drained peat soils nor from peat fires. Particularly the latter can create large emissions and interannual variability due to synergies of land-use and climate variability in equatorial Southeast Asia, especially during El-Niño events. We add peat fire emissions based on the Global Fire Emission Database (GFED4s; van der Werf et al., 2017) to the bookkeeping models' output. Peat fire emissions are calculated by multiplying the mass of dry matter emitted by peat fires with the carbon emission factor for peat fires indicated in the GFED4s database. Emissions from deforestation and degradation fires used to derive the 2025 E_{LUC} projection (Supplement S.2.6) are calculated analogously. The satellite-derived GFED4s estimates of peat fire emissions start in 1997. For the previous years, we follow the approach by Houghton and Nassikas (2017), which linearly ramps up from zero emissions in 1980 to 0.04 GtC yr^{-1} in 1996, reflecting the onset of major clearing of peatlands in equatorial Southeast Asia in the 1980s.

We also add peat drainage emissions, combining estimates from three spatially explicit datasets. We employ peat drainage emissions 1990–2022 from croplands and grasslands provided by FAO (Conchedda and Tubiello, 2020; FAO, 2025b), peat drainage emissions 1700–2010 from simulations with the DGVM ORCHIDEE-PEAT (Qiu et al., 2021), and peat drainage emissions 1701–2024 from simulations with the DGVM LPX-Bern v1.5 (Lienert and Joos, 2018; Müller and Joos, 2021), the latter applying the updated LUH2-GCB2025 forcing as also used by BLUE, OSCAR, LUCE, and the DGVMs. The LPX-Bern simulations start from a transient run over the last deglaciation (-20,050 to 1700 AD) following Müller and Joos (2020) and are forced by changes in

climate, atmospheric CO_2, nitrogen deposition/input, and land-use changes. Simulations were done with and without prescribing land-use changes since 1700 AD. The difference between the simulations represents anthropogenic peat drainage emissions. To account for internal variability, we used the median peat drainage emissions from a 10-member ensemble. In LPX-Bern, peat carbon is stored in (i) active peatlands, (ii) former peatlands ("natural"), and (iii) former peatlands under anthropogenic use. We average the two CO_2 emission cases from Müller and Joos (2021), assuming that half the peat carbon is lost immediately to the atmosphere after transformation from active to former peatland, while the rest decays slowly, depending on local temperature and soil moisture. The LPX-Bern peat drainage emissions show a very high emission peak in Russia in 1959 followed by very low emissions in 1960. This peak can be attributed to an artefact in the HYDE dataset, which was corrected for Brazil and the Democratic Republic of the Congo in GCB2022 (Friedlingstein et al. 2022b) but remains for Russia where it strongly impacts the LPX-Bern peat drainage estimates in 1959 and 1960. To correct for this unrealistic peak, we replace the LPX-Bern peat drainage emissions in Russia in 1959 and 1960 by the average of the estimates in 1958 and 1961. The FAO peat drainage emissions are extrapolated to 1850-2024 by keeping the post-2022 emissions constant at 2022 levels, by linearly increasing tropical peat drainage emissions between 1980 and 1990 starting from 0 GtC yr^{-1} in 1980 (consistent with Houghton and Nassikas, 2017), and by keeping pre-1990 emissions from the often old, drained areas of the extra-tropics constant at 1990 emission levels. The ORCHIDEE-PEAT data are extrapolated to 2011-2024 by replicating the average emissions in 2000-2010 (pers. comm. C. Qiu). Further, ORCHIDEE-PEAT only provides peat drainage emissions north of 30°N, and thus we fill the regions south of 30°N by the average peat drainage emissions from FAO and LPX-Bern. The final peat drainage emissions are calculated as the average of the estimates from the three different peat drainage datasets.

We provide a split of net E_{LUC} into component fluxes to give more insight into the drivers of net E_{LUC} and to better identify reasons for divergence between bookkeeping estimates. This split distinguishes between emissions from deforestation (including due to shifting cultivation), removals from forest (re-)growth (including regrowth in shifting cultivation cycles), fluxes from wood harvest and other forest management (including emissions from slash decay in forests, emissions from product decay following wood harvesting, and removals from regrowth after wood harvesting), emissions from peat drainage and peat fires, and emissions and removals associated with all other land-use transitions. Additionally, we split deforestation emissions into emissions from permanent deforestation and emissions from deforestation in shifting cultivation cycles. Similarly, we split removals from forest (re-)growth into forest (re-)growth due to re-/afforestation and forest regrowth in shifting cultivation cycles. This distinction is insightful with regard to the levers on the reduction of net emissions: as deforestation for shifting cultivation is only temporary, the associated CO_2 emissions cannot easily be avoided without compromising the CO_2 removals from regrowth in shifting cultivation cycles. By contrast, permanent deforestation is typically not directly related to re-/afforestation. Stopping deforestation for permanent agricultural expansion and increasing the forest area provide two independent levers for net emissions reduction.

E_{LUC} data are provided as global sums, as spatially explicit estimates at 0.25° spatial resolution (i.e., the native LUH2-GCB2025 resolution), and for 199 countries (based on the list of UNFCCC parties). Spatially explicit E_{LUC} estimates for BLUE and LUCE are directly available at 0.25°. For OSCAR, the country-level estimates were scaled to 0.25° based on the patterns of gross emissions and gross removals in BLUE (following the methodology of Schwingshackl et al., 2022). The global net E_{LUC} values indicated in the manuscript are the sum

of E_{LUC} estimates from bookkeeping models, peat drainage emissions (average of FAO, LPX-Bern, and ORCHIDEE-PEAT), and peat fire emissions (from GFED4s). Annual E_{LUC} estimates from 1850 onwards are calculated as the average of the estimates from BLUE, OSCAR, and LUCE plus emissions from peat fires and peat drainage. For the cumulative numbers starting in 1750, emission estimates between 1750-1850 are added based on the average of four earlier publications (30 ± 20 GtC 1750-1850, rounded to nearest 5; Le Quéré et al., 2016). The gridded net E_{LUC} estimates of BLUE, LUCE, and OSCAR are averaged, and the gridded estimates of peat drainage emissions and of peat fire emissions are added. Country-level estimates for the gridded datasets (BLUE, LUCE, LPX-Bern, ORCHIDEE-PEAT, GFED4s) are calculated based on a country map from Eurostat (Eurostat, 2024), which was remapped to 0.25°. In case multiple countries are present in a 0.25° grid cell, the E_{LUC} estimates are allocated proportional to each country's land fraction in that grid cell.

S.2.3 Dynamic Global Vegetation Models (DGVMs)

All DGVMs represent processes of vegetation growth and mortality, as well as decomposition of dead organic matter associated with natural cycles, and include the vegetation and soil carbon response to increasing atmospheric CO_2 concentration, to climate variability and to climate change. Most models explicitly simulate the coupling of carbon and nitrogen cycles and account for atmospheric N deposition and N fertilisers (Table S1). The DGVMs are independent from the other budget terms except for their use of atmospheric CO_2 concentration to calculate the fertilisation effect of CO_2 on plant photosynthesis. Land-use change CO_2 emissions are also estimated by an ensemble of 22 DGVMs. The DGVMs account for deforestation and regrowth, the most important components of E_{LUC}, but they do not represent all processes resulting directly from human activities on land (Table S1).

All DGVMs use the LUH2-GCB2025 dataset as input to estimate the land use change CO_2 fluxes. which includes the HYDE cropland/grazing land dataset (Klein Goldewijk et al., 2017a, 2017b), and some additional information on land-use transitions, land-use management activities and wood harvest. DGVMs that do not simulate subgrid-scale transitions (i.e., those estimating net land-use emissions; see Table S1) use the HYDE information on agricultural area change. DGVMs implement land-use change in different ways (e.g., an increased cropland fraction in a grid cell can either be at the expense of grassland, shrubs, or forest, the latter resulting in deforestation; land cover fractions of non-agricultural land differ between models). Similarly, model-specific assumptions are applied to convert deforested biomass or deforested area, and other forest product pools into carbon, and different choices are made regarding the allocation of rangelands as natural vegetation or pastures.

As a criterion for inclusion in this carbon budget, we only retain models that simulate a positive E_{LUC} during the 1990s, as assessed in the IPCC AR4 (Denman et al., 2007) and AR5 (Ciais et al., 2013). All DGVMs met this criterion.

S.2.4 Translation between NGHGIs and E_{LUC}

Land-use emissions estimates from bookkeeping models and from national GHG Inventories (NGHGIs) show a large gap (Figure 8 and Table S11). This gap is due to different approaches for calculating anthropogenic CO_2 fluxes related to land-use change and land management (Grassi et al. 2018). Land sinks due to environmental

changes on managed lands are treated as non-anthropogenic in the GCB assessments, while they are generally considered as anthropogenic in NGHGIs ("indirect anthropogenic fluxes"; IPCC, 2006). Building on previous studies (Grassi et al. 2021), we implement a translation approach that adds the DGVM estimates of CO_2 fluxes due to environmental change in managed forest areas (part of S_{LAND}) to the E_{LUC} estimate from bookkeeping models. The translated E_{LUC} values are expected to be conceptually more comparable to NGHGI estimates.

LULUCF data from NGHGIs are those in the LULUCF data hub V3.1 (https://zenodo.org/records/17153438). They are collected and processed based on country data submitted to the UNFCCC, as described in detail by Melo et al. (2025). While Annex I countries report a complete time series 1990-2023, gap-filling was applied for many Non-Annex I countries through linear interpolation between two points and/or through extrapolation backward (till 2000) and forward (till 2023) using the single closest available data. For this assessment, the NGHGI estimates of the year 2024 are assumed to be equal to those of 2023. NGHGI data include all CO_2 fluxes from land considered managed (forest land, cropland, grassland, wetlands, settlements, and other land), changes among these land categories, and emissions from organic soils (i.e., from peat drainage), from harvested wood products and from fires. Almost all Annex I countries report all land uses, whereas many non-Annex I countries report only on deforestation and forest land, and only few countries report on other land uses. Similarly, Annex I countries typically report most carbon pools (biomass, dead organic matter, soil), whereas non-biomass pools are reported less frequently by non-Annex I countries.

In most cases, NGHGIs include most of the natural response to recent environmental changes because they use direct observations (e.g., national forest inventories) that do not allow separating direct and indirect anthropogenic effects (IPCC, 2006; Grassi et al., 2018). These effects are considered to be particularly relevant in forests (Grassi et al., 2023). To improve comparability with NGHGIs, the natural land sink (S_{LAND}) in managed forests (only including carbon fluxes due to environmental change and excluding land-use change fluxes) is added to the results from bookkeeping models to make them comparable to LULUCF estimates from NGHGIs (Figure 8).

To determine S_{LAND} in managed forests, the following steps were taken (Grassi et al., 2023): Spatially gridded data of natural forest NBP were obtained from DGVMs using the S2 simulation from the TRENDY-GCB2025 dataset (see Supplement S.4.1). For those DGVMs that disaggregate their NBP results by plant functional type (PFT), NBP from forest PFTs was used. For all other DGVMs, the total NBP of a grid cell was used for all grid cells containing forest. Since S2 simulations use pre-industrial forest cover masks that are at least 20% larger than today's forest (Hurtt et al. 2020), we corrected this NBP by a ratio between observed forest cover (based on Hansen et al. 2013) and prescribed forest cover (from DGVMs). Results were then masked using a proxy map of managed forest (Rossi et al., 2024) for different years (2000, 2010, and 2020). This map is based on global Earth observation-derived data of tree cover (Hansen et al. 2013) and country-based information on managed and unmanaged forests. Several countries indicate that all forest is managed (e.g., China, India, Australia, most European countries) and a few provide geospatial polygons of managed forest areas (Brazil, Canada, USA). However, some countries report only the total extent of managed and unmanaged forest without maps being available (e.g., Russia) or do not provide specific information on managed land (most developing countries). In these cases, maps of intact and non-intact forest areas (Potapov et al. 2017) were used as a proxy of non-

managed and managed forests in NGHGIs, respectively (Grassi et al. 2023). The detailed DGVM processing steps are explained in Alkama (2022).

We also use gridded net land flux estimates from 14 atmospheric inversion systems (Table S4) to get an additional estimate of land-use fluxes on managed land. We applied a correction for riverine transport (see Supplement S.5.1.) and multiplied the resulting values with the fraction of managed land in each grid cell for each inversion system. For this purpose, we used masks of managed land from Grassi et al. (2023) available for the years 1994, 2002, 2010, and 2016. We linearly interpolated the masks in time and replicated the 2016 mask in the years 2017-2024. Subsequently, we applied another correction for lateral transport due to international wood and crop trade (data from Deng et al. 2024). The obtained values are summed globally and compared to the NGHGI estimates and the translated net E_{LUC} estimates.

Figure 8 and Table S11 show the resulting translation of global carbon cycle models' land flux definitions to that of the NGHGIs (discussed in Section 3.2.2). For comparison we also show LULUCF estimates from the FAOSTAT database (FAO, 2025c), which include emissions from net forest conversion and fluxes on forest land (Tubiello et al., 2025) as well as CO_2 emissions from peat drainage (Conchedda and Tubiello, 2020) and peat fires (Prosperi et al., 2020). The forest land stock change estimates use as input the most recent FRA 2025 data. The FAOSTAT data shows small net removals of -0.01 GtC yr^{-1} averaged over 2015-2024, in contrast to the removals of -1.05 GtC yr^{-1} estimated by the gap-filled NGHGI data (Table S11). The difference between these two estimates reflects different scopes, methods, and input data. The NGHGI focus lies on estimating carbon fluxes from land use, land-use change, and forestry using either a gain-loss or stock-difference approach (depending on the country) as defined by IPCC guidelines. The FAOSTAT estimate generally includes CO_2 fluxes in all forests (managed and unmanaged; depending on the country) using a stock-difference approach based on FAO's Forest Resource Assessment whose focus is on area and biomass stocks, and emissions for drainage and fires in organic soils. In particular, the NGHGI data include a larger forest sink for non-Annex 1 countries resulting from a more complete coverage of non-biomass carbon pools and non-forest land uses (Grassi et al., 2022; Tubiello et al., 2025).

S.2.5 Uncertainty assessment for E_{LUC}

Differences between the bookkeeping models and DGVMs originate from three main sources: different methodologies, different underlying land-use/land-cover datasets, and different processes represented (Table S1). We examine both the results from bookkeeping models and from DGVMs and use the resulting variations to characterise the uncertainty in E_{LUC}.

Despite the existing differences, the E_{LUC} estimate from the DGVM multi-model mean is consistent with the average of the emissions from the bookkeeping models (Table 5). However, there are large differences among individual DGVMs (standard deviation at ~0.5 GtC yr^{-1}; Table 5) and between the bookkeeping estimates (standard deviation at 0.3 GtC yr^{-1} for cumulative emissions in 1850-2024). A factorial analysis of differences between BLUE and the bookkeeping model H&N2017 (Houghton & Nassikas, 2017), which was part of the bookkeeping ensemble in previous GCBs, attributed them particularly to differences in carbon densities between primary and secondary vegetation (Bastos et al., 2021). Earlier studies additionally showed the relevance of the different land-use forcing as applied (in updated versions) also in the current study (Gasser et al., 2020).

Ganzenmüller et al. (2022) showed that E_{LUC} estimates from BLUE are substantially smaller when the model is driven by a high-resolution land-use dataset (HILDA+). They identified shifting cultivation and the way it is implemented in LUH2 as a main reason for this divergence. They further showed that a higher spatial resolution reduces the estimates of both gross emissions and gross removals because successive transitions are not adequately represented at coarser resolution, which has the effect that—despite capturing the same extent of transition areas—overall less area remains pristine at the coarser compared to the higher resolution.

The uncertainty in E_{LUC} of ±0.7 GtC yr^{-1} reflects our best value judgement that there is at least 68% chance (±1σ) that the true land-use change emissions lie within the given range, for the range of processes considered here. Prior to the year 1959, the uncertainty in E_{LUC} is taken from the standard deviation of the DGVMs. We assign low confidence to the annual estimates of E_{LUC} because of the inconsistencies among estimates and because of the difficulties to quantify some of the processes with DGVMs.

S.2.6 Land-use emissions projection for 2025

We project the 2025 land-use emissions based on anomalies in emissions from peat fires and tropical deforestation and degradation fires from GFED4s. The GFED4s estimates for 2025 are as of October 15, 2025. Since the E_{LUC} estimate for the year 2024 is informed by extrapolated land-use data (Section 3.2.3, Supplement S.2.1), we estimate the 2025 projection based on fire anomalies in 2025 relative to the year 2023. Peat drainage emissions are assumed to be unaltered, as they have low interannual variability.

S.3 Methodology Ocean CO_2 sink S_{OCEAN}

S.3.1 Observation-based estimates

***f*CO_2-products** - We use nine estimates of the ocean CO_2 sink and its variability based on surface ocean fCO_2 maps obtained by the interpolation of surface ocean fCO_2 measurements. Seven of the methods cover a period from 1990 onwards due to severe restriction in data availability prior to 1990 (Figure 11), whereas two span the period from 1957 and 1959 onwards. These estimates differ in many respects: they use different maps of surface fCO_2, different atmospheric CO_2 concentrations, different wind products and different gas-exchange formulations as specified in Table S3. We refer to them as fCO_2-products. The methods include a data-driven diagnostic method combined with a multi-linear regression approach to extend back to 1957 (Rödenbeck et al., 2022; referred to here as Jena-MLS), five neural network models (Landschützer et al., 2014; referred to as VLIZ-SOMFFN; Chau et al., 2022; Copernicus Marine Environment Monitoring Service, referred to here as CMEMS-LSCE-FFNN; Zeng et al., 2022; referred to as NIES-ML3; Gregor et al., 2019, referred to as CSIR-ML6, Ford et al., 2024; referred to as UExP-FNN-U), one cluster regression approach (Gregor et al., 2024; referred to as OceanSODA-ETHZv2), a multi-linear regression method (Iida et al., 2021; referred to as JMA-MLR), and one method that relates the fCO_2 misfit between GOBMs and SOCAT to environmental predictors using the extreme gradient boosting method extending back to 1959 (Gloege et al., 2022). The ensemble mean of the fCO_2-based flux estimates is calculated from these nine mapping methods. In v2025, we now also include 2 fCO_2 products (JMA-MLR and UExP-FNN-U) where the authors adjusted the SOCAT fCO_2 to account for differences in temperature between the depth of the ship intake and the relevant depth right near the surface

using the dataset provided by Ford et al. (2025). Furthermore, UExP-FNN-U includes an additional adjustment to account for the cool surface skin temperature effect in the air-sea CO_2 flux.

Following the approach of Friedlingstein et al. (2025b), we add 0.18 PgC yr^{-1} (multiplied by 7/9 as 2 products already include the cool skin/warm layer temperature effect). This correction is only done on the fCO_2-products average, at the global scale, for the estimate of S_{OCEAN}.

The impact of the cool skin and warm layer effect on air-sea CO_2 flux is based on established understanding of temperature gradients (as discussed by Goddijn-Murphy et al., 2015 and Woolf et al., 2016), and laboratory observations (Jähne and Haussecker, 1998; Jähne, 2019), however in situ field observational evidence is still sparse (Dong et al., 2022, Ford et al., 2024a). While the cool skin and warm ocean layers are mechanistically well understood, temperature differences between the ship inlet and the sea surface microlayer due to variable sampling depth as well as potential artificial warm biases also have been suggested in the literature (Dong et al., 2022, Watson et al., 2020). These are, however, not considered in the above correction factor due to their uncertainty.

Typically, fCO_2-products do not cover the entire ocean due to missing coastal oceans and sea-ice cover. The CO_2 flux from the fCO_2-based products is already at or above 99% coverage of the ice-free ocean surface area in several products this year (UExP-FNN-U, JMA-MLR, VLIZ-SOMFFN, Jena-MLS, OceanSODA-ETHZv2, either due to complete coverage or a posteriori filling). The products that remained below 99% coverage of the ice-free ocean (CMEMS-LSCE-FFNN, NIES-ML3, LDEO-HPD, CSIR-ML6) were scaled by the following procedure. Since v2022 of the GCB we now scale fluxes globally and regionally (North, Tropics, South) to match the ice-free area (using the HadISST sea surface temperature and sea ice cover; Rayner et al., 2003):

$$FCO_2^{reg-scaled} = \frac{A_{(1-ice)}^{region}}{A_{FCO_2}^{region}} \cdot FCO_2^{region} \quad \text{(S4)}$$

In Eq. (S4), A represents area, (1 – ice) represents the ice-free ocean, A_{FCO2}^{region} represents the coverage of the fCO_2-product for a region, and FCO_2^{region} is the integrated flux for a region.

SOCAT - The measurements underlying the surface fCO_2-products are from the Surface Ocean CO_2 Atlas version 2025 (SOCAT v2025; Bakker et al., 2025), which is an update of version 3 (Bakker et al., 2016) and the subsequent annual updates used in previous versions of the global carbon budget. SOCAT has updated its quality control cookbook for SOCATv2025 (Gkritzalis et al., 2024), partly in response to the results of the 2021 fCO_2 intercomparison experiment (Steinhoff et al., 2025). These changes have been implemented going forwards, i.e. for new and updated data submissions to SOCATv2025. Two important changes in the cookbook are: Membrane-based fCO_2 sensor data can at best receive a flag of E (uncertainty of less than 10 µatm), such that new and updated membrane-based data sets are not part of the synthesis and gridded SOCAT products used for the global carbon budget. Complete metadata is now required for all new and updated data sets (except for historic data sets).

SOCAT v2025 has an additional 2.8 million fCO_2 measurements with an estimated accuracy of better than 5 µatm relative to v2024. Of these, 2 million are from 2024 in a total of 283 data sets (Table S8), while the largest

addition from earlier years is from 2023 with 136 data sets new to SOCAT. Nineteen shipboard data sets that were included in earlier SOCAT versions have been suspended or excluded from SOCATv2025 (Table S13). This includes: two coastal data sets with warming in excess of 10°C, eight data sets in the Arctic Ocean where the sea surface temperature and the equilibrator temperature had been swapped and where some data sets overlapped with other data sets, four data sets in the Atlantic Ocean awaiting updates by the data provider and five data sets in the Southern Ocean with a 2-hour offset between the temperature sensors. All these data sets had passed quality control before inclusion in an earlier SOCAT version. This highlights that some data quality issues are missed during quality control by the data provider and during SOCAT quality control. Inclusion of problematic data sets can affect estimates of ocean CO_2 uptake from data-based mapping products, especially in data sparse regions, such as the polar oceans (Fay et al., 2025). SOCAT will consider introducing additional automated quality control checks relating to excessive warming or cooling of seawater between sampling and analysis, as well as to spikes in these temperature changes.

For 2023, the one but final year in SOCATv2025 (with more data sets than the final year as a result of delays in data submission), there are a total of 269 data sets with measurements in the Northern hemisphere, while there are 107 data sets from the Southern hemisphere. For the Southern Ocean, there are only 33 data sets from 2023 south of 50°S, and only four from Austral winter (June-August). The coverage of SOCAT observations in 2023 is only about 75% of that in 2016 (Fig. 11), mainly as a result of a large reduction in sampling in the Northern hemisphere (from 391 to 269 data sets), while the Southern hemisphere data collection effort showed little change (from 109 to 107 data sets). Each of the data-based estimates uses a different method to map the SOCAT v2025 data to the global ocean.

Prior to 1959 - We further use results from two diagnostic ocean models, Khatiwala et al. (2013) and DeVries (2014), to estimate the anthropogenic carbon accumulated in the ocean prior to 1959. The two approaches assume constant ocean circulation and biological fluxes, with S_{OCEAN} estimated as a response in the change in atmospheric CO_2 concentration calibrated to observations. The uncertainty in cumulative uptake of ±20 GtC (converted to ±1σ) is taken directly from the IPCC's review of the literature (Rhein et al., 2013), or about ±30% for the annual values (Khatiwala et al., 2009).

Additional data - We use the observational constraints assessed by IPCC of a mean ocean CO_2 sink of 2.2 ± 0.7 GtC yr^{-1} for the 1990s (90% confidence interval; Ciais et al., 2013) to verify that the GOBMs and fCO_2-products provide a realistic assessment of S_{OCEAN}. This is based on indirect observations with seven different methodologies and their uncertainties, and further using three of these methods that are deemed most reliable for the assessment of this quantity (Denman et al., 2007; Ciais et al., 2013). The observation-based estimates use the ocean/land CO_2 sink partitioning from observed atmospheric CO_2 and O_2/N_2 concentration trends (Manning and Keeling, 2006; Keeling and Manning, 2014), an oceanic inversion method constrained by ocean biogeochemistry data (Mikaloff Fletcher et al., 2006), and a method based on penetration time scale for chlorofluorocarbons (McNeil et al., 2003). The IPCC estimate of 2.2 GtC yr^{-1} for the 1990s is consistent with a range of methods (Wanninkhof et al., 2013). We refrain from using the IPCC estimates for the 2000s (2.3 ± 0.7 GtC yr^{-1}), and the period 2002-2011 (2.4 ± 0.7 GtC yr^{-1}, Ciais et al., 2013) as these are based on trends derived

mainly from models and one data-product (Ciais et al., 2013). Additional constraints summarised in AR6 (Canadell et al., 2021) are the interior ocean anthropogenic carbon change (Gruber et al., 2019) and ocean sink estimate from atmospheric CO_2 and O_2/N_2 (Tohjima et al., 2019), of which we already use updated data sets for model evaluation and discussion, respectively.

S.3.2 Global Ocean Biogeochemistry Models (GOBMs)

The ocean CO_2 sink for 1959-2024 is estimated using ten GOBMs (Table S2). The GOBMs represent the physical, chemical, and biological processes that influence the surface ocean concentration of CO_2 and thus the air-sea CO_2 flux. The GOBMs are forced by meteorological reanalysis and atmospheric CO_2 concentration data available for the entire time period. They mostly differ in the source of the atmospheric forcing data (meteorological reanalysis), spin up strategies, and in their horizontal and vertical resolutions (Table S2). All GOBMs except one (CESM-ETHZ) do not include the effects of anthropogenic changes in nutrient supply (Duce et al., 2008). They also do not include the perturbation associated with changes in riverine organic carbon (see Section 2.10 and Supplement S.6.3). Four sets of simulations were performed with each of the GOBMs. Simulation A applied historical changes in climate and atmospheric CO_2 concentration. Simulation B is a control simulation with constant atmospheric forcing (normal year or repeated year forcing) and constant pre-industrial atmospheric CO_2 concentration. Simulation C is forced with historical changes in atmospheric CO_2 concentration, but repeated year or normal year atmospheric climate forcing. Simulation D is forced by historical changes in climate and constant pre-industrial atmospheric CO_2 concentration.

To derive S_{OCEAN} from the model simulations, we subtracted the slope of a linear fit to the annual time series of the control simulation B from the annual time series of simulation A. Assuming that drift and bias are the same in simulations A and B, we thereby correct for any model drift. Further, this difference also removes the natural steady state flux (assumed to be 0 GtC yr^{-1} globally without rivers), which is often a major source of biases. Note, however, that Gürses et al. (2023) questioned the assumption of comparable bias and drift in simulations A and B as they compared two versions of FESOM-REcoM, and found a very similar air-sea CO_2 flux in simulation A despite a different bias as derived from simulation B. This approach works for all model set-ups, including IPSL and Princeton, where simulation B was forced with variable historical climate changes (looping over a certain repeated period for atmospheric forcing). This approach assures that the interannual variability is not removed from IPSL and Princeton simulation A.The absolute correction for bias and drift per model in the 1990s varied between <0.01 GtC yr^{-1} and 0.41 GtC yr^{-1}, with one model having a positive bias, six having negative biases and three model having essentially no biases (NorESM, ACCESS, CESM-ETHZ, $\leq$ 0.02 GtC yr^{-1}). The MPI, IPSL and Princeton models use riverine input and therefore simulate outgassing in simulation B. By subtracting a linear fit of simulation B, also the ocean carbon sink of these models follows the definition of S_{OCEAN}. This correction increases the model mean ocean carbon sink by 0.12 GtC yr^{-1} in the 1990s.
The ocean models cover 99% to 101% of the total ocean area, so that area-scaling is not necessary.
Finally, as proposed in Friedlingstein et al. (2025b) we upscale the multi model average estimate of the ocean sink by 10% to account for the known underestimation of the sink by the GOBMs (section 2.5 and Friedlingstein et al., 2025b). This is justified by the GOBM average underestimating anthropogenic carbon accumulation by 10% in the period 1994 to 2007 (section 3.6.5), in the 1990s and 2000s (Table 6) and by 15%

in the 2010s (Table 6). Also the fact that most models simulate a low AMOC and a high Revelle factor (compared to GLODAP, Table S11) supports a higher ocean carbon sink although the emergent constraint framework (Terhaar et al., 2022) does not yield significant results for the GOBMs (Terhaar et al., 2024). This correction is only done on the GOBMs average, at the global scale, for the estimate of S_{OCEAN}.

S.3.3 GOBM evaluation

The ocean CO_2 sink for all GOBMs and the ensemble mean falls within 90% confidence of the observed range, or 1.5 to 2.9 GtC yr^{-1} for the 1990s (Ciais et al., 2013) before and after applying adjustments.

In addition to the interior ocean anthropogenic carbon accumulation (Section 3.6.5), we evaluate the models with process-based metrics that were previously related to ocean carbon uptake (Table S12). These are the Atlantic Meridional Overturning Circulation (Goris et al., 2018, Terhaar et al., 2022, 2024), the Southern Ocean sea surface salinity (Terhaar et al., 2021, 2022, 2024, Hauck et al., 2023b), the Southern Ocean stratification index (Bourgeois et al., 2022) and the surface ocean Revelle factor (Terhaar et al., 2022, 2024).

We follow the methodology of previous studies wherever possible, particularly the RECCAP2 model evaluation chapter (Terhaar et al., 2024). The Atlantic Meridional Overturning Circulation from the GOBMs is here defined as the maximum of the Atlantic meridional overturning streamfunction at 26°N. This is compared to data from the RAPID array at 26°N (Moat et al., 2025). An uncertainty of 0.9 Sv was reported in McCarthy et al. (2015). We use the years 2005-2023, which are all complete calendar years available from the RAPID data set, and report the temporal standard deviation over that period.

The Southern Ocean sea surface salinity is reported for the subpolar seasonally stratified biome (SPSS) and for the area covering both the SPSS and subtropical seasonally stratified (STSS) biomes. Biome definitions are taken from Fay and McKinley (2014, as provided for the RECCAP2 project). The sea surface salinity was first used as an emergent constraint for the Southern Ocean CO_2 uptake with Earth System Models (Terhaar et al. 2021, 2022) using the interfrontal salinity between the polar and subtropical fronts with dynamic fronts. As the GOBMs are forced with reanalysis data, the fronts do not vary as much as in the ESMs, and thus the use of fixed biomes is justified (Hauck et al., 2023b, Terhaar et al., 2024). We use the time period 2005-2024. The observational sea surface salinity values are calculated from the EN4 data set (Good et al., 2013; using the objective analyses – Gouretski and Reseghetti (2010) XBT corrections and Gouretski and Cheng (2020) MBT corrections) with the aid of the Fay and McKinley (2014) mask.

The Southern Ocean stratification index is a simplified version of the metric used in Bourgeois et al. (2022). It is defined as the difference between in situ density at the surface and at 1000 m depth in the latitudinal band of 30°S to 55°S. Each model provider calculated this metric based on their native model mesh. We use the period of 2005-2024. The same metric was calculated from the EN4 data set mentioned above (Good et al., 2013).

Finally, the global surface ocean Revelle factor is reported. Monthly 1°x1° gridded fields were provided by the modelling groups, based on standard carbonate chemistry routines (e.g., mocsy, Orr & Epitalon, 2015;

PyCO2SYS, Humphreys et al., 2022a,b). The observational metrics come from two sources, firstly the gridded GLODAP data set v2.2016 (Lauvset et al., 2016), which is a climatology centered around the year 2002. For comparison with GLODAP, the models were subsampled to GLODAP data coverage and to a comparable time window also centred around 2002 (1997-2007). Secondly, the OceanSODA_v2023 data set (Gregor and Gruber, 2020, updated) was used, which has all input data available to calculate the surface ocean Revelle factor. OceanSODA covers a slightly smaller surface area (~96 % of GLODAP) but provides data until 2022. The period 2005-2022 was used due to data availability and the models were subsampled to the same spatial and temporal coverage.

We now also summarize GOBM performance relative to each other using the IOMB framework (Ogunro et al., 2018, Fu et al., 2022). The International Ocean Model Benchmarking (IOMB) system is a Python–Xarray-based open-source software framework designed to evaluate the performance of global ocean biogeochemical models. Building upon the benchmarking principles established by Collier et al. (2018) and Fu et al. (2022), IOMB provides a systematic approach to assess model skill against a range of observational datasets. IOMB quantifies model performance using statistical metrics, including bias, root mean square error (RMSE), annual cycle phase, and spatial distribution. Each of these contributes to an overall performance score (refer to equation 7 in Fu et al., 2022), which enables objective comparison across models. The IOMB framework has been further expanded and refined to address uncertainties in the estimation of the ocean carbon sink (IOMB-GCBv1). In this updated version, several new diagnostics were introduced, including the Revelle factor, Southern Ocean SPSS biome surface salinity, Southern Ocean stratification index, Atlantic Meridional Overturning Circulation (AMOC), and CO_2 fugacity. These metrics enhance the system's ability to evaluate model skill in reproducing critical physical and biogeochemical processes that influence the global ocean carbon sink. This version of IOMB also incorporates time-series analysis capabilities, where the overall model score is computed as a combination of the bias score and the Taylor score (depends on the normalized standard deviation and correlation). The final benchmark visualization presents Z-score normalized results, enabling fair comparison of model performance relative to each other across multiple variables and metrics. Figure S6 illustrates the evaluation results from IOMB-GCBv1, where key variables of interest are assessed against state-of-the-art observational datasets. The model climatology for the period 2000–2024 is compared with corresponding observational climatologies to evaluate model performance in simulating upper-ocean physics and biogeochemistry.

To assess upper-ocean physical processes, the variables sea surface temperature (SST), sea surface salinity (SSS), mixed layer depth (MLD), Southern Ocean stratification index, Southern Ocean SPSS biome salinity, and Atlantic Meridional Overturning Circulation (AMOC) were analyzed. For temperature and salinity, individual performance scores are computed relative to WOA2023 (Locarnini et al., 2023, Reagan et al., 2023) and GLODAPv2-2023 (Lauvset et al., 2024) observations, and an overall score is derived by combining both. The mixed layer depth, a key indicator of upper and interior ocean exchange, is evaluated using multiple observational products, including Sallée et al. (2021), de Boyer Montégut (2023), and de Boyer Montégut et al. (2004). The RAPID 26°N AMOC observational record (2005– 2023) is used to assess the modeled AMOC strength (Moat et al., 2025). The EN4.2.2 dataset (2005–2024, Good et al., 2013) provides the basis for evaluating both the Southern Ocean stratification index and SPSS biome salinity.

To evaluate carbonate chemistry, model-simulated surface total alkalinity and dissolved inorganic carbon (DIC) are compared against GLODAPv2-2023 observations. For the Revelle factor, we use GLODAPv2-2023 (derived using PyCO2SYS v1.8 package, Humphreys et al., 2022) and the OceanSODA_ETHZ observation-based data set (Gregor and Gruber, 2020 updated). Finally, CO_2 fugacity from the models is compared against SOCATv2025 (Bakker et al., 2025) to complete the evaluation.

S3.4 fCO_2-product evaluation

To benchmark the performance of 9 fCO_2-products included this year, we compare the suite of 9 fCO_2 products to independent observations that have not been included in any training/regression step of the methods, i.e. direct fCO_2 measurements from the Surface Ocean CO_2 Atlas (Bakker et al., 2016) that received a quality flag E (uncertainty less than 10 µatm) and calculated fCO_2 from surface ocean measurements of dissolved inorganic carbon and total alkalinity with quality flag of at least 2 from the Global Ocean Data Analysis Project (GLODAP, Lauvset et al. 2024) of the top 10 meters, via the CO2sys carbonate system calculation software (Sharp et al., 2020), using the dissociation constants of Lueker et al. (2000). Additionally, we use temperature-corrected SOCAT flag E fCO_2 measurements (from Ford et al., 2025) for comparisons with JMA-MLR and UExP-FNN-U for consistency. Both sets of measurements carry inherent larger uncertainty than the SOCAT measurements the fCO_2-products are based on, however, their independent nature and spatial extent allows us to further investigate regional biases in fCO_2-products.

Interestingly, Figure S7 reveals overall close to zero or negative biases in all products, with the exception of the GLODAP comparison in the region north of 30°N, highlighting a tendency of the fCO_2-products to underestimate the sea surface fugacity of the observations. We find the smallest errors in the Southern Hemisphere south of 30°S in all fCO_2-products, i.e. a region that has substantially less seasonal data coverage compared to the northern hemisphere and where we find the largest trend divergence between GOBMs and fCO_2-products (see main text and below). Overall, fCO_2 products perform better against calculated GLODAP measurements compared to SOCAT flag E data, but with biases within the expected measurement uncertainty (up to 10 µatm). There are only 4 exceptions where biases are beyond the expected uncertainty range of the measurements, i.e. in the Northern Hemisphere, where UExP-FNN-U (-40.47 µatm), Jena-MLS (22.20 µatm) and OceanSODA-ETHv2 (13.49 µatm) show larger biases and in the tropics where OceanSODA-ETHZv2 (10.29 µatm) falls just outside the 10 µatm range. Larger spreads, represented by the RMSE exist in the north compared to SOCAT flag E data in the same products that illustrated the largest bias (with RMSE exceeding 100 µatm), however, the impact on the resulting global bias and RMSE remains small due to the very limited number of measurements in this region, explaining the larger bias and local spread. The global comparison reveals a better agreement with GLODAP measurements (mean bias of -2.03 µatm) compared to SOCAT flag E data (mean of -6.25 µatm), however, for all products within the estimated measurement uncertainty.

This year, we also update the trend benchmark analysis using a set of 5 GOBM´s, namely CESM-ETHZ, FESOM2.1-REcoM, MRI-ESM2, IPSL and NorESM, that were submitted to the GCB2023 (Friedlingstein et al., 2023) following the approach of Hauck et al. (2023a). A total of 7 fCO_2-products conducted the benchmark

test (VLIZ-SOMFFN, NIES-ML3, Jena-MLS, CSIR-ML6, OceanSODA-ETHZv2, JMA-MLR and UExP-FNN-U). The GOBMs serve as known truth and are subsampled according to the real-world observation tracks. The fCO_2-products then reconstruct the true model field, based on the subsampled information provided. We then compare trends for the period 2001-2021, i.e. the period where we see the divergence between fCO_2-products and models, removing the final year to avoid the tail effect. The trends of the individual fCO_2-products from the GCB2025 were then plotted against the mean of the trend reconstruction bias (evaluated against the known truth GOBM trends) of the 5 GOBMs. This is shown in Figure S8. The figure illustrates the tendency that fCO_2-products with negative biases in the fCO_2 reconstruction show the strongest air-sea CO_2 flux trends and vice versa for the fCO_2 products with positive biases. Globally, the ensemble of 7 fCO_2 methods suggest a mean trend of 0.58±0.20 PgC yr^{-1} $decade^{-1}$ (mean and standard deviation across the y-axis of Figure S8). Figure S8 also suggests a tendency of the products to underestimate the global fCO_2 trend by -0.29±0.65 ppm $decade^{-1}$ compared to the model truth (mean and standard deviation across the x-axis in Figure S8). Due to compensating negative and positive fCO_2 biases, the ensemble mean trend bias is smaller than suggested from previous studies focusing on one or two fCO_2-products only (see e.g. Gloege et al. 2021, Hauck et al. 2023a). The inferred global flux trend of 0.50±0.13 PgC yr^{-1} $decade^{-1}$ that intercepts with the zero bias line is smaller than the mean trend suggested by the 7 fCO_2-products, but larger than in previous versions due to the addition of one extra method and a fifth model, however, it still is within the combined uncertainty estimate of a recent estimate by Mayot et al. (2024) of 0.42±0.06 PgC yr^{-1} $decade^{-1}$ (period 2000-2022) in the mean, although with a substantially larger uncertainty and different time period. The evidence basis, thus, remains low due to the small sample size of fCO_2-products (n = 7) and reconstructed GOBMs (n = 5).

S3.5 Uncertainty assessment for S_{OCEAN}

We quantify the 1-σ uncertainty around the mean ocean sink of anthropogenic CO_2 by assessing random and systematic uncertainties for the GOBMs and fCO_2-products. The random uncertainties are taken from the ensemble standard deviation (0.3 GtC yr^{-1} for GOBMs, 0.3 GtC yr^{-1} for fCO_2-products). We derive the GOBMs systematic uncertainty by the mean deviation from the observation-based anthropogenic carbon inventory changes (Gruber et al. (2019); Müller et al., 2023; DeVries, 2022) reported in Section 3.6.5 (0.3 GtC yr^{-1}) and suggest these are related to physical transport (mixing, advection) into the ocean interior. For the fCO_2-products, we consider systematic uncertainties stemming from uncertainty in fCO_2 observations (0.2 GtC yr^{-1} , Takahashi et al., 2009; Wanninkhof et al., 2013), gas-transfer velocity (0.2 GtC yr^{-1} , Ho et al., 2011; Wanninkhof et al., 2013; Roobaert et al., 2018), wind product (0.1 GtC yr^{-1}, Fay et al., 2021), river flux adjustment (0.3 GtC yr^{-1}, Regnier et al., 2022, formally 2-σ uncertainty), and fCO_2 mapping (0.2 GtC yr^{-1}, Landschützer et al., 2014). Combining these uncertainties as their squared sums, we assign an uncertainty of ± 0.4 GtC yr^{-1} to the GOBMs ensemble mean and an uncertainty of ± 0.6 GtC yr^{-1} to the fCO_2-product ensemble mean, which is smaller than a recent estimate by Ford et al. (2024), who estimate an uncertainty of ±0.7 GtC yr^{-1} based on propagating different sources of uncertainty in fCO_2-products. Here, the uncertainties are propagated as $\sigma(S_{OCEAN}) = 0.5 * (0.4^2+0.6^2)^{1/2}$ GtC yr^{-1} and result in an ± 0.4 GtC yr^{-1} uncertainty around the best estimate of S_{OCEAN}.

We examine the consistency between the variability of the GOBMs and the fCO_2-products to assess confidence in S_{OCEAN}. Individual estimates (both GOBMs and fCO_2products) generally produce a higher ocean CO_2 sink

during strong El Niño events. There is emerging agreement between GOBMs and fCO_2-products on the patterns of decadal variability of S_{OCEAN} with a global stagnation in the 1990s and an extra-tropical strengthening in the 2000s (McKinley et al., 2020, Hauck et al., 2020). More recently, a fast growth of the sink is simulated by both methods between 2001 and 2016, and a stagnation period since then. A stagnation or even decline of S_{OCEAN} occurred during the triple La Niña years 2020-2023. The central estimates of the annual flux from the GOBMs and the fCO_2-products have a correlation r of 0.98 (1990-2024). The agreement between the models and the fCO_2-products reflects some consistency in their representation of underlying variability since there is little overlap in their methodology or use of observations.

S3.6 Observation-based estimates of carbon storage changes in the ocean interior

We rely on three observation-based methods to quantify temporal changes in dissolved inorganic carbon (DIC) in the ocean interior, differing in their underlying observations, gap-filling approach, temporal resolution and the type of carbon fluxes they resolve.

The extended multiple linear regression (eMLR) method (Müller et al., 2023; Gruber et al., 2019) applied to the tracer C* builds on observations of DIC, total alkalinity, phosphate, oxygen and other physical and biogeochemical variables from GLODAPv2 (Lauvset et al., 2022) collected during repeat surveys. The method calculates a quasi-conservative tracer C*, separating biological from anthropogenic carbon variability, and fits regional multiple regressions of C* against temperature, salinity, oxygen, and nutrients for individual water masses separated along neutral density surfaces. Finally, these regional MLR regressions are applied to global climatological fields to map the decadal change in anthropogenic carbon as the differences between survey periods. The data sets provide a 13-year estimates for the period 1994-2007 (Gruber et al., 2019) and decadal estimates for the period 1994-2004 and 2004-2014 (Müller et al., 2023).

The Ocean Circulation Inverse Model (OCIM; DeVries, 2022) uses an observation-constrained steady-state ocean circulation model that assimilates temperature, salinity, CFCs, and radiocarbon to reconstruct the large-scale transport field. An abiotic carbon cycle module is then forced with the evolving atmospheric pCO_2 (partial pressure of CO_2) to simulate air–sea CO_2 fluxes and interior carbon storage. Because biological and internal biogeochemical feedbacks are excluded, OCIM isolates the anthropogenic component of the ocean carbon sink. OCIM covers the period 1990 to 2020.

The Mapped Observation-Based Oceanic DIC (MOBO-DIC; Keppler et al., 2023) approach employs a two-step approach of self-organizing maps and feed-forward neural networks trained on ship-based DIC measurements from GLODAPv2 and corresponding environmental predictors such as temperature, salinity, nutrients, oxygen for the upper ocean and atmospheric pCO_2. The trained models reconstruct monthly global ocean interior DIC fields at 1° resolution for 2004–2019. As MOBO-DIC is based on total DIC observations without separating the anthropogenic component, it resolves the combined anthropogenic plus natural DIC changes.

To scale eMLR(C*)-based estimates to full decades (1990s, 2000s) reported in Table 6, the cumulative ocean carbon storage change over the original base periods (1994-2004-2014) was divided by the corresponding atmospheric CO_2 increase (NOAA/GML global mean CO_2) to obtain a sink efficiency (Pg C ppm^{-1}), following Müller et al. (2023). These efficiencies were then multiplied by the observed atmospheric CO_2 change over the closest target decade, assuming proportionality between atmospheric CO_2 growth and oceanic CO_2 uptake. OCIM and eMLR(C*) estimates were further adjusted for non-steady changes in natural DIC storage, obtained from the ensemble of GOBMs (Sim D - Sim B), to obtain estimates formally consistent with the definition of S_{OCEAN}. In Table 6, the mean and range are provided for all members of the ensemble of three ocean interior estimates (OCIM, eMLR(C*), MOBO-DIC) that cover the full reported decade.

S.4 Methodology Land CO_2 sink S_{LAND}

S.4.1 DGVM simulations

The DGVMs model runs were forced by either the merged monthly Climate Research Unit (CRU) and 6 hourly Japanese 3-quarter century Reanalysis (JRA-3Q) data set or by the monthly CRU data set, both providing observation-based temperature, precipitation, and incoming surface radiation on a 0.5°x0.5° grid and updated to 2024 (Harris et al., 2014, 2020). The combination of CRU monthly data with 6 hourly forcing from JRA-3Q (Kobayashi et al., 2015) is performed with methodology used in previous years (Viovy, 2016) adapted to the specifics of the JRA-3Q data.

Introduced in GCB2021 (Friedlingstein et al., 2022a), incoming short-wave radiation fields take into account aerosol impacts and the division of total radiation into direct and diffuse components as summarised below. The diffuse fraction dataset offers 6-hourly distributions of the diffuse fraction of surface shortwave fluxes over the period 1901-2024. Radiative transfer calculations are based on monthly-averaged distributions of tropospheric and stratospheric aerosol optical depth, and 6-hourly distributions of cloud fraction. Methods follow those described in the Methods section of Mercado et al. (2009), but with updated input datasets.

The time series of speciated tropospheric aerosol optical depth is taken from the historical and RCP8.5 simulations by the HadGEM2-ES climate model (Bellouin et al., 2011). To correct for biases in HadGEM2-ES, tropospheric aerosol optical depths are scaled over the whole period to match the global and monthly averages obtained over the period 2003-2020 by the CAMS Reanalysis of atmospheric composition (Inness et al., 2019), which assimilates satellite retrievals of aerosol optical depth.

The time series of stratospheric aerosol optical depth is taken from the by Sato et al. (1993) climatology, which has been updated to 2012. Years 2013-2020 are assumed to be background years so replicate the background year 2010. That assumption is supported by the Global Space-based Stratospheric Aerosol Climatology time series (1979-2016; Thomason et al., 2018). The time series of cloud fraction is obtained by scaling the 6-hourly distributions simulated in the Japanese Reanalysis (Kobayashi et al., 2015) to match the monthly-averaged cloud cover in the CRU TS v4.06 dataset (Harris et al., 2020). Surface radiative fluxes account for aerosol-radiation interactions from both tropospheric and stratospheric aerosols, and for aerosol-cloud interactions from tropospheric aerosols, except mineral dust. Tropospheric aerosols are also assumed to exert interactions with clouds. The radiative effects of those aerosol-cloud interactions are assumed to scale with the radiative effects of aerosol-radiation interactions of tropospheric aerosols, using regional scaling factors derived from HadGEM2-

ES. Diffuse fraction is assumed to be 1 in cloudy sky. Atmospheric constituents other than aerosols and clouds are set to a constant standard mid-latitude summer atmosphere, but their variations do not affect the diffuse fraction of surface shortwave fluxes.

In addition to the climate forcing, the DGVMs forcing also include the global atmospheric CO_2 time series, same as for the GOBMs and described in Section S.3.2 (Lan et al. (2023), the gridded land cover changes (see Supplement S.2.2), and the gridded nitrogen deposition and fertilisers (see Table S1 for specific models details). Four simulations were performed with each of the DGVMs.

Four simulations are performed with the DGVMs.

- Simulation 0 (S0) is a control simulation which uses fixed pre-industrial (year 1700) atmospheric CO2 concentrations, cycles early 20th century (1901-1920) climate and applies a time-invariant pre-industrial land cover distribution and pre-industrial wood harvest rates.
- Simulation 1 (S1) differs from S0 by applying historical changes in atmospheric CO2 concentration and N inputs.
- Simulation 2 (S2) applies historical changes in atmospheric CO_2 concentration, N inputs, and climate, while applying time-invariant pre-industrial land cover distribution and pre-industrial wood harvest rates.
- Simulation 3 (S3) applies historical changes in atmospheric CO_2 concentration, N inputs, climate, and land cover distribution and wood harvest rates.

S2 is used to estimate the land sink component of the global carbon budget (S_{LAND}). S3 is used to estimate the total land flux but is not used in the global carbon budget. We further separate S_{LAND} into contributions from CO_2 (=S1-S0) and climate (=S2-S1+S0).

S.4.2 RSS correction

New for GCB2025 we correct S_{LAND} for a known bias due to the simulation protocol for the S2 simulation, whereby land cover is fixed at 1700 values. This leads to too high forest cover at global scale in the present day. Historical land-use change was dominated by transitions from vegetation types that can provide a large carbon sink per area unit (typically, forests) to others less efficient in removing CO_2 from the atmosphere (typically, croplands). This overestimate in the S_{LAND} is referred to as Replaced Sinks and Sources (RSS) and represents the difference between natural sinks under pre-industrial vs. historical land cover (Dorgeist et al., 2024, O'Sullivan et al., 2025; Friedlingstein et al. 2025b). To estimate this correction of S_{LAND}, we use output from 7 DGVMs (CABLE-POP, CLASSIC, GDSTEM, IBIS, iMAPLE, JSBACH, and LPX-Bern), which were able to output net biome productivity (NBP) on a Plant Functional Type basis (PFT). Although all DGVMs simulate carbon fluxes for vegetation on a PFT basis, this is not necessarily the case for heterotrophic respiration from soils. Many models consider soil carbon pools as well-mixed and do not associate with individual PFTs. S_{LAND} from the S2 simulation is corrected by weighting the PFT-level NBP of each grid cell by the fractional cover of each PFT in the S3 simulation in each year, producing a gridcell-mean NBP that reflects the response of the land biosphere to changes in climate and atmospheric composition, while accounting for realistic land cover. The RSS bias is calculated as the difference between the original S2 S_{LAND} estimate and the corrected S_{LAND} for each of the 7 DGVMs. Following O'Sullivan et al. (2025), using a mixed-effects regression an S_{LAND}-RSS relationship is derived from this DGVM subset. This amounts to a 19% reduction of S_{LAND} applied to the remaining 15

DGVMs to estimate the corrected S_{LAND} (i.e. original S_{LAND} - predicted RSS) at the global scale. For the regional and spatial estimates of S_{LAND} in this paper, we use the mean RSS for the 7 model subset to adjust the full ensemble of DGVMs. See O'Sullivan et al. (2025) for a full description.

S.4.3 DGVM evaluation

We apply three criteria for minimum DGVMs realism by including only those DGVMs with (1) steady state after spin up, (2) global net land flux ($S_{LAND} - E_{LUC}$) that is an atmosphere-to-land carbon flux over the 1990s ranging between -0.3 and 2.3 GtC yr^{-1}, within 90% confidence of constraints by global atmospheric and oceanic observations (Keeling and Manning, 2014; Wanninkhof et al., 2013), and (3) global E_{LUC} that is a carbon source to the atmosphere over the 1990s, as already mentioned in Supplement S.2.2. All DGVMs meet these three criteria.

The International LAnd Model Benchmarking (ILAMB) system (Collier et al. 2018; version 2.7.2 (2024): https://github.com/rubisco-sfa/ILAMB/releases/tag/v2.7.2) is used to compare the 23 models (22 DGVMs and CARDAMOM) to observational benchmarks for a number of different variables related to the land surface: live biomass carbon, gross primary productivity (GPP), leaf area index (LAI), ecosystem respiration (heterotrophic + autotrophic), soil carbon, evapotranspiration, runoff, burned areas, fire CO_2 emissions, and soil respiration. Each row for each variable in Figure S11 is clickable in the full website version (https://gws-access.jasmin.ac.uk/public/landsurf_rdg/pmcguire/ILAMB_output_TRENDYv14/TRENDYv14_latest/) and gives access to geographic plots for such quantities as bias relative to observational benchmark, temporal RMSE from the observational benchmark, and difference in max month from the observational benchmark. The full website version also gives a spatial Taylor diagram for all the models, as well as time series comparisons of the regional mean time-series and the regional mean annual cycle.

This year, we include Biomass Carbon in the ILAMB analysis, wherein we add a time-dependent annual dataset, ESACCI6.0 (Santoro et al. 2024), for the years 2015-2022, and a time-dependent annual dataset XuSaatchi (Xu et al., 2021), for the years 2000-2019. For the ESACCI dataset, the ESACCI6.0 dataset, and the XuSaatchi dataset, we use an approximate, global, linearized, allometric root-to-shoot ratio (RSR) of 0.275 to convert above-ground biomass to total above-ground + below-ground biomass (multiplying by 1.0 + RSR).

In the ILAMB setup for TRENDYv13 (GCB2024), we added three extra variables (annual-averaged Burned Area, Fire Emissions, and Soil Respiration). In addition for TRENDY-GCB2025 the following changes are made:

1) Modified the Koven et al., (2017) analysis slightly for the Soil Carbon variable, when masking out arid regions;
2) Added annually-averaged observational data sets for GFED5 for both Burned Area and Fire Emissions (Chen et al. 2023);
3) Enabled a pre-existing ILAMB variable for Carbon Dioxide, which uses Net Biome Production (NBP) over land as an emulator for Carbon Dioxide that is subsequently transported by atmospheric circulation to the observation sites, as in Liptak et al. (2017).

The new variables in GCB2024/25 are assigned into the category, 'Ecosystem and Carbon Cycle Extended'. Variables in this category do not affect the overall scores for the category 'Ecosystem and Carbon Cycle'. For TRENDY-GCB2025, Burned Area from two models (EDv3 and SDGVM) are corrected in post-processing to mask out fuel limited regions (i.e. grid cells with no vegetation or with no carbon emissions due to fire).

A row for the total score is added to the ILAMB summary page, and this total score is called 'Hydrology and Carbon Cycles'. The total score is the weighted average of the 'Hydrology Cycle' (weight of 2, since there are 2 variables under Hydrology Cycle) and the 'Ecosystem and Carbon Cycle' (weight of 5 , since there are 5 variables under the Ecosystem and Carbon Cycle).

The TRENDY-GCB2025 version of the updated ILAMB version 2.7.2 GitHub code fork/branch is available at: https://github.com/mcguirepatr/ILAMB/tree/master

S.4.4 Uncertainty assessment for S_{LAND}

For the uncertainty for S_{LAND}, we use the standard deviation of the annual CO_2 sink across the DGVMs, averaging to about ± 0.6 GtC yr^{-1} for the period 1959 to 2024. We attach a medium confidence level to the annual land CO_2 sink and its uncertainty because the estimates from the residual budget and averaged DGVMs match well within their respective uncertainties (Table 5).

S.5 Methodology Atmospheric Inversions

S.5.1 Inversion System Simulations

Fourteen atmospheric inversions (details of each in Table S4) were used to infer the spatio-temporal distribution of the CO_2 flux exchanged between the atmosphere and the land or oceans. These inversions are based on Bayesian inversion principles with prior information on fluxes and their uncertainties. They use very similar sets of surface measurements of CO_2 time series (or subsets thereof) from various flask and in situ networks. Six inversion systems used surface observations, and eight inversion systems used satellite XCO_2 retrievals from GOSAT and/or OCO-2, of which three systems used a combination of satellite and surface observations. Each inversion system uses different methodologies and input data but is rooted in Bayesian inversion principles. These differences mainly concern the selection of atmospheric CO_2 data and prior fluxes, as well as the spatial resolution, assumed correlation structures, and mathematical approach of the models. Each system uses a different transport model, which was demonstrated to be a driving factor behind differences in atmospheric inversion-based flux estimates, and specifically their distribution across latitudinal bands (Gaubert et al., 2019; Schuh et al., 2019).

Most of the fourteen inversion systems prescribe similar global fossil fuel emissions for E_{FOS}; specifically, the GCP's Gridded Fossil Emissions Dataset version 2025.1 (GCP-GridFEDv2025.1; Jones et al., 2025), which is an update through 2024 of the first version of GCP-GridFED presented by Jones et al. (2021b) (Table S4). All GCP-GridFED versions scale gridded estimates of CO_2 emissions from EDGARv4.3.2 (Janssens-Maenhout et al., 2019) within national territories to match national emissions estimates provided by the GCP for the years 1959-2024, which are compiled following the methodology described in Supplement S.1. GCP-GridFEDv2025.1 adopts the seasonality of emissions (the monthly distribution of annual emissions) from the

Carbon Monitor (Liu et al., 2020a,b; Dou et al., 2022) for Brazil, China, all EU27 countries, the United Kingdom, the USA and shipping and aviation bunker emissions. The seasonality present in Carbon Monitor is used directly for years 2019-2024, while for years 1959-2018 the average seasonality of 2019, and 2021 and 2022 are applied (avoiding the year 2020 during which emissions were most impacted by the COVID-19 pandemic). For all other countries, seasonality of emissions is taken from EDGAR (Janssens-Maenhout et al., 2019; Jones et al., 2023), with small annual correction to the seasonality present in 2010 based on heating or cooling degree days to account for the effects of inter-annual climate variability on the seasonality of emissions (Jones et al., 2021b).

Small remaining differences between regridding of the GridFED inputs, or the use of different fossil fuel emission priors are corrected for by scaling the resulting inverse fluxes to GridFEDv2025.1. The consistent use of E_{FOS} ensures a close alignment with the estimate of E_{FOS} used in this budget assessment, enhancing the comparability of the inversion-based estimate with the flux estimates deriving from DGVMs, GOBMs and *f*CO_2-based methods. The fossil fuel adjustment (including emissions from cement production and cement carbonation CO_2 sink) ensures that the estimated uptake of atmospheric CO_2 by the land and oceans was fully consistent within the inversion ensemble.

The land and ocean CO_2 fluxes from atmospheric inversions contain anthropogenic perturbation and natural pre-industrial CO_2 fluxes. On annual time scales, natural pre-industrial fluxes are primarily land CO_2 sinks and ocean CO_2 sources corresponding to carbon taken up on land, transported by rivers from land to ocean, and outgassed by the ocean. These pre-industrial land CO_2 sinks are thus compensated over the globe by ocean CO_2 sources corresponding to the outgassing of riverine carbon inputs to the ocean, using the exact same numbers and distribution as described for the ocean in Section 2.5. To facilitate the comparison, we adjusted the inverse estimates of the land and ocean fluxes per latitude band with these numbers to produce historical perturbation CO_2 fluxes from inversions.

S.5.2 Inversion System Evaluation

All participating atmospheric inversions are checked for consistency with the annual global growth rate, as both are derived from the global surface network of atmospheric CO_2 observations. In this exercise, we use the conversion factor of 2.086 GtC ppm^{-1} to convert the inverted carbon fluxes to mole fractions, as suggested by Prather (2012). This number is specifically suited for the comparison to surface observations that do not respond uniformly, nor immediately, to each year's summed sources and sinks. This factor is therefore slightly smaller than the GCB conversion factor in Table 1 (2.142 GtC ppm^{-1}, Ballantyne et al., 2012). Overall, the inversions agree with the growth rate with biases between 0.003-0.04 ppm yr^{-1} (0.006-0.08 GtC yr^{-1}) for the period 2015-2024.

The atmospheric inversions are also evaluated using vertical profiles of atmospheric CO_2 concentrations (Figure S13). More than 50 aircraft programs over the globe, either regular programs or repeated surveys over at least 9 months (except on the SH), have been used to draw a robust picture of the system performance (with space-time data coverage irregular and denser in the 0-45°N latitude band; Table S9 and lower panel in Figure S13). The fourteen systems are compared to these independent aircraft CO_2 observations between 2 and 7 km above sea level between 2001 and 2024. Results are shown in Figure S13, where the inversions generally match the atmospheric mole fractions to within 0.6 ppm at all latitudes.

S.6 Methodology Earth System Models (ESMs)

The decadal prediction systems based on ESMs used here consist of three sets of simulations: (i) uninitialized freely evolving historical simulations (1850-2014); (ii) assimilation reconstruction incorporating observational data into the ESMsmodel (1960-2024); (iii) initialised prediction simulations for the 1981-2025 period, starting every year from initial states obtained from the above assimilation simulations. The assimilations are designed to reconstruct the actual evolution of the Earth system by assimilating essential fields from data products. The assimilations' states, which are expected to be close to observations, are used to start the initialised prediction simulations used for the current year (2025) global carbon budget. Similar initialised prediction simulations starting every year (Nov. 1st or Jan. 1st) over the 1981-2024 period (i.e., hindcasts) are also performed for predictive skill quantification and for bias correction. More details on the illustration of a decadal prediction system based on an ESM can refer to Figure 1 of Li et al. (2023).

Six ESMs, i.e., CanESM5 (Swart et al., 2019; Sospedra-Alfonso et al., 2021), EC-Earth3-CC (Döscher et al. 2021; Bilbao et al., 2021; Bernardello et al., 2024), IPSL-CM6A-CO2-LR (Boucher et al., 2020), MIROC-ES2L (Watanabe et al., 2020), MPI-ESM1-2-LR (Mauritsen et al., 2019; Li et al., 2023), and NorCPM-CC (Tjiputra et al. 2020; Bethke et al. 2021) have performed 10-ensemble members of prediction simulations. Each ESM uses a different assimilation method and combination of data products incorporated into the model. More details on the models' configuration can be found in Table 4 and Supplement Table S5. The ESMs use external forcings from the Coupled Model Intercomparison Project Phase 6 (CMIP6) historical (1960-2014) plus SSP2-4.5 baseline and CovidMIP two-year blip scenario (2015-2025) (Eyring et al., 2016; Lamboll et al., 2021). The CO_2 emissions forcing from 2015-2024 are substituted by GCB-GridFED (v2025.0, Jones et al., 2025) to provide a consistent CO_2 forcing, the CO_2 emissions forcing for year 2025 is an extension with the same emission of the year 2024.

S.7 Atmospheric CO_2 time series

The 1750-2024 atmospheric CO_2 concentration times series is produced as follows.
Since January 1980, we use the CO_2 global growth rate reported by NOAA/GML (Lan et al., 2024). In the period March 1958-December 1979, we use bias-adjusted values of the global growth rate based on measurements of atmospheric CO_2 made by the Scripps Institution of Oceanography at the Mauna Loa Observatory, Hawaii (Keeling et al., 1976; full period of coverage 1758-2024). Bias adjustment of the Scripps data was performed in three sequential stages as follows:

- First, to correct for differences in the mean atmospheric concentration of CO_2 at Mauna Loa versus the globally averaged value, a constant of -0.231 ppm was added to all Scripps data to improve alignment of the "CO_2[trend]" values from the Scripps data with the "CO_2[trend]" values from the global NOAA data. The value of -0.231 ppm is the mean offset of "CO_2[trend]" at Mauna Loa from the global "CO_2[trend]" value during 1980-2000.
- Second, to correct for differences in the seasonality of atmospheric CO_2 concentrations at Mauna Loa versus globally, we shifted monthly anomalies between CO_2 concentration data and "trend" values

backward in time by one month in the Scripps data. This specifically corrects for the fact that peaks/troughs in the climatology of "CO_2[monthly_observation] - CO_2[trend]" at Mauna Loa occur 1 month earlier than peaks/troughs in the climatology of "CO_2[monthly_observation] - CO_2[trend]" in the global data from NOAA. A one-month shift to the Scripps data was found to optimally align the climatologies of "CO_2[monthly_observation] - CO_2[trend]" in the Scripps and global data.

- Third, to correct for the greater amplitude of seasonal anomalies at Mauna Loa from Scripps than the global data from NOAA, we apply a monthly multiplier that dampens the magnitude of monthly anomalies from "trend" values in the Scripps data. The monthly multiplier reduces values of "CO_2[monthly_observation] - CO_2[trend]" in the Scripps data to more closely match values of "CO_2[monthly_observation] - CO_2[trend]" in the NOAA global data.

For the period Jan 1750 to February 1958, we use bias-adjusted values of the global growth rate based on measurements of atmospheric CO_2 from air trapped in ice at Law Dome (Joos and Spahni, 2008; full period of coverage 1750-2004). Bias adjustments were made to improve alignment with the post-1980 time series of data from Scripps and NOAA, and were performed in two sequential stages as follows:

- First, a constant of 0.973 was added to all data from Law Dome to improve alignment with the Scripps data (which had already been bias-corrected as described above). The constant of 0.973 is the mean offset of CO_2 annual values (annual mean in the case of the Scripps data) in the period 1958-1979.
- Second, the climatology of "CO_2[monthly_observation] - CO_2[trend]" from the period 1958-2000 was superimposed on the data from Law Dome (note that the 1958-2000 data includes both Scripps and NOAA data, combined as described above). To achieve this, a spline interpolation was fitted to downscale annual observations from CO_2 concentration from Law Dome to monthly values of "CO_2[trend]" and the climatological seasonality of "CO_2[monthly_observation] - CO_2[trend]" from 1958-2000) was then added to the interpolated values of "CO_2[trend]".

S.8 Processes not included in the global carbon budget

S.8.1 Contribution of anthropogenic CO and CH_4 to the global carbon budget

Equation (1) includes only partly the net input of CO_2 to the atmosphere from the chemical oxidation of reactive carbon-containing gases from sources other than the combustion of fossil fuels, such as: (1) cement process emissions, since these do not come from combustion of fossil fuels, (2) the oxidation of fossil fuels, (3) the assumption of immediate oxidation of vented methane in oil production. However, it omits any other anthropogenic carbon-containing gases that are eventually oxidised in the atmosphere, forming a diffuse source of CO_2, such as anthropogenic emissions of CO and CH_4. An attempt is made in this section to estimate their magnitude and identify the sources of uncertainty. Anthropogenic CO emissions are from incomplete fossil fuel and biofuel burning and deforestation fires. The main anthropogenic emissions of fossil CH_4 that matter for the global (anthropogenic) carbon budget are the fugitive emissions of coal, oil and gas sectors (see below). These emissions of CO and CH_4 contribute a net addition of fossil carbon to the atmosphere.

In our estimate of E_{FOS} we assumed (Section 2.1.1) that all the fuel burned is emitted as CO_2, thus CO anthropogenic emissions associated with incomplete fossil fuel combustion and its atmospheric oxidation into CO_2 within a few months are already counted implicitly in E_{FOS} and should not be counted twice (same for E_{LUC}

and anthropogenic CO emissions by deforestation fires). The diffuse atmospheric source of CO_2 deriving from anthropogenic emissions of fossil CH_4 is not included in E_{FOS}. In reality, the diffuse source of CO_2 from CH_4 oxidation contributes to the annual CO_2 growth. Emissions of fossil CH_4 represent 30% of total anthropogenic CH_4 emissions (Saunois et al. 2020; their top-down estimate is used because it is consistent with the observed CH_4 growth rate), that is 0.083 GtC yr^{-1} for the decade 2008-2017. Assuming steady state, an amount equal to this fossil CH_4 emission is all converted to CO_2 by OH oxidation, and thus explain 0.083 GtC yr^{-1} of the global CO_2 growth rate with an uncertainty range of 0.061 to 0.098 GtC yr^{-1} taken from the min-max of top-down estimates in Saunois et al. (2020). If this min-max range is assumed to be 2 σ because Saunois et al. (2020) did not account for the internal uncertainty of their minimum and maximum top-down estimates, it translates into a 1-σ uncertainty of 0.019 GtC yr^{-1}.

Other anthropogenic changes in the sources of CO and CH_4 from wildfires, vegetation biomass, wetlands, ruminants, or permafrost changes are similarly assumed to have a small effect on the CO_2 growth rate. The CH_4 and CO emissions and sinks are published and analysed separately in the Global Methane Budget and Global Carbon Monoxide Budget publications, which follow a similar approach to that presented here (Saunois et al., 2020; Zheng et al., 2019).

S.8.2 Contribution of other carbonates to CO_2 emissions

Although we do account for cement carbonation (a carbon sink), the contribution of emissions of fossil carbonates (carbon sources) other than cement production is not systematically included in estimates of E_{FOS}, except for Annex I countries and lime production in China (Andrew and Peters, 2025). The missing processes include CO_2 emissions associated with the calcination of lime and limestone outside of cement production. Carbonates are also used in various industries, including in iron and steel manufacture and in agriculture. They are found naturally in some coals. CO_2 emissions from fossil carbonates other than cement not included in our dataset are estimated to amount to less than 0.5% of E_{FOS} (estimated based on Crippa et al., 2019).

S.8.3 Anthropogenic carbon fluxes in the land-to-ocean aquatic continuum

The approach used to determine the global carbon budget refers to the mean, variations, and trends in the perturbation of CO_2 in the atmosphere, referenced to the pre-industrial era. Carbon is continuously displaced from the land to the ocean through the land-ocean aquatic continuum (LOAC) comprising freshwaters, estuaries, and coastal areas (Bauer et al., 2013; Regnier et al., 2013). A substantial fraction of this lateral carbon flux is entirely 'natural' and is thus a steady state component of the pre-industrial carbon cycle. We account for this pre-industrial flux where appropriate in our study (see Supplement S.3). However, changes in environmental conditions and land-use change have caused an increase in the lateral transport of carbon into the LOAC – a perturbation that is relevant for the global carbon budget presented here.

The results of the analysis of Regnier et al. (2013) can be summarised in two points of relevance for the anthropogenic CO_2 budget. First, the anthropogenic perturbation of the LOAC has increased the organic carbon export from terrestrial ecosystems to the hydrosphere by as much as 1.0 ± 0.5 GtC yr^{-1} since pre-industrial times, mainly owing to enhanced carbon export from soils. Second, this exported anthropogenic carbon is partly respired through the LOAC, partly sequestered in sediments along the LOAC and to a lesser extent, transferred to the open ocean where it may accumulate or be outgassed. The anthropogenic CO_2 outgassing from the LOAC

was recently estimated at 0.34 ± 0.26 GtC yr^{-1} (Regnier et al., 2022; Tian et al., 2023), a significant fraction originating from the lateral displacement of CO_2 produced by soil heterotrophic respiration to the aquatic system. The inclusion of LOAC related anthropogenic CO_2 fluxes should affect estimates of S_{LAND} and S_{OCEAN} in Eq. (1) but does not affect the other terms. The GOBMs and DGVMs used in the global carbon budget do not include a representation of the anthropogenic perturbation of LOAC CO_2 fluxes. Here in GCB2025, we apply a posteriori correction of -0.07 GtC yr^{-1} to the S_{LAND} estimate over the 2015-2024 period as assessed in (Friedlingstein et al. 2025b).

Supplementary Tables

Table S1. Comparison of the processes included in the bookkeeping method and DGVMs in their estimates of ELUC and SLAND. See Table 4 for model references. All models include deforestation and forest regrowth after abandonment of agriculture (or from afforestation activities on agricultural land). Processes relevant for ELUC are only described for the DGVMs used with land-cover change in this study.

	Bookeeping models			**DGVMs**																					
	BLUE	OSCAR	LUCE	CABLE-POP	CLASSIC	CLM6.0	CLM-FATES	DLEM	EDv3	ELM	ELM-FATES	GDSTEM	IBIS	iMAPLE	ISAM	JSBACH	JULES-ES	LPJ-GUESS	LPJmL	LPJ-EOSIM	LPX-Bern	ORCHIDEEv3	SDGVM	VISIT	VISIT-UT	CARDAMOM
Processes relevant for ELUC																									
Wood harvest and forest degradation (a)	yes	yes	yes	yes	no	yes	yes	yes	yes	yes	yes	yes	yes	no	yes	yes	no	yes (d)	no	yes	no (c)	yes	no	yes	yes	yes (R+L)
Shifting cultivation / Subgrid scale transitions	yes	yes	yes	yes	no	yes	yes	yes	yes	yes	yes	yes	yes	no	no	yes	no	yes	no	yes	no (c)	no	no	yes	no	no
Cropland harvest (removed, R, or added to litter, L)	yes (R) (i)	yes (R)	yes (R) (i)	yes (R)	yes (k)	yes (R+L)	no	yes	yes (R+L)	yes (k)	no	yes (R+L)	yes (R)	yes (k)	yes	yes (R+L)	yes (R)	yes (R)	yes (R+L)	yes (k)	yes (R)	yes (R)	yes (R)	yse (R)	yes (R)	no
Peat fires	yes (j)	yes (j)	yes (j)	no	no	yes	no	yes	no	no	no	no	no	no	no	no	no	no	no	no	no	no	no	no	no	yes (l)
fire as a management tool	yes (i)	yes (g)	yes(i)	no	no	no	no	yes	no	no	no	no	no	no	no	no	no	no	no	no	no	no	no	no	no	yes (l)
N fertilisation	yes (i)	yes (g)	yes(i)	no	yes	yes	no	yes	no	no	no	yes	yes	no	yes	no	yes(h)	yes	yes	no	yes	yes	no	no	yes	no
tillage	yes (i)	yes (g)	yes(i)	no	yes (f)	yes	no	yes	no	no	no	no (c)	no	no	no	no	no	yes	yes	no	no	yes (f)	no	no	no	no
irrigation	yes (i)	yes (g)	yes(i)	no	no	yes	no	yes	no	no	no	yes	no	no	yes	no	no	yes	yes	no	no	no	no	no	no	no
wetland drainage	yes (i)	yes (g)	yes(i)	no	no	no	no	no	no	no	no	no	no	no	yes	no	no	no	no	no	no	no	no	no	no	no
erosion	yes (i)	yes (g)	yes(i)	no	no	no	no	yes	no	no	no	no	yes	no	no	no	no	no	no	no	no	no	no	yes	yes	no
peat drainage	yes (j)	yes (j)	yes (j)	no	no	no	no	no	no	no	no	no	no	no	no	no	no	no	no	no	no	no	no	no	no	no

Grazing and mowing Harvest (removed, R, or added to litter, L)	yes (R) (i)	yes (R)	yes (r) (i)	yes (R)	no	no	yes (R)	no	yes (R+L)	no	yes (R)	yes (R+L)	yes	no	yes (R, L)	yes (k)	no	yes (R)	yes (R+L)	yes (k)	no	no	no	no	no	no
Processes also relevant for SLAND (in addition to CO2 fertilisation and climate)																									
ecosystem demography (ED) / vegetation competition (VC)				yes (ED), No (VC)	no	no	yes(ED)	no	yes	no	yes(ED)	no	yes ED, no VC	no	no ED, yes VC	no (VC (c))	No ED, Yes VC	yes	no ED, yes VC	yes	no ED, yes VC	Some ED no VC	yes (ED), No (VC)	no	no	no
Fire simulation and/or suppression	N.A.	N.A.	N.A.	no	yes	yes	yes	no	yes	yes	yes	no	yes	no	no	yes	yes	yes	yes	yes	yes	no	yes	yes	yes	yes (l)
Carbon-nitrogen interactions, including N deposition	N.A.	N.A.	N.A.	yes	yes	yes	no	yes	no	yes	no	yes	yes	no (e)	yes	yes	yes	yes	yes	no	yes	yes	yes (b)	no	no	no
Separate treatment of direct and diffuse solar radiation	N.A	N.A	N.A	yes	no	yes	yes	no	no	yes	yes	no	yes	yes	no	no	yes	no	no	no	no	no	yes (k)	yes (k)	yes (k)	no

(a) Refers to the routine harvest of established managed forests rather than pools of harvested products.

(b) Limited. Nitrogen uptake is simulated as a function of soil C, and Vcmax is an empirical function of canopy N. Does not consider N deposition.

(c) Available but not active.

(d) without the LUH2 secondary mature, young, and non-forest harvest fractions

(f) Tillage is represented over croplands by increased soil carbon decomposition rate and reduced humification of litter to soil carbon.

(g) as far as the DGVMs that OSCAR is calibrated to include it

(h) perfect fertilisation assumed, i.e. crops are not nitrogen limited and the implied fertiliser diagnosed

(i) Process captured implicitly by use of observed carbon densities.

(j) Emissions added from external datasets.

(k) Diffuse fraction calculated internally, not from external dataset

(l) Fire occurance added from external dataset, but C impact simulated.

1081

1082
1083

Table S2. Comparison of the processes and model set up for the Global Ocean Biogeochemistry Models for their estimates of SOCEAN. See Table 4 for model references.

	NEMO-PlankTOM12	NEMO4.2-PISCES (IPSL)	MICOM-HAMOCC (NorESM-OCv1.2)	MPIOM-HAMOCC6	FESOM-2.1-REcoM3	NEMO3.6-PISCESv2-gas (CNRM)	MOM6-COBALTv3 (Princeton)	CESM-ETHZ	MRI-ESM2-4	ACCESS (CSIRO)
Model specifics										
Physical ocean model	NEMOv3.6-ORCA2	NEMOv4.2-eORCA1L75	MICOM (NorESM-OCv1.2)	MPIOM	FESOM-2.1	NEMOv3.6-GELATOv6-eORCA1L75	MOM6-SIS2	CESMv1.3 (ocean model based on POP2)	MRI.COMv5	MOM5
Biogeochemistry model	PlankTOM12	PISCESv2	HAMOCC (NorESM-OCv1.2)	HAMOCC6	REcoM-3	PISCESv2-gas	COBALTv3	BEC (modified & extended)	NPZD+Fe	WOMBAT
Horizontal resolution	2° lon, 0.3 to 1.5° lat	1° lon, 0.3 to 1° lat	1° lon, 0.17 to 0.25 lat	1.5°	unstructured mesh, 20-120 km resolution (CORE mesh)	1° lon, 0.3 to 1° lat	1° lon, 0.5-1° lat (360x210)	1.125° lon, 0.53° to 0.27° lat	1.0° lon, 0.3 to 0.5° lat	1°x1° with enhanced latitudinal resolution in the tropics and high-lat Southern Ocean
Vertical resolution	31 levels	75 levels, 1m at the surface	51 isopycnic layers + 2 layers representing a bulk mixed layer	40 levels	46 levels, 10 m spacing in the top 100 m	75 levels, 1m at surface	75 levels hybrid coordinates, 2m at surface	60 levels	60 levels with 1-level bottom boundary layer	50 levels, 20 in the top 200m
Total ocean area on native grid (km2)	3.6080E+08	3.6360E+08	3.6006E+08	3.6598E+08	3.6435E+08	3.6270E+14	3.6137E+14	3.5926E+08	3.6094E+08	3.6134E+08
Gas-exchange parameterization	Wanninkhof et al (1992)	Orr et al., 2017	Orr et al., 2017, but with a=0.337	Orr et al., 2017	Orr et al., 2017	Orr et al., 2017; Wanninkhof et al. 2014	Deike et al., (2025) wind-wave-bubble formulation	Wanninkhof (1992, coefficient a scaled down to 0.31)	Orr et al., 2017	Wanninkhof et al (1992)
CO2 chemistry routines	OCMIP2 (Orr et al. 2017)	mocsy	Following Dickson et al. 2007	Ilyina et al. (2013) adapted to comply with OMIP protocol (Orr et al., 2017)	mocsy	mocsy	mocsy	OCMIP2 (Orr et al. 2017)	mocsy	OCMIP2 (Orr et al. 2017)
River input (PgC/yr) (organic/inorganic DIC)	0.723 / -	0.9167 (0.2577 / 0.659)	0	0.77 / -	0 / 0	0.611 / -	0.2139 / 0.7119	0.33 / -	0 / 0	0/0
Net flux to sediment (PgC/yr) (organic/other)	0.723 / -	0.3997 (0.0889 / 0.3138)	around 0.54 / -	0.71/-	0 / 0	around 0.656 / -	~0.166 / ~0.145 (CaCO3)	0.21 / -	0 / 0	0/0
SPIN-UP procedure										
Initialisation of carbon chemistry	GLODAPv2 (preindustrial DIC)	GLODAPv2 (preindustrial DIC)	GLODAPv1 (preindustrial DIC)	initialization from previous simulation	GLODAPv2 (preindustrial DIC)	GLODAPv2	GLODAPv2 (Alkalinity, DIC)	GLODAPv2 (preindustrial DIC)	GLODAPv2 (preindustrial DIC)	GLODAPv1 preindustrial DIC
Preindustrial spin-up prior to 1850	spin-up 1750-1940	~300 yrs with xCO2=278ppm	1000 year spin up (prior to 1762)	~2000 years	189 years	long spin-up (> 1000 years) from 1750 fixed conditions	Spin-up 792 years before the year 1766 with xCO2=278	500 years before year 1780 with xCO2 = 278	1925 years with xCO2 = 278	1200+ years

Atmospheric forcing fields and CO2										
Atmospheric forcing for (i) pre-industrial spin-up, (ii) spin-up 1850-1958 for simulation B, (iii) simulation B	looping ERA5 year 1990	(i) and (ii) looping first ten years (1958-1967) of JRA55-do-v1.4 (spin-up and 1750-1939) ; (iii) looping ten years (1958-1967) of ERA5 (1940-2024)	CORE-I (normal year) forcing (i, ii, iii)	OMIP climatology (i), NCEP year 1957 (ii,iii)	JRA55-do v.1.4.0 repeated year 1961 (i, ii), ERA5 hourly (iii)	JRA55-do-v1.5.0 full reanalysis (i) cycling year 1958 (ii,iii)	ERA5 hourly loop over 1958-1969 (i, ii, iii)	(i, ii, iii): ERA5 NYF (mean of 1958-2024 with 2001 anomalies, with a temporal resolution of 3h)	JRA-3Q repeat year 1990/91 (01May1990 to 30Apr1991) (i, ii, iii)	(i) 800+ years CORE spinup. 750 years with JRA55-do 1990/1991 and 250+ years of cycling ERA5 1958, (ii) and (iii) cycling ERA5 1958.
Atmospheric CO2 for control spin-up 1850-1958 for simulation B, and for simulation B	constant 278ppm; converted to pCO2 temperature formulation (Sarmiento et al., 1992)	xCO2 of 278ppm, converted to pCO2 with constant sea-level pressure and water vapour pressure	xCO2 of 278ppm, converted to pCO2 with sea-level pressure and water vapour pressure	xCO2 of 278ppm, no conversion to pCO2	xCO2 of 278ppm, converted to pCO2 with sea-level pressure and water vapour pressure	xCO2 of 278 ppm, converted to pCO2 with constant sea-level pressure and water vapour pressure	xCO2 of 278ppm, converted to pCO2 with sea-level pressure and water vapour pressure	xCO2 = 278 ppm, converted to pCO2 with atmospheric pressure, and water vapour pressure	xCO2 of 278ppm, converted to pCO2 with water vapour and sea-level pressure (JRA-3Q repeat year 1990/91)	xCO2 of 278ppm, converted to pCO2 with sea-level pressure
Atmospheric forcing for historical spin-up 1850-1958 for simulation A (i) and for simulation A (ii)	1750-1947: looping ERA5 year 1990; 1948-2023: ERA5	(i) looping first ten years (1958-1967) of JRA55-do-v1.4 (1750-1939) ; (ii) full ERA5 reanalysis (1940-2024)	CORE-I (normal year) forcing; from 1948 onwards NCEP-R1 with CORE-II corrections	NCEP 6 hourly cyclic forcing (10 years starting from 1948, i), 1948-2021: transient NCEP forcing	JRA55-do-v1.4.0 repeated year 1961 (i), ERA5 hourly (ii)	JRA55-do cycling year 1958 (i), JRA55-do-v1.5.0 from 1958 to 2023 (ii), JRA55-do-v1.5.0 scaled on ERA5 hourly for all scalars fields (e.g. T2m) for 2024	ERA5 hourly loop over 1958-1969 (i), ERA5 hourly ii)	(i, ii): ERA5 at 3h resolution, repeat cycle 1958-2024	1640-1957: repeated cycle JRA-3Q 1948-2024 (i), 1958-2024 (ii)	(i) cycling ERA5 1958, (ii) ERA5 for 1958-2024.
Atmospheric CO2 for historical spin-up 1850-1958 for simulation A (i) and simulation A (ii)	xCO2 provided by the GCB; converted to pCO2 temperature formulation (Sarmiento et al., 1992), monthly resolution (i, ii)	xCO2 as provided by the GCB, global mean, annual resolution, converted to pCO2 with sea-level pressure and water vapour pressure (i, ii)	xCO2 as provided by the GCB, converted to pCO2 with sea level pressure (taken from the atmospheric forcing) and water vapor correction (i, ii)	transient monthly xCO2 provided by GCB, no conversion (i, ii)	xCO2 as provided by the GCB, converted to pCO2 with sea-level pressure and water vapour pressure, global mean, monthly resolution (i, ii)	xCO2 as provided by the GCB, converted to pCO2 with constant sea-level pressure and water vapour pressure, global mean, yearly resolution (i, ii)	xCO2 as provided by GCB, converted to pCO2 with sea-level pressure and water vapour pressure, global mean, yearly resolution (i, ii)	xCO2 as provided by the GCB in 2025 (from 1780 onward), converted to pCO2 with locally determined atm. pressure, and water vapour pressure (i, ii)	xCO2 as provided by GCB, converted to pCO2 with water vapour and sea-level pressure (i, ii).	xCO2 as provided by the GCB, converted to pCO2 with sea-level pressure

Table S3: Description of ocean *f*CO2-products used for assessment of SOCEAN. See Table 4 for references.

	Jena-MLS	**VLIZ-SOMFFN**	**CMEMS-LSCE-FFNN**	**UExP-FNN-U (previously Watson et al.)**	**NIES-ML3**	**JMA-MLR**	**OceanSODA-ETHZv2**	**LDEO HPD**	**CSIR-ML6**
Method	Spatio-temporal interpolation (version oc_v2023). Spatio-temporal field of ocean-internal carbon sources/sinks is fit to the SOCATv2022 pCO2 data. Includes a multi-linear regression against environmental drivers to bridge data gaps,	A feed-forward neural network (FFN) determines non-linear relationship between SOCAT pCO2 measurements and environmental predictor data for 16 biogeochemical provinces (defined through a self-organizing map, SOM) and is used to fill the existing data gaps.	An ensemble of neural network models trained on 100 subsampled datasets from SOCAT and environmental predictors. The models are used to reconstruct sea surface fugacity of CO2 and convert to air-sea CO2 fluxes	A self-organising map feed forward neural network (SOM-FNN) implementation using SOCATv2025 recalculated to the subskin temperature (ESA CCI v3 bias corrected to surface drifter data following recommendations in Dong et al. 2022) of the ocean as measured by satellites (Goddijn-Murphy et al, 2015). Flux calculation corrected for the cool and salty surface skin. Monthly skin temperature calculated from ESA CCI v3 (Embury et al. 2024) with the cool skin difference calculated using NOAA COARE 3.5. Flux calculations completed using FluxEngine (Shutler et al., 2016; Holding et al., 2019).	The ensemble of a random forest, a gradient boost machine, and a feed forward neural network trained on SOCAT 2025 fCO2 and environmental predictor variables. The interannual trend of fCO2 was estimated first by the decadal trend of atmospheric CO2 and then corrected by a so-called leave-one-year-out validation method. The trend was used to normalize fCO2 to the mid year of 1982-2024 for model training. The monthly fCO2 maps were reconstructed using model prediction and the trend.	Fields of total alkalinity (TA) were estimated by using a multiple linear regressions (MLR) method based on GLODAPv2.2023 and satellite observation data. SOCATv2025 recalculated fCO2 data were converted to dissolved inorganic carbon (DIC) with the TA. Fields of DIC were estimated by using a MLR method based on the DIC and satellite observation data	OceanSODA-ETHZv2 is a two-phase machine learning approach. In phase 1, we estimate the ΔfCO2 8-day seasonal cycle climatology with a Gradient Boosted Decision Tree which is used as a predictor in the next phase. In phase 2, we predict the non-thermal component of ΔfCO2 at a 8-day by 0.25° by 0.25° resolution with a two-layer fully-connected neural network using 35 ensemble members. The atmospheric CO2 and non-thermal component are added back to the result.	Based on fCO2-misfit between observed fCO2 and 10 global carbon budget GOBMs. The eXtreme Gradient Boosting method links this misfit to environmental observations to reconstruct the model misfit across all space and time., which is then added back to the model-based fCO2 estimate. The final reconstruction of surface fCO2 is the average across the 10 reconstructions. A climatology of the misfits calculated for the years 2000-2023 is used as an offset for years prior to 1982 when no/limited envionmental observations are available to train the ML algorithm.	An ensemble average of six machine-learning models, where each model is constructed with a two-step clustering-regression approach to determine a non-linear relationship between SOCAT fCO2 measurements and environmental proxy variables, and it used to fill the existing data gaps. The clustering step consists of two methods: the Mini-batch K-means clustering and the extended Fay and McKinley (2014) biomes. The regression step consists of three methods: Gradient Boosting Machine, Support Vector Regression, and Feed-forward Neural Network.
Gas-exchange parameterization	Wanninkhof 1992. Transfer coefficient k scaled to match a global mean transfer rate of 16.5 cm/hr by (Naegler, 2009)	Wanninkhof 2014. Transfer coefficient k scaled to match a global mean transfer rate of 16.5 cm/hr (Naegler, 2009)	Wanninkhof 2014. Transfer coefficient k scaled to match a global mean transfer rate of 16.5 cm/hr (Naegler, 2009)	Nightingale et al 2000	Wanninkhof, 2014. Transfer coefficient k scaled to match a global mean transfer rate of 16.5 cm/hr in 1990-2019 (Fay et al., 2021)	Wanninkhof., 2014. Transfer coefficient k scaled to match a global mean transfer rate of 16.5 cm/hr (Naegler, 2009; Fay, Gregor et al. 2021)	Wanninkhof 1992, averaged and scaled for three reanalysis wind data, to a global mean 16.5 cm/hr (after Naegler 2009; Fay & Gregor et al. 2021)	Wanninkhof 1992 parameterization. Transfer coefficient k scaled to match a global mean transfer rate of 16.5 cm/hr (Naegler, 2009)	Wanninkhof 1992, averaged and scaled for three reanalysis wind data, to a global mean 16.5 cm/hr (after Naegler 2009; Fay & Gregor et al. 2021)
Wind product	JMA55-do reanalysis	ERA 5	ERA5	CCMP3.1	ERA5	JRA3Q	ERA5	ERA5	ERA5

Spatial resolution	2.5 degrees longitude x 2 degrees latitude regridded to 1x1 degree	1x1 degree	0.25x0.25 degree regridded to 1x1 degree	1x1 degree	1x1 degree	1x1 degree	0.25x0.25 degree regridded to 1x1 degree	1x1 degree	1x1 degree
Temporal resolution	daily	monthly	monthly	monthly	monthly	monthly	8-daily regridded to monthly	monthly	monthly
Atmospheric CO2	Spatially and temporally varying field based on atmospheric CO2 data from 169 stations (Jena CarboScope atmospheric inversion)	Spatially varying 1x1 degree atmospheric pCO2_wet calculated from the NOAA ESRL marine boundary layer xCO2 and NCEP sea level pressure with the moisture correction by Dickson et al 2007.	Spatially and monthly varying fields of atmospheric pCO2 computed from CO2 mole fraction (CO2 atmospheric inversion from the Copernicus Atmosphere Monitoring Service), and atmospheric dry-air pressure which is derived from monthly surface pressure (ERA5) and water vapour pressure fitted by Weiss and Price 1980	Atmospheric fCO2 (wet) calculated from NOAA marine boundary layer XCO2(atm) and ERA5 sea level pressure, with pH2O calculated from Cooper et al. (1998). 2024 XCO2 marine boundary values were not available at submission so we used preliminary values, estimated from 2023 values and increase at Mauna Loa.	NOAA Greenhouse Gas Marine Boundary Layer Reference. https://gml.noaa.gov/ccgg/mbl/mbl.html	Atmospheric xCO2 fields of JMA-GSAM inversion model (Maki et al. 2010) were converted to pCO2 by using JRA3Q sea level pressure. 2024 xCO2 fields were not available at this stage, and we used Cape Grim and Mauna Loa xCO2 increments from 2023 to 2024 for the southern and northern hemispheres, respectively.	NOAA's marine boundary layer (MBL) product (1980 - 2023) is used for atmospheric xCO2. For the year 2024, a linear regression is performed between deseasonalised Mauna Loa (1970 - 2025) and MBL data for each latitude of the latter. The mean seasonal cycle is added back to the interpolated data for 2024. The MBL xCO2 (now 1980 - 2024) is linearly interpolated onto a 0.25°x0.25° grid and resampled from weekly to 8-daily. xCO2 is multiplied by ERA5 mean sea level pressure, where the latter corrected for water vapour pressure using Dickson et al. (2007). These results are regridded to a monthly 1x1 degree pCO2atm.	NOAA's marine boundary layer (MBL) surface xCO2 product is linearly interpolated to a 1x1° monthly grid for years 1979-2023. Prior to 1979, calculating an offset between the MBL and Mauna Loa seasonal climatologic xCO2 values for a subset of common years (1979-1989) yields a mean seasonality difference which is then applied to the Mauna Load time series. This results in a latitudinal-varying xCO2 time series for years prior to 1979, based on the long term trajectory estimated at Mauna Loa. Monthly 1x1 degree xCO2 is multiplied by ERA5 mean sea level pressure, with the correction for water vapour pressure using Dickson et al. 2007, using ERA5 SST and EN4 SSS. FInally converted to fCO2 using ERA5 SST and SLP.	NOAA's marine boundary layer product for xCO2 is linearly interpolated onto a 1x1 degree grid and resampled from weekly to monthly. ERA5 mean sea level pressure is used, where the latter corrected for water vapour pressure using Dickson et al. (2007).
Total ocean area on native grid (km2)	3.63E+08	3.63E+08	3.50E+08	361000000	329000000	315000000	354615000	3.586 E+8	363150000

method to extend product to full global ocean coverage		Arctic and marginal seas added following Landschützer et al. (2020). No coastal cut.				Fay & Gregor et al. 2021	Coverage of the global ice free ocean (ice frac < 0.9)	Based on method in Fay & Gregor et al. 2021. Gaps were filled with monthly climatology (Landschützer et al. 2020) scaled for interannual variability based on the temporal evolution of this product for all years.	Method has near full coverage

1098

1099
1100

Table S4. Comparison of the inversion set up and input fields for the atmospheric inversions. Atmospheric inversions see the full CO2 fluxes, including the anthropogenic and pre-industrial fluxes. Hence they need to be adjusted for the pre-industrial flux of CO2 from the land to the ocean that is part of the natural carbon cycle before they can be compared with SOCEAN and SLAND from process models. See Table 4 for references.

Name	**Jena CarboScope**	**Carbon-Tracker Europe (CTE)**	**NISMON-CO2**	**CT-NOAA**	**CMS-Flux**	**Copernicus Atmosphere Monitoring Service (CAMS)**	**GONGGA**	**COLA**	**GCASv2**	**UoE**	**MIROC-ACTM**	**NTFVAR**	**THU**	**NISMON-CO2_GOSAT**
Version number	r76nbetEXToc_v2025	v2025	v2025.1	CT2025	v2025	FT25r1	v2025	v2025	v2025	v2025	v2025	v2025	v2025	v2025.1
Flags														
Observations														
Atmospheric observations (a, b)	Flasks and hourly from various institutions (outliers removed by 2σ criterion)	Hourly resolution (well-mixed conditions) obspack GLOBALVIEWplus v8.0 and v10.1 and NRT_v10.1	Hourly resolution (well-mixed conditions) obspack GLOBALVIEWplus v10.1 and NRT_v10.1	Hourly resolution (well-mixed conditions) obspack GLOBALVIEWplus v9.1 and v10.1 and NRT_v10.1	OCO-2 V11.2 and obspack GLOBALVIEWplus v10.1 and NRT_v10.1	OCO-2 ACOS retrievals from NASA, v11.2	OCO-2 v11.2r data that were scaled to the WMO 2019 standard	Hourly resolution (well-mixed conditions) obspack GLOBALVIEWplus v10.1 and NRT_v10.1. And OCO-2_b11.2_LNLG	ACOS v11.2 OCO-2 XCO2 retrievals, scaled to the WMO 2019 standard	Hourly resolution (well-mixed conditions) obspack GLOBALVIEWplus v10.1 and NRT_v10.1	Hourly resolution (well-mixed conditions) obspack GLOBALVIEWplus v10.1 and NRT_v10.1 and JMA	Hourly resolution (well-mixed conditions) obspack GLOBALVIEWplus v9.0 and v10.1 and NRT_v10.1 and GOSAT XCO2 data NIES Level 2 product v03.05	OCO-2 v11.2r data that were scaled to the WMO 2019 standard	NIES GOSAT SWIR L2 Product ver03.05 that were taken only over land (GOSAT)
Period covered	1976-2024	2001-2024	1990-2024	2000-2024	2015-2024	2015-2024	2015-2024	2015-2024	2015-2024	2001-2024	2001-2024	2010-2024	2015-2024	2010-2024
Prior fluxes														

Biosphere and fires	Zero	SiB4-MERRA and GFAS	VISIT and GBEI	MiCASA v1 (includes GFEDv3)	CARDAMOM simulated fire emissions with GFED4.1 burned area before 2024, GFAS fire emissions in 2024	ORCHIDEE, GFEDv4.1s	ORCHIDEE-MICT and GFEDv4.1s	VEGAS + GFAS	BEPS and GFED4.1s	CASA v1.0, climatology after 2016 and GFED4.0	MiCASA and GFEDv4s	Zeng et al. 2020 and GFAS	SiB4.2 and GFEDv4.1s	VISIT and GBEI
Ocean	CarboScope oc_v2025	CarboScope v2022 and v2024	JMA global ocean mapping (Iida et al., 2021)	AOML-Extra Trees surface ocean pCO2	ECCO-Darwin and MOM6	CMEMS-LSCE-FFNN 2025	Takahashi climatology with a trend	Jena OC-v2024	JMA Ocean CO2 Map v2024 (Global) and v2025 (regional)	Takahashi climatology	Takahashi climatology	Zeng et al. 2022	Takahashi climatology with a trend	JMA global ocean mapping (Iida et al., 2021)
Fossil fuels (c)	GridFED v2025.1	GridFED 2023.1 and 2025.1	GridFED v2025.1	Miller	GridFED 2024.0 with an extrapolation to 2024-25 based on Carbonmonitor and NO2 retrievals	GridFED 2024.0 with an extrapolation to 2024-25 based on Carbonmonitor and NO2 retrievals	GridFED 2025.1	GridFEDv2024.0 and v2025.1	GridFEDv2025.1	GridFED 2025.1	GridFEDv2025.1	GridFEDv2025.1	GridFEDv2025.1	GridFED v2025.1
Transport and optimization														
Transport model	TM3	TM5	NICAM-TM	TM5	GEOS-CHEM	LMDZ v6	GEOS-Chem v12.9.3	GEOS-CHEM v13.0.2	MOZART-4	GEOS-CHEM	MIROC-ACTM	NIES-TM-FLEXPART	GEOS-Chem v12.2	NICAM-TM
Weather forcing	ERA5	ECMWF	JRA-3Q	ERA5	MERRA2	ECMWF	MERRA2	MERRA-2	GEOS5	MERRA	JRA-3Q	ERA5(NIES-TM)/JRA-55(FLEXPART)	GEOS-FP	JRA-3Q

Horizontal Resolution	Global 4°x6°	Global 3°x2°, Europe 1°x1°, North America 1°x1°	glevel-5 (~223 km)	Global 3°x2°, North America 1°x1°	Global 4°x5°	global ~90 km in the horizontal (hexagons)	Global 2°x2.5°	2°×2.5°	2.5°×1.875°	Global 2°x2.5°	2.8°×2.8°	NIES-TM 3.75°x3.75° and FLEXPART 0.1°x0.1°	Global 4° x 5°	glevel-5 (~223 km)
Optimization	Conjugate gradient (re-ortho-normalization)	5-week ensemble Kalman smoother	Variational	12-week ensemble Kalman smoother	Variational	Variational	Nonlinear least squares four-dimensional variation (NLS-4DVar)	Ensemble Kalman Filter (LETKF with CEnKF/AAPO)	Ensemble Kalman filter	Ensemble Kalman filter	Bayesian inversion, similar to that of Rayner et al. (Tellus, 1999)	Variational, M1QN3	Ensemble Kalman filter	Variational

(a) Schuldt et al. 2024. Multi-laboratory compilation of atmospheric carbon dioxide data for the period 1957-2023; obspack_co2_1_test_GLOBALVIEWplus_v10.1_2024-11-13; NOAA Earth System Research Laboratory, Global Monitoring Laboratory. http://doi.org/10.25925/20241101

(b) Schuldt et al. 2025. Multi-laboratory compilation of atmospheric carbon dioxide data for the period 2024; obspack_co2_1_NRT_v10.1_2025-02-07; NOAA Earth System Research Laboratory, Global Monitoring Laboratory. http://doi.org/10.25925/20250101.

(c) GCP-GridFED v2025.1 and earlier (Jones et al., 2025) are updates of the GCP-GridFED dataset presented by Jones et al. (2021b).

1101

1102

1103

1104

Table S5: Overview of the Earth System Models (ESMs) and the simulations.

Model	CanESM5	EC-Earth3-CC	IPSL-CM6A-CO2-LR	MIROC-ES2L	MPI-ESM1.2-LR	NorCPM-CC
Resolution Atmosphere	T63, 49 hybrid levels up to 1hPa	T255, 91 levels	2.5°x1.25°, 79 levels	T42, 40 levels	T63, 47 levels	2.5x1.875°, 32 levels
Resolution Ocean	1° refined meridionally to 1/3° near Equator, 45 levels	1°, 75 levels	1° (nominal), 75 levels	Tripolar (~1°), 62 levels	1.5°, 40 levels	1°, 53 sigma levels
Assimilation Atmosphere	ERA-Interim (Dee et al. 2011) from 1980 to 2018 and ERA5 (Hersbach et al. 2020) afterwards: full-field nudging of temperature, horizontal wind and specific humidity. Globally averaged atmospheric CO2 concentration at the lowest model level is constrained by prescribed values (Arora and Scinocca, 2016).	ERA5 (Hersbach et al. 2020) full-field	None	3D full field wind and T of JRA55 (Kobayashi et al. 2015) with the simplified IAU (Tatebe et al. 2012)	ERA-40 (Uppala et al. 2005) before 1979 and ERA5 (Hersbach et al. 2020) from 1980: Vorticity, divergence, log(p), T; full field with nudging	None

Assimilation Ocean	Nudging to 3D potential temperature and salinity from ORAS5 reanalysis (Zuo et al. 2019). Sea surface temperature relaxed to interpolated values from NOAA's OISSTv2 from Nov. 1981 to present, and NOAA's ERSSTv3 prior (Smith et al. 2008).	EN4 (Good et al. 2013) 3D nudging T and S with weaker nudging band around equator. SST and SSS restoring to ORAS5 (Zuo et al. 2019). Atmospheric forcing: DFS5.2 1958-1979 and ERA5 after 1980	Nudging towards SST (ERSSTv5) and SSS (EN4) using a restoring coefficient dependent on the mixed layer depth (Ortega et al. 2017)	3D full field T, S, and sea-ice concentration of an ocean objective analysis (Ishii and Kimoto 2009) with the simplified IAU (Tatebe et al. 2012)	EN4 (Good et al. 2013) 3D full field T and S with ensemble Kalmann filter (Brune et al. 2018)	ENKF anomaly assimilation of monthly T and S from EN4, monthly SST from HADISST during 1975-1981, and daily SST from OISSTv2 during 1982-2023
Assimilation Land	Indirectly through response of CLASS-CTEM to the data-constrained coupled ESM	LPJ-GUESS forced offline with ERA5 1979-2020 after preindustrial spinup+transient up to 1979	None	None	Indirectly initialized by atmospheric and oceanic data assimilation within the fully coupled ESM	None
Ensemble Size	10	10	10	10	10	10
Period of reconstruction	1960-2024	1980-2024	1960-2024	1960-2024	1960-2024	1975-2024
Hindcasts and forecasts	1 year starting from Jan. 1st 1980-2025	14 months starting from Nov.1st 1980-2024	1 year starting from Jan. 1st 1981-2025	14 months starting from Nov. 1st 1980-2024	14 months starting from Nov.1st 1980-2024	16 months starting from Nov. 1st 1980-2024
External forcings	The Coupled Model Intercomparison Project Phase 6 (CMIP6) historical (1960-2014) plus SSP2-4.5 baseline and CovidMIP two year blip scenario (after 2015) (Eyring et al. 2016; Lamboll et al. 2021). The CO2 emissions forcing from 2015 onward are substituted by GCP-GridFED (v2024.0, Jones et al., 2025), which is an update to Jones et al. (2021) , for all the models except for IPSL-CM6A-CO2-LR. The CO2 emissions forcing for year 2025 is an extension with the same emission of the year 2024. Note the difference in global integrated CO2 emissions between CMIP6 CovidMIP and GCP-GridFED in recent years is within the emission uncertainty.					

References	Swart et al. 2019; Sospedra-Alfonso et al. 2021	Döscher et al. 2021; Bilbao et al., 2021; Bernardello et al., 2024	Boucher et al. 2020	Watanabe et al. 2020	Mauritsen et al. 2019; Li et al. 2023	Tjiputra et al. 2020; Bethke et al. 2021

1105

1106

1107

Table S6. Comparison of the projection with realised fossil CO_2 emissions (EFOS). The 'Actual' values are first the estimate available using actual data (e.g., the actual 2020 value is from the 2021 budget) and the 'Projected' values refers to estimates made before the end of the year for each publication (e.g., the projected 2020 value is from the 2020 budget). Projections based on a different method from that described here during 2008-2014 are available in Le Quéré et al., (2016). All values are adjusted for leap years.

	World		China		USA		EU28 / EU27 (i)		India		Rest of World (ii)	
	Projected	Actual	Projected	Actual	Projected	Actual	Projected	Actual	Projected	Actual	Projected	Actual
2015 (a)	–0.6% (–1.6 to 0.5)	0.06%	–3.9% (–4.6 to –1.1)	–0.7%	–1.5% (–5.5 to 0.3)	–2.5%	–	–	–	–	1.2% (–0.2 to 2.6)	1.2%
2016 (b)	–0.2% (–1.0 to +1.8)	0.20%	–0.5% (–3.8 to +1.3)	–0.3%	–1.7% (–4.0 to +0.6)	–2.1%	–	–	–	–	1.0% (–0.4 to +2.5)	1.3%
2017 (c)	2.0% (+0.8 to +3.0)	1.6%	3.5% (+0.7 to +5.4)	1.5%	–0.4% (–2.7 to +1.0)	–0.5%	–	–	2.00% (+0.2 to +3.8)	3.9%	1.6% (0.0 to +3.2)	1.9%
2018 (d)	2.7% (+1.8 to +3.7)	2.1%	4.7% (+2.0 to +7.4)	2.3%	2.5% (+0.5 to +4.5)	2.8%	-0.7% (-2.6 to +1.3)	-2.1%	6.3% (+4.3 to +8.3)	8.0%	1.8% (+0.5 to +3.0)	1.7%
2019 (e)	0.5% (-0.3 to +1.4)	0.1%	2.6% (+0.7 to +4.4)	2.2%	-2.4% (-4.7 to -0.1)	-2.6%	-1.7% (-5.1% to +1.8%)	-4.3%	1.8% (-0.7 to +3.7)	1.0%	0.5% (-0.8 to +1.8)	0.5%
2020 (f)	-6.7%	-5.4%	-1.7%	1.4%	-12.2%	-10.6%	-11.3% (EU27)	-10.9%	-9.1%	-7.3%	-7.4%	-7.0%

2021 (g)	**4.8% (4.2% to 5.4%)**	**5.1%**	**4.3% (3.0% to 5.4%)**	**3.5%**	**6.8% (6.6% to 7.0%)**	**6.2%**	**6.3% (4.3% to 8.3%)**	**6.8%**	**11.2% (10.7% to 11.7%)**	**11.1%**	**3.2% (2.0% to 4.3%)**	**4.5%**
2022 (h)	**1.1% (0% to 1.7%)**	**0.9%**	**-1.5% (-3.0% to 0.1%)**	**0.9%**	**1.6% (-0.9% to 4.1%)**	**1.0%**	**-1.0% (-2.9% to 1.0%)**	**-1.9%**	**5.6% (3.5% to 7.7%)**	**5.8%**	**2.5% (0.1% to 2.3%)**	**0.6%**
2023 (j)	**1.1% (0.0% to 2.1%)**	**1.3%**	**4.0% (1.9% to 6.1%)**	**4.9%**	**-3.0% (-5% to -1%)**	**-3.3%**	**-7.4% (-9.9% to -4.9%)**	**-8.4%**	**8.2% (6.7% to 9.7%)**	**8.2%**	**0.4% (-1.4% to 2.3%)**	**0.7%**
2024 (k) GCB	**0.80% (-0.2% to 1.7%)**	**1.10%**	**0.10% (-1.7% to 1.9%)**	**0.70%**	**-0.90% (-2.1% to 0.3%)**	**-0.60%**	**-2.80% (-5.2% to -0.3%)**	**-2.60%**	**3.70% (3.3% to 4.0%)**	**4.00%**	**1.20% (0.7% to 3.2%)**	**1.90%**
2024 (k) CM	**0.80% (0.5% to 1.1%)**		**-0.80% (-1.3% to -0.4%)**		**1.30% (1.1% to 1.6%)**		**-4.50% (-5.4% to -3.6%)**		**5.00% (4.4% to 5.5%)**		**1.50% (-1.2% to 1.8%)**	

(a) Jackson et al. (2016) and Le Quéré et al. (2015a). (b) Le Quéré et al. (2016). (c) Le Quéré et al. (2018a). (d) Le Quéré et al. (2018b). (e) Friedlingstein et al., (2019), (f) Friedlingstein et al., (2020), (g) Friedlingstein et al., (2022a), (h) Friedlingstein et al., (2022b), (j) Friedlingstein et al., (2023), (k) Friedlingstein et al. (2025a), (l) This study

(i) EU28 until 2019, EU27 from 2020

(ii) From 2023, the projection for Rest of World is composed of separate projections for aviation bunkers, maritime bunkers, and all other countries.

(iii) The projection for the World includes the projection on cement carbonation

1108

Table S7 Comparison of the current year projection of GATM, SLAND and SOCEAN for the current year with the actual values since GCB2021. The 'actual' values are the estimate available using observations and comprehensive models/data streams (e.g., the actual 2023 value from the 2024 GCB budget publication) and the 'projected' values refers to estimates made before the end of the year for each publication (e.g., the projected 2024 value from the 2024 GCB budget publication). All units in GtC yr^{-1}.

	GATM		**SOCEAN**		**SLAND**	
	Projected	Actual	Projected	Actual	Projected	Actual
2021	5.3 ± 0.1	5.2 ± 0.2	2.9 ± 0.4	2.9 ± 0.4	3.3 ± 1.0	3.5 ± 0.9
2022	5.3 ± 0.4	4.6 ± 0.2	2.9 ± 0.4	2.8 ± 0.4	3.4 ± 0.9	3.8 ± 0.8
2023	5.1 ± 0.4	5.9 ± 0.2	2.9 ± 0.6	2.9 ± 0.4	2.9 ± 1.2	2.3 ± 1.0
2024	6.1 ± 0.3	7.9 ± 0.2	3.0 ± 0.6	3.4 ± 0.6	3.2 ± 1.5	1.9 ± 0.9

Note: the 2024 projections of SOCEAN and SLAND are not corrected as in the GCB2024, while the actual estimates are corrected, as in the present GCB2025. The uncorrected 2024 estimates of SOCEAN and SLAND are 3.2 ± 0.6 and 2.5 ± 0.9 GtC yr^{-1} respectively.

1119

Table S8 Attribution of fCO2 measurements for the year 2024 included in SOCATv2025 (Bakker et al., 2016, 2025) to inform ocean fCO2-based data products.

Platform Name	Regions	No. of measurements	Principal Investigators	No. of datasets	Platform Type
Allure of the Seas	Coastal	3,065	Wanninkhof, R.; Pierrot, D.	1	Ship
Arni Fridriksson	Arctic, North Atlantic, coastal	23,030	Benoit-Cattin, A.	3	Ship
Atlantic Explorer	North Atlantic, Tropical Atlantic, coastal	38,394	Bates, N. R.; Enright, M.	23	Ship
Bell M. Shimada	Coastal	32,166	Alin, S. R.; Feeley, R. A.	6	Ship
CCE1_122W_33N	Coastal	432	Sutton, A.; Send, U.; Ohman, M.	1	Mooring
CCE2_121W_34N	Coastal	703	Sutton, A.; Send, U.; Ohman, M.	1	Mooring
Celtic Explorer	Arctic, North Atlantic, coastal	49,799	Cronin, M.	5	Ship
Equinox	North Atlantic, Tropical Atlantic, coastal	2,125	Wanninkhof, R.; Pierrot, D.	2	Ship
F.G. Walton Smith	Coastal	28,714	Barbero, L.; Pierrot, D.; Wanninkhof, R.	15	Ship
Finnmaid	Coastal	287,640	Rehder, G.; Bittig, H.; Glockzin, M.	11	Ship
G.O. Sars	Arctic, North Atlantic, coastal	116,122	Skjelvan, I.	16	Ship
GAKOA_149W_60N	Coastal	487	Monacci, N.; Alin, S. R.; Battisti, R.; Bott, R.; Cross, J.; Maenner-Jones, S.; Musielewicz, S.; Osborne, J.; Sutton, A.	1	Mooring
Gordon Gunter	North Atlantic, Tropical Atlantic, coastal	50,247	Wanninkhof, R.; Pierrot, D.	9	Ship
Healy	Arctic, North Pacific, coastal	16,900	Sweeney, C.; Newberger, T.; McAuliffe, A. M.; Munro, D. R.	2	Ship
Henry B. Bigelow	Coastal	72,468	Wanninkhof, R., Pierrot, D.	10	Ship
Heron Island	Coastal	1,128	Tilbrook, B.	1	Mooring
Investigator	Southern Ocean	81,717	Tilbrook, B.; Akl, J.; Neill, C.	3	Ship
Kangaroo Island	Southern Ocean	1,343	Tilbrook, B.	1	Mooring
Keifu Maru II	North Pacific, Tropical Pacific, coastal	7,155	Enyo, K.	6	Ship
Laurence M. Gould	Southern Ocean	12,899	Sweeney, C.; Newberger, T.; Sutherland, S. C.; Munro, D. R.	2	Ship
Le Commandant Charcot	Arctic, North Atlantic, Tropical Atlantic, Southern Ocean, coastal	35,750	Wanninkhof, R.; Pierrot, D.	10	Ship
M2_164W_57N	Coastal	552	Monacci, N.; Sutton, A.	2	Mooring
Maria Island	Southern Ocean	1,236	Tilbrook, B.	1	Mooring
Marion Dufresne	Indian, Southern Ocean	9,559	Lo Monaco, C.; Metzl, N.	1	Ship
MV Oleander	North Atlantic, coastal	34,322	Bates, N. R.; Enright, M.	7	Ship
Nathaniel B. Palmer	Southern Ocean	42,354	Sweeney, C.; Newberger, T.; McAuliffe, A. M.; Munro, D. R.	6	Ship
New Century 2	North Pacific, Tropical Pacific, Southern Ocean, coastal	252,956	Nakaoka, S.-I.; Takao, S.	14	Ship
NG Islander 2	Tropial Pacific	55,333	Wanninkhof, R.; Pierrot, D.	15	Ship
Oshoro Maru V	North Pacific, coastal	4,275	Takafumi, A.; Nakaoka, S.-I.	6	Ship
Papa_145W_50N	North Pacific	1,711	Sutton, A.; Cronin, M.; Emerson, S.	1	Mooring
Quadra Island Field Station	Coastal	81,629	Evans, W.	1	Mooring

RV Neil Armstrong	North Atlantic, coastal	10,376	Theetaert, H.; Azetsu-Scott, K.; Pierrot, D.	2	Ship
RV Skagerak	Arctic, coastal	13,572	Leseurre, C.	1	Ship
Sea-Cargo Express	Coastal	52,931	Omar, A.; Kritensen, T. O.	5	Ship
Sikuliaq	Arctic, North Pacific, Tropical Pacific, coastal	64,663	Sweeney, C.; Newberger, T.; Munro, D. R.; Fay A. R.	18	Ship
Simon Stevin	Coastal	52,878	Gkritzalis, T.; Theetaert, H.; T'Jampens, M.	7	Ship
SOFS_142E_46S	Southern Ocean	775	Sutton, A.; Trull, T.	1	Mooring
Tangaroa	Tropical Pacific, Southern Ocean	145,095	Van de Velde, S.; Currie, K. I.	11	Ship
TAO170W_0N	Tropical Pacific	631	Sutton, A.	1	Mooring
Thomas G. Thompson	Tropical Pacific, Indian, Southern Ocean, coastal	18,058	Alin, S.R.; Feeley, R. A.	4	Ship
Trans Future 5	North Pacific, Tropical Pacific, Southern Ocean, coastal	200,905	Nakaoka, S.-I.; Takao, S.; Nojiri, Y.	16	Ship
Tukuma Arctica	North Atlantic, coastal	37,839	Becker, M.; Olsen, A.	14	Ship
Victor Angelescu	Southern Ocean	46,031	Berghoff, C., Arbilla, L., Veccia, M., Maenza, R. A.	5	Ship
WHOTS_158W_23N	Tropical Pacific	1,258	Sutton, A., Weller, R., Pleuddemann, A.	1	Mooring

1120
1121

1122

Table S9. Aircraft measurement programs archived by Cooperative Global Atmospheric Data Integration Project (Schuldt et al. 2024 and 2025) that contribute to the evaluation of the atmospheric inversions (Figure S13).

Site code	Measurement program name in Obspack	Specific doi	Data providers
AAO	Airborne Aerosol Observatory, Bondville, Illinois	https://doi.org/10.15138/39HR-9N34	Sweeney, C.;
ABOVE	Carbon in Arctic Reservoirs Vulnerability Experiment (CARVE)	https://doi.org/10.3334/ORNLDAAC/1404	Sweeney, C.; McKain, K.; Karion, A.; Miller, J.B.; Miller, C.E.
ACG	Alaska Coast Guard	https://doi.org/10.15138/39HR-9N34	McKain, K.; Karion, A.; Sweeney, C.
ACT	Atmospheric Carbon and Transport - America	https://doi.org/10.3334/ORNLDAAC/1593	Sweeney, C.; Baier, B; Davis, K.
AIRCORENOAA	NOAA AirCore	https://doi.org/10.15138/6AV0-MY81	Sweeney, C.; Baier, B.
AJAX	Alpha Jet Atmospheric eXperiment (AJAX)	https://doi.org/10.5194/essd-15-2375-2023	Emma L. Yates (NASA-Ames) AND Laura T. Iraci (NASA-Ames) AND Susan S. Kulawik (NASA-Ames) AND Ju-Mee Ryoo (NASA-Ames) AND Josette E. Marrero (NASA-Ames) AND Caroline L. Parworth (NASA-Ames) AND Jason M. St.Clair (NASA-GSFC) AND Thomas F. Hanisco (NASA-GSFC) AND Thao Paul V. Bui (NASA-Ames) AND Cecilia S. Chang (NASA-Ames) AND Jonathan M. Dean-Day (NASA-Ames)
ALF	Alta Floresta	https://doi.org/10.1594/PANGAEA.949643	Gatti, L.V.; Gloor, E.; Miller, J.B.; Peters, W.
AOA	Aircraft Observation of Atmospheric trace gases by JMA	doi:10.5194/amt-6-1257-2013	Shinya Takatsuji
BGI	Bradgate, Iowa	https://doi.org/10.15138/39HR-9N34	Sweeney, C.;
BNE	Beaver Crossing, Nebraska	https://doi.org/10.15138/39HR-9N34	Sweeney, C.;
BRZ	Berezorechka, Russia		Motoki Sasakawa, Toshinobu Machida
CAR	Briggsdale, Colorado	https://doi.org/10.15138/39HR-9N34	McKain, K.; Sweeney, C.
CMA	Cape May, New Jersey	https://doi.org/10.15138/39HR-9N34	McKain, K.; Sweeney, C.
CON	CONTRAIL (Comprehensive Observation Network for TRace gases by AIrLiner)	http://dx.doi.org/10.17595/20180208.001	Toshinobu Machida (NIES) AND Hidekazu Matsueda (MRI) AND Yosuke Niwa (NIES) AND Motoki Sasakawa (NIES)
CRV	Carbon in Arctic Reservoirs Vulnerability Experiment (CARVE)	https://doi.org/10.3334/ORNLDAAC/1404	Sweeney, C.; Karion, A.; Miller, J.B.; Miller, C.E.
DND	Dahlen, North Dakota	https://doi.org/10.15138/39HR-9N34	McKain, K.; Sweeney, C.
ECO	East Coast Outflow	https://doi.org/10.1029/2019GL082635	Sweeney, C.; McKain, K.
ESP	Estevan Point, British Columbia	https://doi.org/10.15138/39HR-9N34	McKain, K.; Sweeney, C.
ETL	East Trout Lake, Saskatchewan	https://doi.org/10.15138/39HR-9N34	McKain, K.; Sweeney, C.
FAM	FAAM Aircraft, UK		Xin Lan
FWI	Fairchild, Wisconsin	https://doi.org/10.15138/39HR-9N34	Sweeney, C.;
GSFC	NASA Goddard Space Flight Center Aircraft Campaign		Kawa, S.R.; Abshire, J.B.; Riris, H.
HAA	Molokai Island, Hawaii	https://doi.org/10.15138/39HR-9N34	Sweeney, C.;
HFM	Harvard University Aircraft Campaign	doi:10.1002/2014JD022591	Sweeney, C.;
HIL	Homer, Illinois	https://doi.org/10.15138/39HR-9N34	McKain, K.; Sweeney, C.

HIP	HIPPO (HIAPER Pole-to-Pole Observations)	https://doi.org/10.3334/CDIAC/HIPPO_010	Wofsy, S.C.; Stephens, B.B.; Elkins, J.W.; Hintsa, E.J.; Moore, F.
IAGOS-CARIBIC	In-service Aircraft for a Global Observing System	https://doi.org/10.5281/zenodo.10495597	Obersteiner, F.; Boenisch., H; Gehrlein, T.; Zahn, A.; Gerbig, C.; Schuck, T.
IAGOS-CORE	In-service Aircraft for a Global Observing System		Christoph Gerbig (Max-Planck-Institut für Biogeochemie, Jena)
SONGNEX2015	Shale Oil and Natural Gas Nexus 2015 (air campaign)		Thomas Ryerson (NOAA) AND Jeff Peischl (NOAA) AND Ken Aikin (NOAA)
INX	INFLUX (Indianapolis Flux Experiment)	doi:10.1002/2014JD022591	Sweeney, C.; Shepson, P.B.; Turnbull, J.
LEF	Park Falls, Wisconsin	https://doi.org/10.15138/39HR-9N34	McKain, K.; Sweeney, C.
MAN	Manaus, Brazil		Miller, J.B.; Martins, G.A.; de Souza, R.A.F.
NHA	Offshore Portsmouth, New Hampshire (Isles of Shoals)	https://doi.org/10.15138/39HR-9N34	McKain, K.; Sweeney, C.
NSA	North Slope, Alaska	doi:10.1002/2014JD022591	McKain, K.; Sweeney, C.; Biraud, S.C.
OIL	Oglesby, Illinois	https://doi.org/10.15138/39HR-9N34	Sweeney, C.;
ORC	ORCAS (O2/N2 Ratio and CO2 Airborne Southern Ocean Study)	https://doi.org/10.5065/D6SB445X	Stephens, B.B, Sweeney, C., McKain, K., Kort, E.
PFA	Poker Flat, Alaska	https://doi.org/10.15138/39HR-9N34	McKain, K.; Sweeney, C.
RBA-B	Rio Branco	https://doi.org/10.1594/PANGAEA.949643	Gatti, L.V.; Gloor, E.; Miller, J.B.; Peters, W.
RTA	Rarotonga	https://doi.org/10.15138/39HR-9N34	McKain, K.; Sweeney, C.
TOM	Atmospheric Tomography Mission (ATom)	doi: 10.5067/Aircraft/ATom/TraceGas_Aerosol_Global_Distribution	Kathryn McKain (NOAA) AND Colm Sweeney (NOAA) AND Steven C. Wofsy (HU) AND Bruce Daube (HU) AND Roisin Commane (HU)
KORUS-AQ	LARC - NASA Langley Research Center Aircraft Campaign		Gao Chen (NASA LaRC) AND Joshua P. DiGangi (NASA-LaRC) AND Michael Shook (NASA LaRC)
SAN	Santarem, Brazil	https://doi.org/10.1594/PANGAEA.949643	Gatti, L.V.; Gloor, E.; Miller, J.B.; Peters, W.
SCA	Charleston, South Carolina	https://doi.org/10.15138/39HR-9N34	Sweeney, C.; McKain, K.
SGP	Southern Great Plains, Oklahoma	https://doi.org/10.15138/39HR-9N34	Sweeney, C.; McKain, K.; Biraud, S.
TAB	Tabatinga	https://doi.org/10.1594/PANGAEA.949643	Gatti, L.V.; Gloor, E.; Miller, J.B.
TEF	Tefe	https://doi.org/10.1594/PANGAEA.949643	Gatti, L.V.; Gloor, E.; Miller, J.B.; Peters, W.
TGC	Offshore Corpus Christi, Texas	https://doi.org/10.15138/39HR-9N34	McKain, K.; Sweeney, C.
THD	Trinidad Head, California	https://doi.org/10.15138/39HR-9N34	McKain, K.; Sweeney, C.
UGD	Kajjansi Airfield, Kampala, Uganda	https://doi.org/10.15138/515F-N008	McKain, K; Sweeney, C
ULB	Ulaanbaatar, Mongolia	https://doi.org/10.15138/39HR-9N34	Sweeney, C.;
WBI	West Branch, Iowa	https://doi.org/10.15138/39HR-9N34	McKain, K.; Sweeney, C.

(a) Schuldt et al. 2024. Multi-laboratory compilation of atmospheric carbon dioxide data for the period 1957-2023; obspack_co2_1_test_GLOBALVIEWplus_v10.1_2024-11-13; NOAA Earth System Research Laboratory, Global Monitoring Laboratory. http://doi.org/10.25925/20241101

(b) Schuldt et al. 2025. Multi-laboratory compilation of atmospheric carbon dioxide data for the period 2024; obspack_co2_1_NRT_v10.1_2025-02-07; NOAA Earth System Research Laboratory, Global Monitoring Laboratory. http://doi.org/10.25925/20250101.

1123

1124
1125

Table S10. Main methodological changes in the global carbon budget since first publication. Methodological changes introduced in one year are kept for the following years unless noted. Empty cells mean there were no methodological changes introduced that year.

Publication year	Fossil fuel emissions			LUC emissions	Reservoirs			Uncertainty & other changes
	Global	Country (territorial)	Country (consumption)		Atmosphere	Ocean	Land	
2006 (a)		Split in regions						
2007 (b)				ELUC based on FAO-FRA 2005; constant ELUC for 2006	1959-1979 data from Mauna Loa; data after 1980 from global average	Based on one ocean model tuned to reproduced observed 1990s sink		±1σ provided for all components
2008 (c)				Constant ELUC for 2007				
2009 (d)		Split between Annex B and non-Annex B	Results from an independent study discussed	Fire-based emission anomalies used for 2006-2008		Based on four ocean models normalised to observations with constant delta	First use of five DGVMs to compare with budget residual	
2010 (e)	Projection for current year based on GDP	Emissions for top emitters		ELUC updated with FAO-FRA 2010				
2011 (f)			Split between Annex B and non-Annex B					

2012 (g)		129 countries from 1959	129 countries and regions from 1990-2010 based on GTAP8.0	ELUC for 1997-2011 includes interannual anomalies from fire-based emissions	All years from global average	Based on 5 ocean models normalised to observations with ratio	Ten DGVMs available for SLAND; First use of four models to compare with ELUC	
2013 (h)		250 countriesb	134 countries and regions 1990-2011 based on GTAP8.1, with detailed estimates for years 1997, 2001, 2004, and 2007	ELUC for 2012 estimated from 2001-2010 average		Based on six models compared with two data-products to year 2011	Coordinated DGVM experiments for SLAND and ELUC	Confidence levels; cumulative emissions; budget from 1750
2014 (i)	Three years of BP data	Three years of BP data	Extended to 2012 with updated GDP data	ELUC for 1997-2013 includes interannual anomalies from fire-based emissions		Based on seven models	Based on ten models	Inclusion of breakdown of the sinks in three latitude bands and comparison with three atmospheric inversions
2015 (j)	Projection for current year based Jan-Aug data	National emissions from UNFCCC extended to 2014 also provided	Detailed estimates introduced for 2011 based on GTAP9			Based on eight models	Based on ten models with assessment of minimum realism	The decadal uncertainty for the DGVM ensemble mean now uses ±1σ of the decadal spread across models

2016 (k)	Two years of BP data	Added three small countries; China's emissions from 1990 from BP data (this release only)		Preliminary ELUC using FRA-2015 shown for comparison; use of five DGVMs		Based on seven models	Based on fourteen models	Discussion of projection for full budget for current year
2017 (l)	Projection includes India-specific data			Average of two bookkeeping models; use of 12 DGVMs		Based on eight models that match the observed sink for the 1990s; no longer normalised	Based on 15 models that meet observation-based criteria (see Sect. 2.5)	Land multi-model average now used in main carbon budget, with the carbon imbalance presented separately; new table of key uncertainties
2018 (m)	Revision in cement emissions; Projection includes EU-specific data	Aggregation of overseas territories into governing nations for total of 213 countries a		Average of two bookkeeping models; use of 16 DGVMs	Use of four atmospheric inversions	Based on seven models	Based on 16 models; revised atmospheric forcing from CRUNCEP to CRUJRA	Introduction of metrics for evaluation of individual models using observations
2019 (n)	Global emissions calculated as sum of all countries plus bunkers, rather than taken directly from CDIAC.			Average of two bookkeeping models; use of 15 DGVMs	Use of three atmospheric inversions	Based on nine models	Based on 16 models	

2020 (o)	Cement carbonation now included in the EFOS estimate, reducing EFOS by about 0.2GtC yr-1 for the last decade	India's emissions from Andrew (2020: India); Corrections to Netherland Antilles and Aruba and Soviet emissions before 1950 as per Andrew (2020: CO2); China's coal emissions in 2019 derived from official statistics, emissions now shown for EU27 instead of EU28. Projection for 2020 based on assessment of four approaches.		Average of three bookkeeping models; use of 17 DGVMs. Estimate of gross land use sources and sinks provided	Use of six atmospheric inversions	Based on nine models. River flux revised and partitioned NH, Tropics, SH	Based on 17 models	
2021 (p)	Projections are no longer an assessment of four approaches.	Official data included for a number of additional countries, new estimates for South Korea, added emissions from lime production in China.		ELUC estimate compared to the estimates adopted in national GHG inventories		Average of means of eight models and means of seven data-products. Current year prediction of SOCEAN using a feed-forward neural network method	Current year prediction of SLAND using a feed-forward neural network method	

2022 (q)				ELUC provided at country level. Revised components decomposition of ELUC fluxes. Revision of LUC maps for Brazil. New datasets for peat drainage.	Use of nine atmospheric inversions	Average of means of ten models and means of seven data-products	Based on 16 models. Revision of LUC maps for Brazil.	
2023 (r)				Refined components decomposition of ELUC. Revision of LUC maps for Indonesia. Use of updated peat drainage estimates.	Use of 14 atmospheric inversions. Additional use of 4 Earth System Models to estimate current year CO2	Additional use of 4 Earth System Models and atmospheric oxygen method to assess SOCEAN. Regional distribution of river flux adjustment revised.	Based on 20 models. Additional use of 4 Earth System Models and atmospheric oxygen method to assess the net atmosphere-land flux.	Inclusion of an estimate of Carbon Dioxide Removal

2024 (s)	Inclusion of 2024 projections from Carbon Monitor	Inclusion of 2024 projections from Carbon Monitor for China, USA, EU27, India, and Rest of the World		Fourth bookkeeping estimate (LUCE). Update in land-use data (HYDE3.4) including revision of LUC maps for China. Updated definition of forest (re-)growth fluxes (consistent with 2nd State of CDR Report).	Use of 14 atmospheric inversions models	Use of 10 GOBMs, 8 fCO2-products. Added evaluation for fCO2-products.	Use of 20 DGVMs	

e Friedlingstein et al. (2010)

f Peters et al. (2012a)

g Le Quéré et al. (2013), Peters et al. (2013)

h Le Quéré et al. (2014)

i Le Quéré et al. (2015a)

j Le Quéré et al. (2015b)

k Le Quéré et al. (2016)

l Le Quéré et al. (2018a)

m Le Quéré et al. (2018b)

n Friedlingstein et al. (2019)

o Friedlingstein et al. (2020

p Friedlingstein et al. (2022a)

q Friedlingstein et al. (2022b)

r Friedlingstein et al. (2023)

s Friedlingstein et al. (2025a)

1126

1127

Table S11: Translation of global carbon cycle models' land flux definitions to the definition of the LULUCF net flux used by National GHG Inventory (NGHGI) reports to UNFCCC. Non-intact lands are used here as a proxy for "managed lands" in the country reporting. NGHGIs are gap-filled (see Sec. C.2.3 for details). For comparison, we provide the net land flux on managed land from atmospheric inversions and FAOSTAT estimates. Units are GtC yr-1.

Carbon flux	Source	2005-2014	2015-2024
ELUC	Bookkeeping estimates (see Table 5)	1.70	1.37
SLAND total	DGVMs (see Table 5)	2.50	2.36
SLAND in non-intact forest	DGVMs	1.89	1.89
ELUC minus SLAND in non-intact forest	Bookkeeping ELUC & DGVM SLAND	-0.19	-0.52
LULUCF	NGHGIs	-0.89	-1.05
Net land flux on managed land	Atmospheric inversions	-0.89	-0.68
LULUCF	FAOSTAT	0.00	-0.01

1128

Table S12 - Evaluation of global ocean biogeochemistry models based on comparison with observation-based interior ocean carbon accumulation and process-based evaluation metrics for Atlantic Meridional Overturning Circulation (AMOC), Southern Ocean sea surface salinity and surface ocean Revelle factor (following the RECCAP2 ocean model evaluation chapter, Terhaar et al., 2024) and Southern Ocean stratification index (Bourgeois et al., 2022). See supplementary text C3.3 for details of calculation and observational data sources.

		Global Ocean Biogeochemistry Models									
Metric	**Observations**	ACCESS (CSIRO)	CESM-ETHZ	FESOM 2.1-REcoM	MOM6-Cobalt (Princeton)	MPIOM-HAMOCC6	MRI-ESM2-3	NEMO-PISCES (IPSL)	NEMO-PlankTOM12	NEMO3.6-PISCESv2-gas (CNRM)	NorESM-OC1.2
Interior ocean anthropogenic carbon accumulation in GtC yr^{-1}											
Global (1994-2007, Gruber et al., 2019)	33.8 ± 4.0	35.6	26.9	32.0	33.0	19.9	27.9	32.6	25.4	27.1	33.4
North (1994-2007, Gruber et al., 2019)	5.9	6.1	5.6	5.8	3.8	3.6	5.7	6.4	4.2	5.8	6.8
Tropics (1994-2007, Gruber et al., 2019)	17.5	15.3	8.7	13.8	14.5	7.2	12.7	15.7	12.5	13.4	13.6
South (1994-2007, Gruber et al., 2019)	10.4	14.2	12.6	12.4	14.6	9.1	9.6	11.0	8.6	8.8	13.0
Global (1994-2004, Müller et al., 2023)	29.3 ± 2.5	26.0	19.2	23.7	24.8	15.3	20.5	24.1	18.5	21.2	24.7
Global (2004-2014, Müller et al., 2023)	27.3 ± 2.5	30.8	23.3	27.9	29.1	18.5	24.0	28.1	22.4	23.8	28.4
Atlantic Meridional Overturning Circulation at 26°N, 2005-2023 in Sv (Moat et al., 2025)	*16.9 ± 1.2*	6.8	13.8	10.2	4.8	14.9	13.2	13.2	17.8	13.0	22.8
Southern Ocean sea surface salinity 2005-2024 in psu (Good et al., 2013)											
subpolar seasonally stratified biome (SPSS)	33.944	34.194	33.826	34.256	34.859	33.927	34.059	34.192	33.873	33.823	34.116
subpolar seasonally stratified and subtropical seasonally stratified biomes (SPSS+STSS)	34.309	34.571	34.266	34.557	34.859	34.280	34.392	34.544	34.386	34.149	34.541
Southern Ocean stratification index 2005-2024, in kg m-3 (Bourgeois et al., 2022, Good et al., 2013)	5.88	5.44	6.16	5.67	5.73	5.96	5.97	5.53	5.06	6.18	5.76
Surface ocean Revelle factor											
1997-2007, unitless (GLODAPv2.2016, Lauvset et al., 2016)	10.49	10.59	10.02	10.64	10.64	10.70	10.56	10.68	10.46	10.74	10.54
2005-2022, unitless (OceanSODA_v2023, updated from Gregor and Gruber, 2021)	10.91	10.91	10.31	10.95	10.94	11.02	10.89	10.98	10.77	11.05	10.87

1129

1130

Table S13 fCO2 data sets suspended from SOCATv2025 (Bakker et al., 2016, 2025) included in earlier SOCAT versions.

Expocode	Platform Name	Regions	Principal Investigators	Platform Type	Included in SOCAT versions	Suspended from SOCAT version	Reason for suspension or exclusion
11SS20201023	Simon Stevin	coastal	Gkritzalis, T.	Research vessel	v2022-v2024	v2025	Warming of upto 18°C
11SS20211101	Simon Stevin	coastal	Gkritzalis, T.	Research vessel	v2022-v2024	v2025	Warming of upto 16°C
18DL20100701	CCGS Amundsen	Arctic Ocean, coastal	Papakyriakou, T.	Research vessel	v2019-v2024	v2025	Temperature sensors swapped
18DL20110718	CCGS Amundsen	Arctic Ocean, coastal	Papakyriakou, T.	Research vessel	v2019-v2024	v2025	Temperature sensors swapped
18DL20130725	CCGS Amundsen	Arctic Ocean	Papakyriakou, T., Else, B., Burgers, T., Thomas, H., Mucci, A.	Research vessel	v2018(v6)-v2024	v2025	Temperature sensors swapped. Overlap with 18DL20130726
18DL20130726	CCGS Amundsen	Arctic Ocean	Papakyriakou, T.	Research vessel	v2019-v2024	v2025	Temperature sensors swapped. Overlap with 18DL20130725
18DL20140707	CCGS Amundsen	Arctic Ocean, coastal	Papakyriakou, T.	Research vessel	v2019-v2024	v2025	Temperature sensors swapped
18DL20140708	CCGS Amundsen	Arctic Ocean	Papakyriakou, T., Else, B., Burgers, T., Thomas, H., Mucci, A.	Research vessel	v2018(v6)-v2024	v2025	Data set updated as 18DL20140707
18DL20150417	CCGS Amundsen	Arctic Ocean, coastal	Papakyriakou, T.	Research vessel	v2019-v2024	v2025	Temperature sensors swapped
18DL20160802	CCGS Amundsen	Arctic Ocean	Papakyriakou, T.	Research vessel	v2021-v2024	v2025	Temperature sensors swapped
29SG20210528	RV Sarmiento de Gambao	North Atlantic, coastal	Velo, A.	Research vessel	v2023-v2024	v2025	awaits update
29SG20210630	RV Sarmiento de Gambao	North Atlantic, coastal	Velo, A.	Research vessel	v2023-v2024	v2025	awaits update
29SG20211115	RV Sarmiento de Gambao	North Atlantic, Tropical Atlantic, Southern Ocean, coastal	Padin, X. A.	Research vessel	v2023-v2024	v2025	awaits update
29SG20220911	RV Sarmiento de Gambao	North Atlantic, coastal	Fontela, M.	Research vessel	v2023-v2024	v2025	awaits update
91AA20190718	SA Agulhas II	Southern Ocean	Hamnca, S., Monteiro, P. M. S.	Research vessel	v2024	v2025	near-zero warming, despite variable seawater temperature and fugacity of CO2, metadata

							incomplete
91AA20191013	SA Agulhas II	Southern Ocean	Hamnca, S., Monteiro, P. M. S.	Research vessel	v2024	v2025	temperature sensors offset by 2 hours, metadata incomplete
91AA20191217	SA Agulhas II	Southern Ocean	Hamnca, S., Monteiro, P. M. S.	Research vessel	v2024	v2025	temperature sensors offset by 2 hours, metadata incomplete
91AA20220711	SA Agulhas II	Southern Ocean	Hamnca, S.	Research vessel	v2024	v2025	temperature sensors offset by 2 hours, fCO2 exceeds highest standard gas, metadata incomplete
91AA20221219	SA Agulhas II	Southern Ocean	Hamnca, S., Tsanwani, M., Monteiro, P. M. S.	Research vessel	v2024	v2025	unacceptable data, metadata incomplete

1131

Supplementary figures

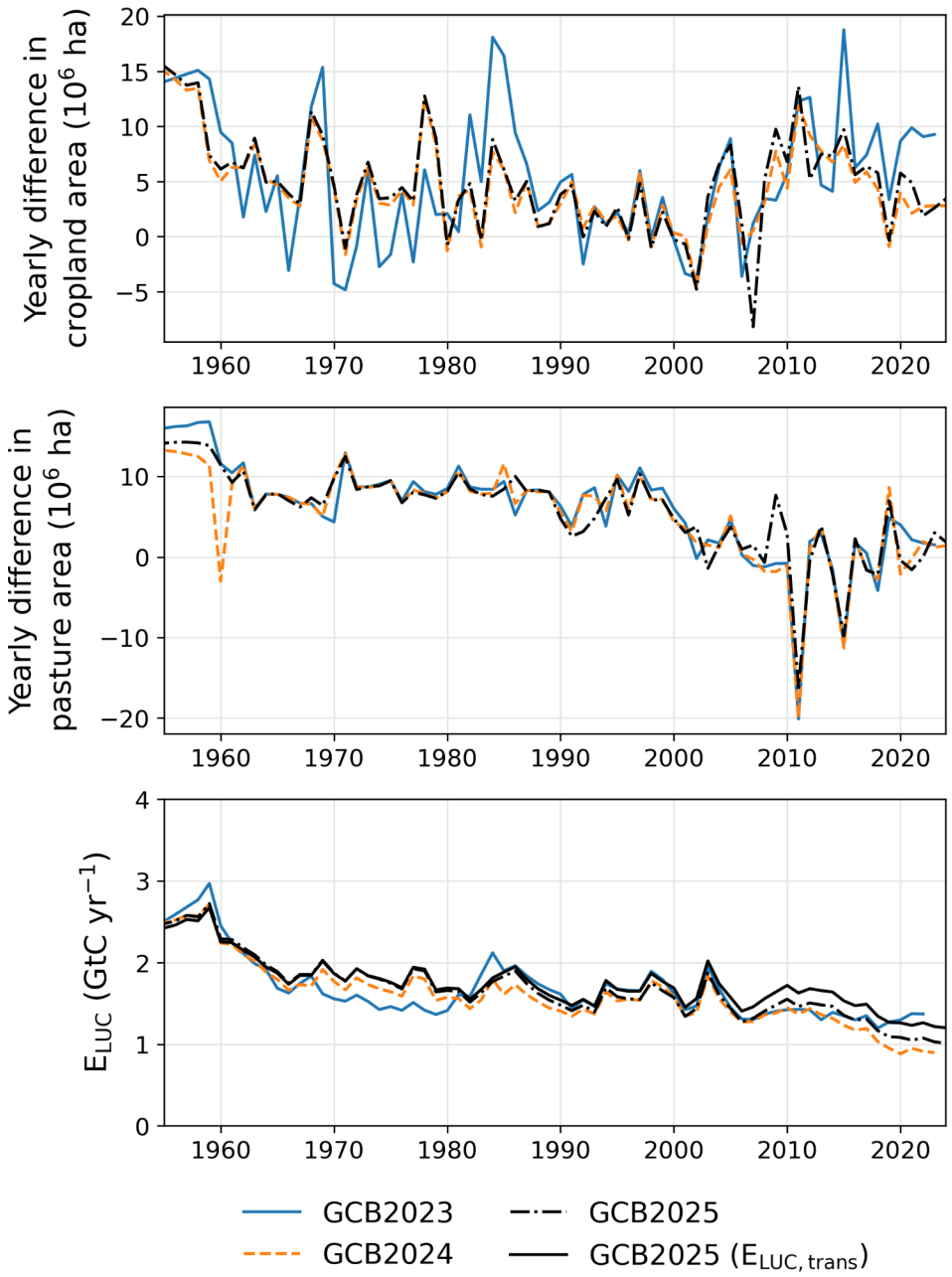

Figure S1. Differences in the HYDE/LUH2 land-use forcing used for the global carbon budgets GCB2023 (Friedlingstein et al., 2023), GCB2024 (Friedlingstein et al., 2025a), and GCB2025 (this paper). Shown are year-to-year changes in cropland area (top panel) and pasture area (middle panel). To illustrate the relevance of the update in the land-use forcing for the recent trends in E_{LUC}, the bottom panel shows the land-use emission estimate from the bookkeeping model BLUE (original model output, i.e., excluding emissions from peat fire and peat drainage). The inclusion of transient carbon densities in GCB2025 is also shown on the bottom panel.

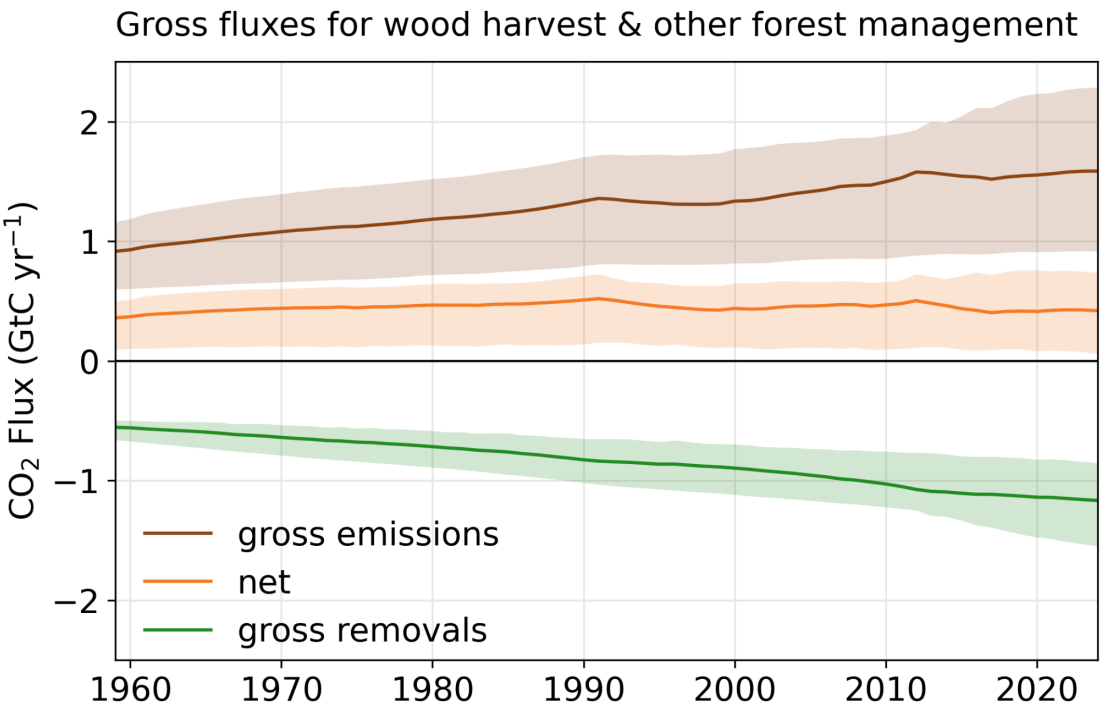

Figure S2. Split of net CO_2 fluxes from wood harvest and other forest management into gross emissions and gross removals. Solid lines denote the average of the three bookkeeping models and shaded areas the full range (min-max) of the bookkeeping model estimates. Gross wood harvest emissions amount to 1.6 [0.9, 2.2] GtC yr^{-1} in 2015-2024 resulting from the decomposition of slash and the decay of wood products. Gross removals amount to −1.1 [−1.5, −0.8] GtC yr^{-1} in 2015-2024 resulting from regrowth after wood harvesting.

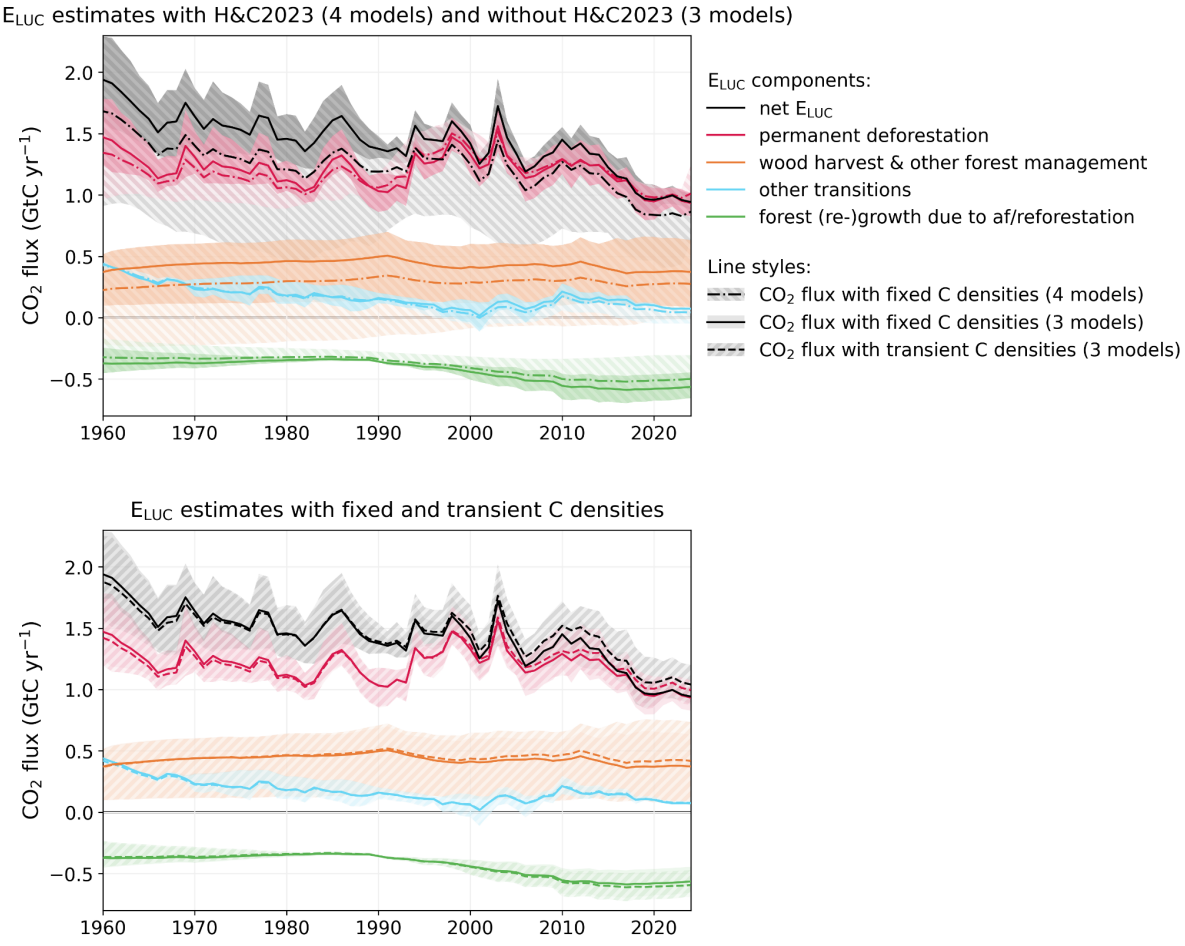

Figure S3. Effects of methodological changes in GCB2025 on land-use change emissions (E_{LUC}) estimates for net E_{LUC} and sub-components. Top: Comparison of E_{LUC} estimates based on three bookkeeping models (BLUE, LUCE, OSCAR) and four bookkeeping models (BLUE, LUCE, H&C2023, OSCAR) using fixed carbon densities. Bottom: Comparison of E_{LUC} estimates with fixed and transient carbon densities using estimates from the three bookkeeping models that are able to estimate E_{LUC} with transient carbon densities (BLUE, LUCE, OSCAR). The GCB2025 E_{LUC} estimates are based on simulations with transient carbon densities from BLUE, LUCE, and OSCAR. Shading represents the mininum-to-maximum range across bookkeeping estimates.

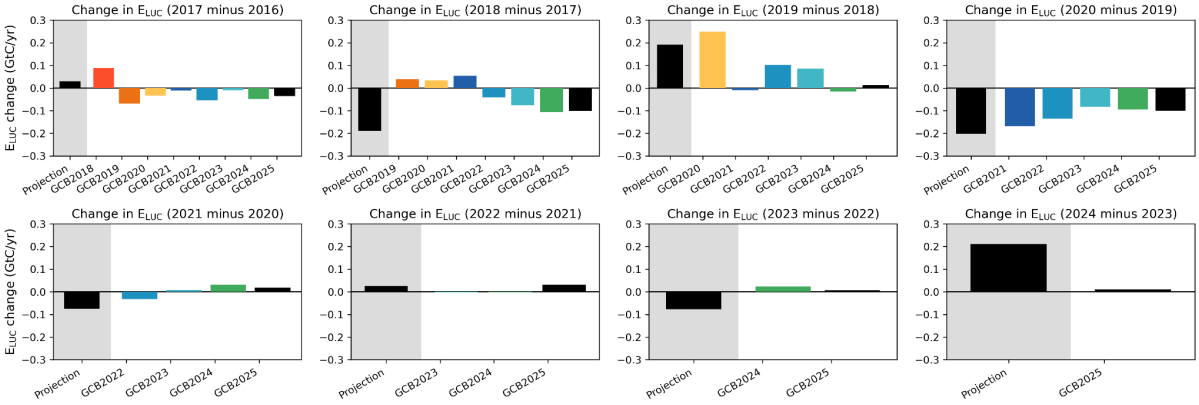

Figure S4. Comparison of initial E_{LUC} projections (E_{LUC} changes relative to the E_{LUC} estimate in the previous year) based on anomalies in peat fires in equatorial Asia and tropical deforestation and degradation fires with updated estimates in later global carbon budgets (GCBs) based on bookkeeping model simulations. Black bars on gray background indicate E_{LUC} projections; colored bars indicate bookkeeping E_{LUC} estimates from later GCB versions (with the GCB2025 bookkeeping E_{LUC} estimate in black).

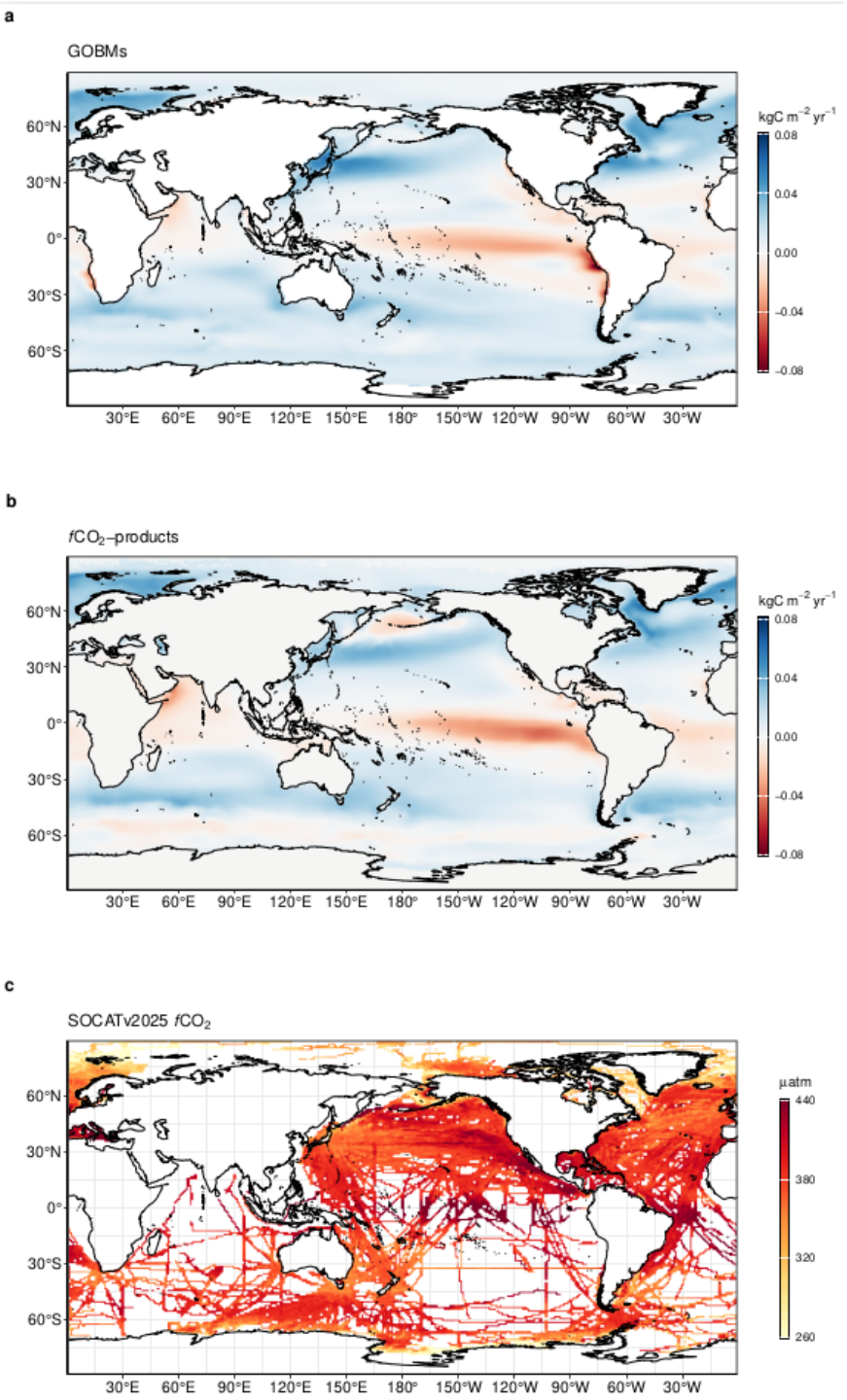

Figure S5. Ensemble mean air-sea CO_2 flux from a) global ocean biogeochemistry models and b) fCO_2 based data products, averaged over 2015-2024 period (kgC m^{-2} yr^{-1}). Positive numbers indicate a flux into the ocean. c) gridded SOCATv2025 fCO_2 measurements, averaged over the 2015-2024 period (µatm). In (a) model simulation A is shown. The fCO_2-products represent the contemporary flux, i.e. including outgassing of riverine carbon, which is estimated to amount to 0.65 GtC yr^{-1} globally.

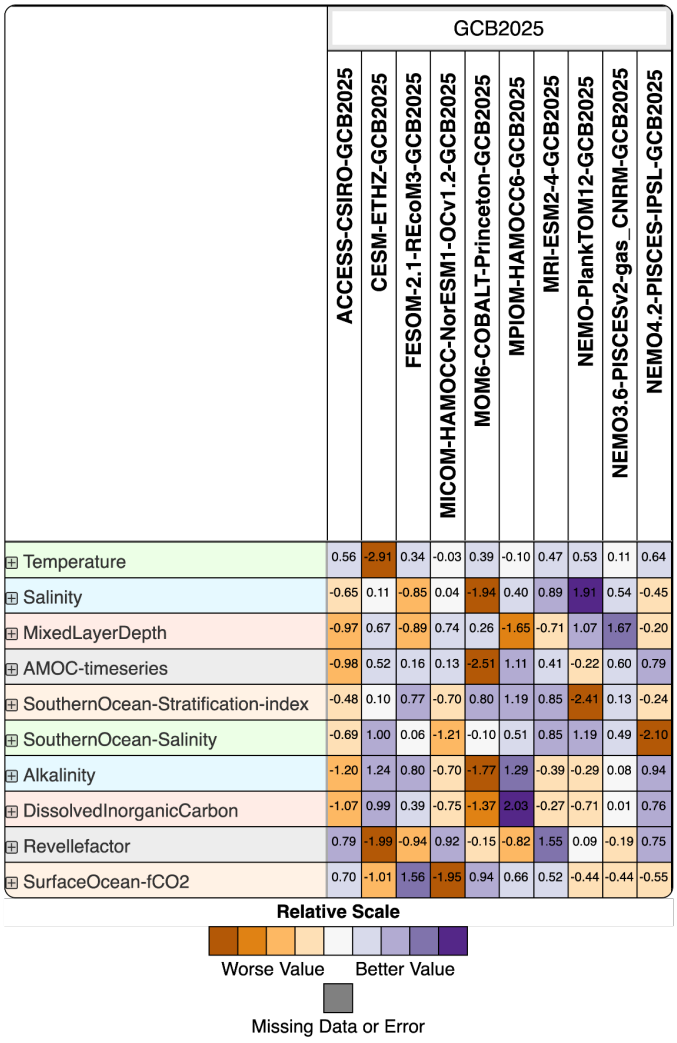

Figure S6. Evaluation of the GOBMs using the IOMB scheme considering physical (sea surface temperature, sea surface salinity, mixed layer depth, Southern Ocean stratification index, Southern Ocean subpolar biome surface salinity, and Atlantic Meridional Overturning Circulation (AMOC)) and biogeochemical variables (surface dissolved inorganic carbon, alkalinity, Revelle factor and CO_2 fugacity (fCO_2)). See section S3.3 for observational data sets and statistical metrics included.

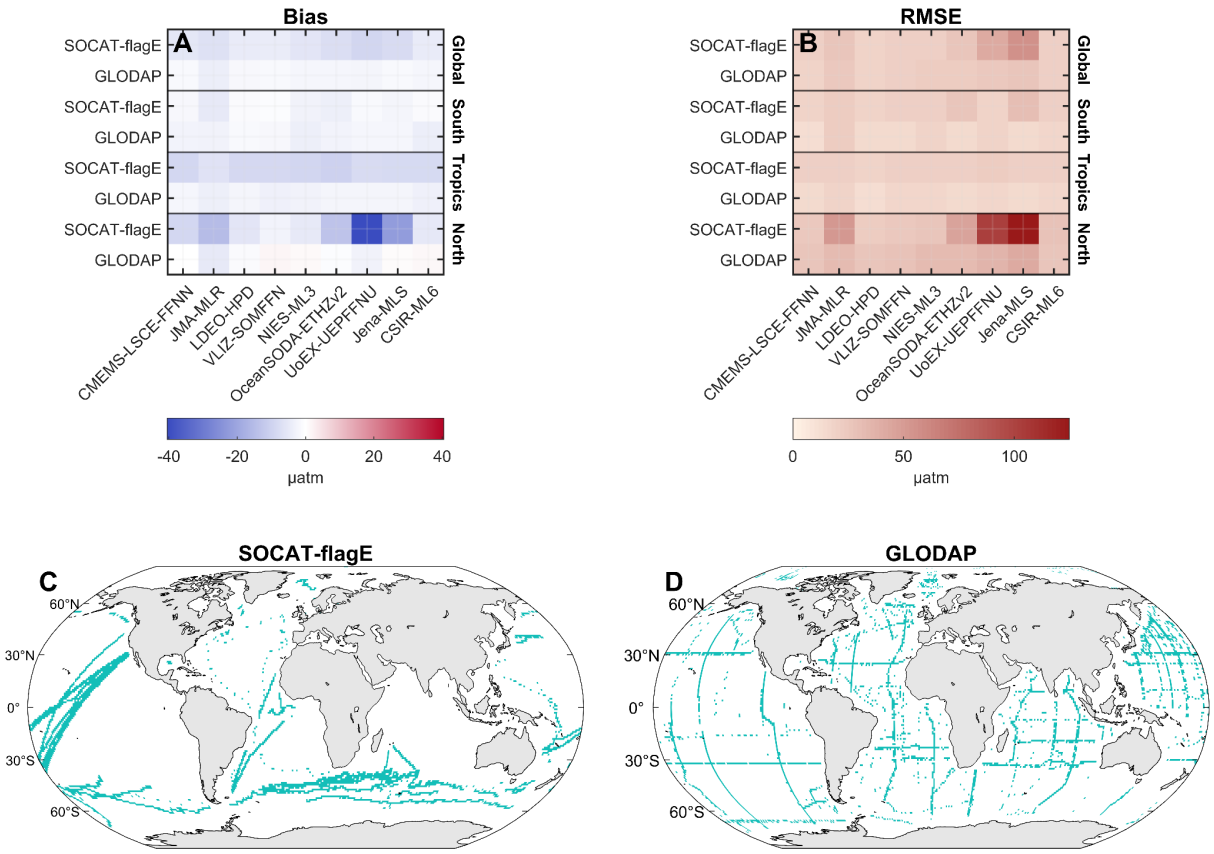

Figure S7: Bias (a) and RMSE (b) between independent observations from the SOCAT flag E and GLODAPv2 datasets with 9 fCO_2-products included in the global carbon budget. Panels C and D show the location of the observations in the global ocean.

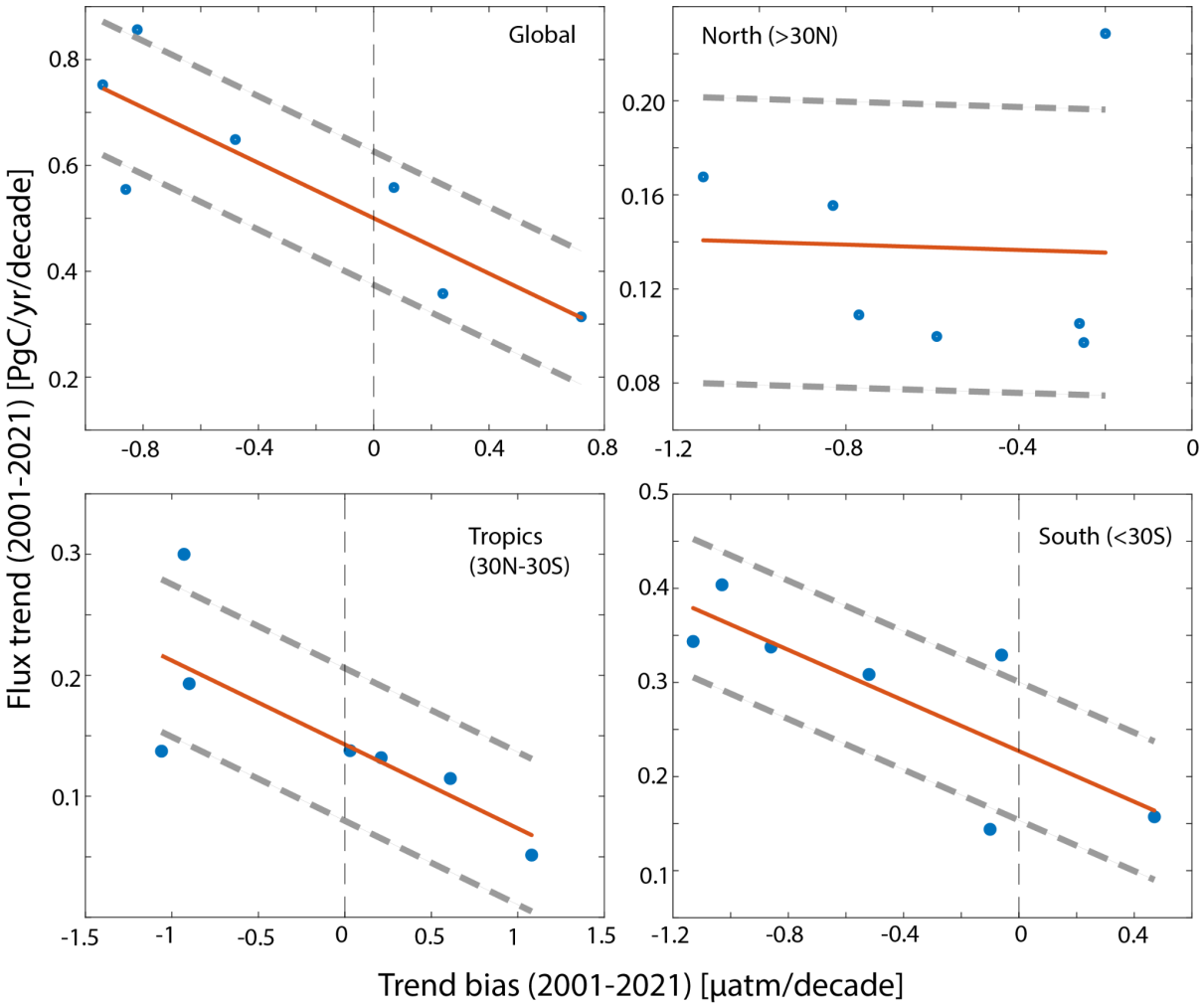

Figure S8. Trend evaluation of six from the eight fCO_2-products used for S_{OCEAN} (blue circles - CSIR-ML6, NIES-ML3, VLIZ-SOMFFN, OceanSODA-ETHZv2, JMA-MLR, Jena-MLS). The x-axis represents the mean fCO_2 trend bias from a model subsampling exercise (following Hauck et al., 2023a) using four of the GCB2023 GOBMs (CESM, FESOM-REcoM, IPSL and MRI-ESM). The y-axis represents the flux trend as submitted by the fCO_2 product to this study. Besides the northern hemisphere, where all of the six fCO_2-products overestimate the subsampled model trend, there is a clear relationship between the trend reconstruction bias and the flux trend (red line with grey dashed lines representing the 1 sigma uncertainty interval), indicating that flux trends are sensitive to the fCO_2-products ability to reconstruct biases.

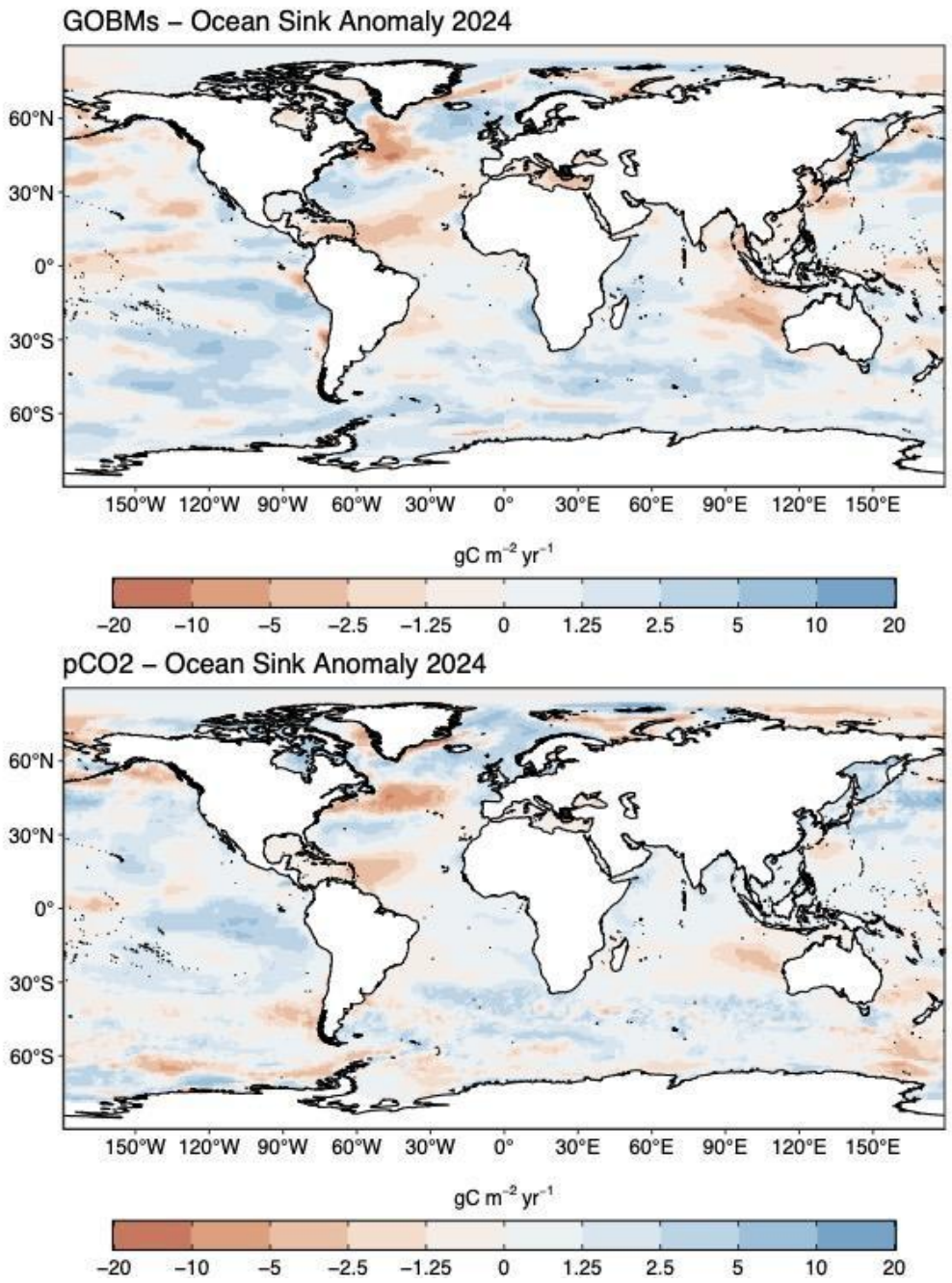

Figure S9 Anomalies in the ocean sink for 2024, as in Figure 11c, but here separated into the anomalies derived from (top) GOBMs and (bottom) fCO_2-products. Maps show the 2024 fluxes relative to 2015-2024 decadal mean. Units are gC m^{-2} yr^{-1}.

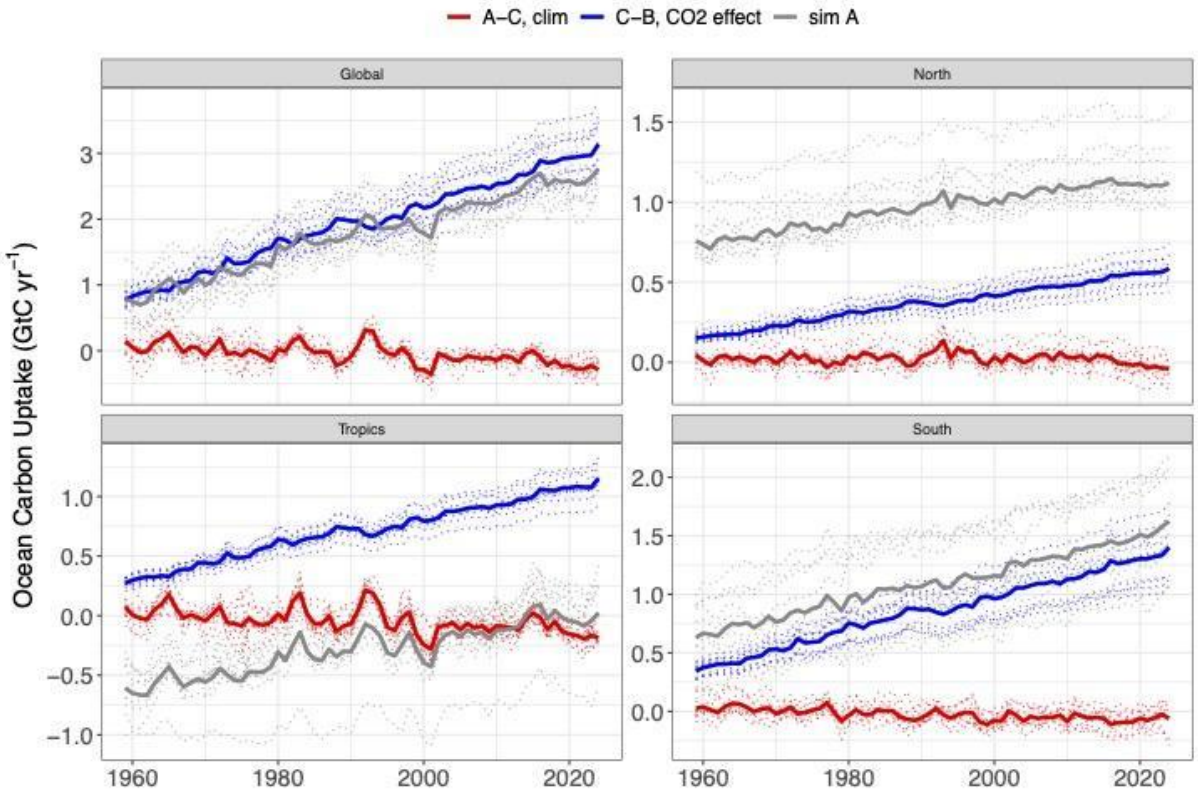

Figure S10 Time-series of CO_2 and climate effects on the S_{OCEAN} in the global ocean, and three latitudinal bands (north, tropics, south) as indicated in the panels. Dotted lines show individual global ocean biogeochemistry models and solid lines indicate the ensemble mean. The grey line shows the contemporary flux (simulation A) without adjustments, which represents the sum of natural fluxes, CO_2 and climate effects, bias and drift. The CO_2 and climate effects are calculated from simulation C minus B and A minus C, respectively. See section S3.2 on GOBM simulations.

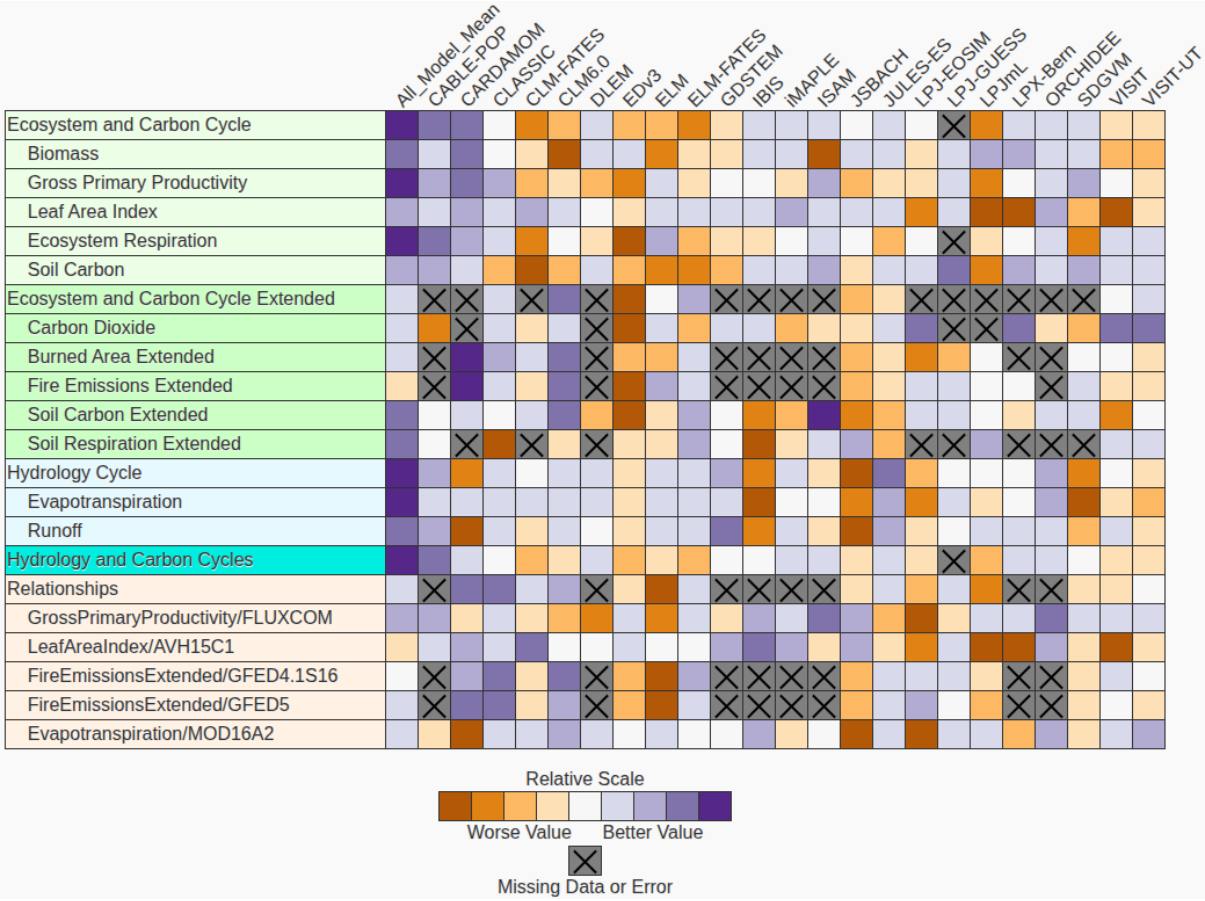

Figure S11. Evaluation of the DGVMs using the International Land Model Benchmarking system (ILAMB; Collier et al., 2018). Skill scores relative to other models. The benchmarking is done with observations for vegetation biomass (Santoro and Cartus, 2021; Saatchi et al., 2011; Thurner et al. 2014; Santoro et al. 2024; Xu et al., 2021), GPP and ecosystem respiration (Reichstein et al., 2007; Lasslop et al., 2010; Knauer et al., 2018; Jung et al., 2017; Tramontana et al., 2016; Alemohammad et al., 2017), leaf area index (Vermote, 2019; Claverie et al., 2016; De Kauwe et al., 2011; Myneni et al., 1997), soil carbon (Hugelius et al., 2013; Fischer et al., 2008), soil respiration (Tang et al., 2019, 2020; Raich et al., 2002; Hashimoto et al., 2015; Hashimoto et al., 2023), carbon dioxide (Dlugokencky et al., 2013; Liptak et al., 2017), burned area and fire emissions (Chen et al., 2023), evapotranspiration (De Kauwe et al., 2011; Martens et al., 2017; Miralles et al., 2011; Mu et al., 2011), and runoff (Dai and Trenberth, 2002; Hobeichi et al., 2019; Hobeichi et al., 2020). Metrics include relationships between carbon cycle variables, precipitation (Adler et al., 2003) and temperature (Harris et al., 2014). For each model–observation comparison a series of error metrics are calculated, scores are then calculated as an exponential function of each error metric, and finally for each variable the multiple scores from different metrics and observational datasets are combined to give the overall variable scores. Overall variable scores increase from 0 to 1 with improvements in model performance. The All_Model_Mean does not include CARDAMOM. The set of error metrics vary with dataset and can include metrics based on the period mean, bias, root mean squared error, spatial distribution, interannual variability, and seasonal cycle. The relative skill score shown is a Z score, which indicates in units of standard deviation the model scores relative to the mean score for a given variable. The overall score is given in the row 'Hydrology and Carbon Cycles', which represents a weighted average of the 'Hydrology Cycle' score and the 'Ecosystem and Carbon Cycle' score. Grey boxes with x's represent missing model data.

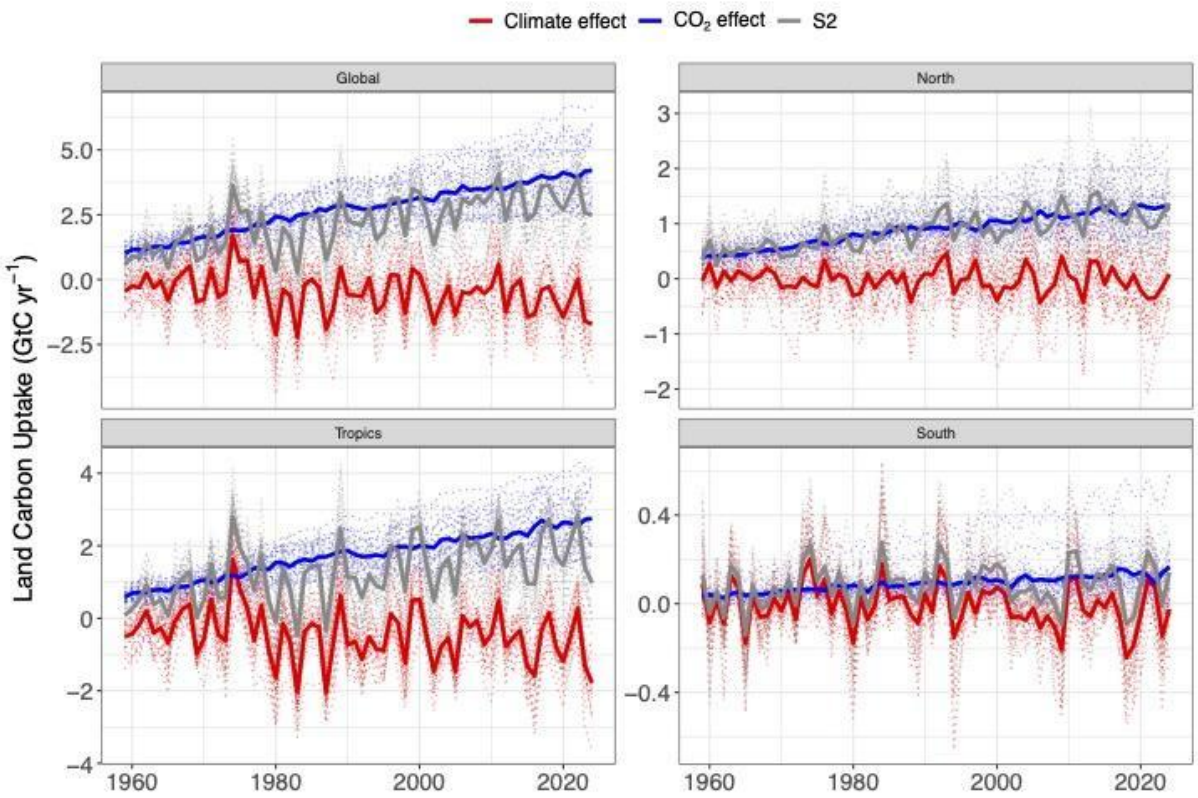

Figure S12. Time-series of CO_2 and climate effects on the land sink for global land, and three latitudinal bands (north, tropics, south) as indicated in the panels. Dotted lines show individual dynamic global vegetation models and solid lines indicate the ensemble mean. The grey line shows the S_{LAND} flux (simulation S2) without RSS adjustment, which represents the sum of natural fluxes, CO_2 and climate effects. The CO_2 and climate effects are calculated from simulations S1 minus S0 and S2 minus S1 plus S0, respectively. See section S4.1 on DGVM simulations.

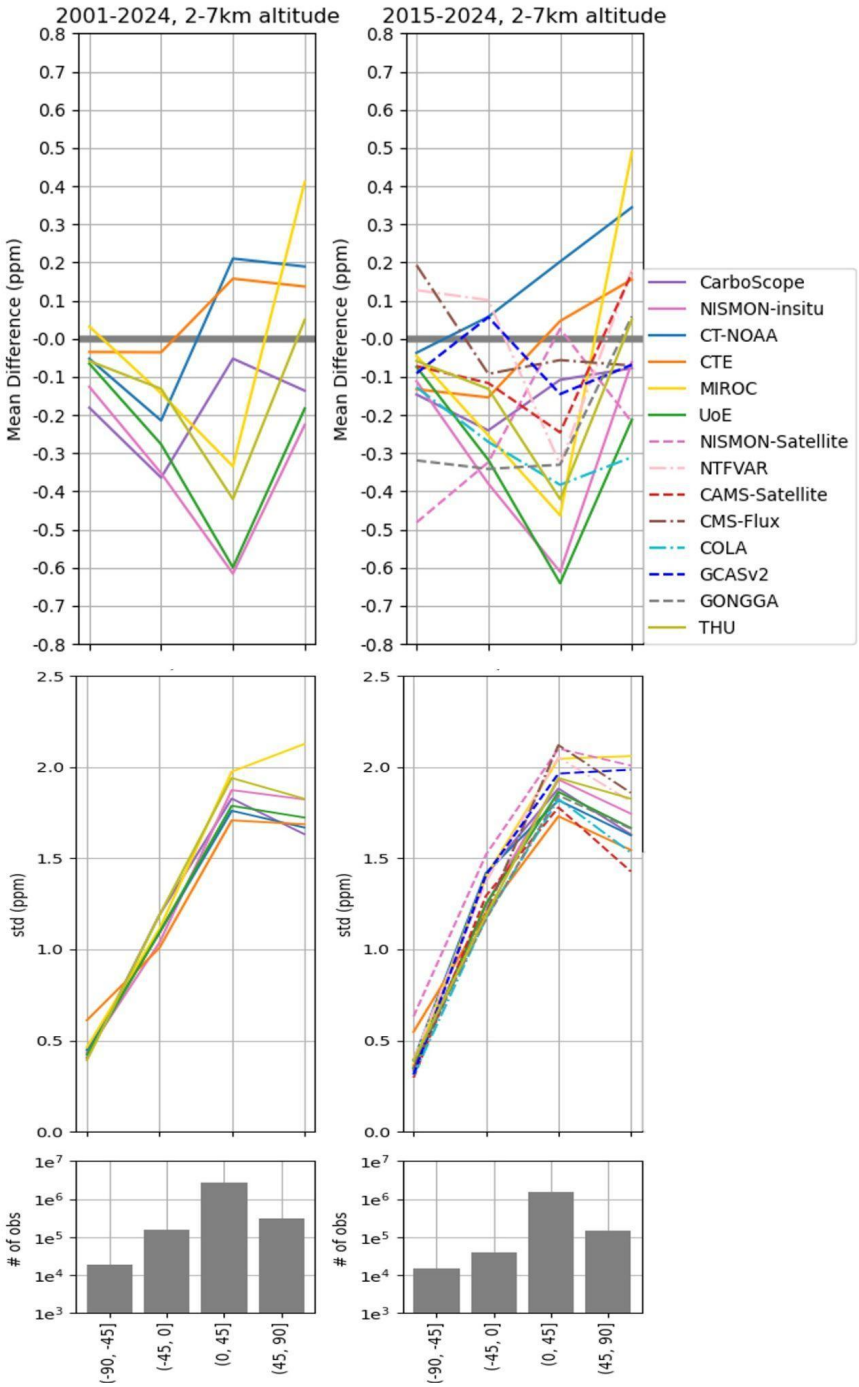

Figure S13. Evaluation of the atmospheric inversion products. The mean of the model minus observations is shown for four latitude bands in three periods: (first panel) 2001-2024, (second panel) 2015-2024. The 14 systems are compared to independent CO_2 observations from aircraft over many places of the world between 2 and 7 km above sea level. Aircraft measurements archived in the Cooperative Global Atmospheric Data Integration Project (Schuldt et al., 2024, Schuldt et al., 2025) from sites, campaigns or programs that have not been assimilated and cover at least 9 months (except for SH programs) between 2001 and 2024, have been used to compute the biases (top row) and their standard deviations (middle row) in four 45° latitude bins. Land and ocean data are used without distinction, and observation density varies strongly with latitude and time as seen on the lower panels.

Figure S14. Fire carbon emissions for the months January-September for each year 2003-2025 from two global fire emissions products. (Top row) Global emissions. (Middle row) Emissions for the northern hemisphere extra tropics (>30° N), tropics (30°N-30°S) and southern extra tropics (>30°S). (Bottom row) Emissions by RECCAP2 region. The Global Fire Assimilation System (GFAS; Di Giuseppe et al., 2018) (left column) and the Global Fire Emissions Database (GFED, version 4.1s; van der Werf et al., 2017) (right column) are among the most widely applied global fire emissions products based on satellite remote sensing of fire. GFED relies on the post-fire detection of burned areas combined with fuel consumption factors. GFAS relies on the detection of thermal energy release during active fires.

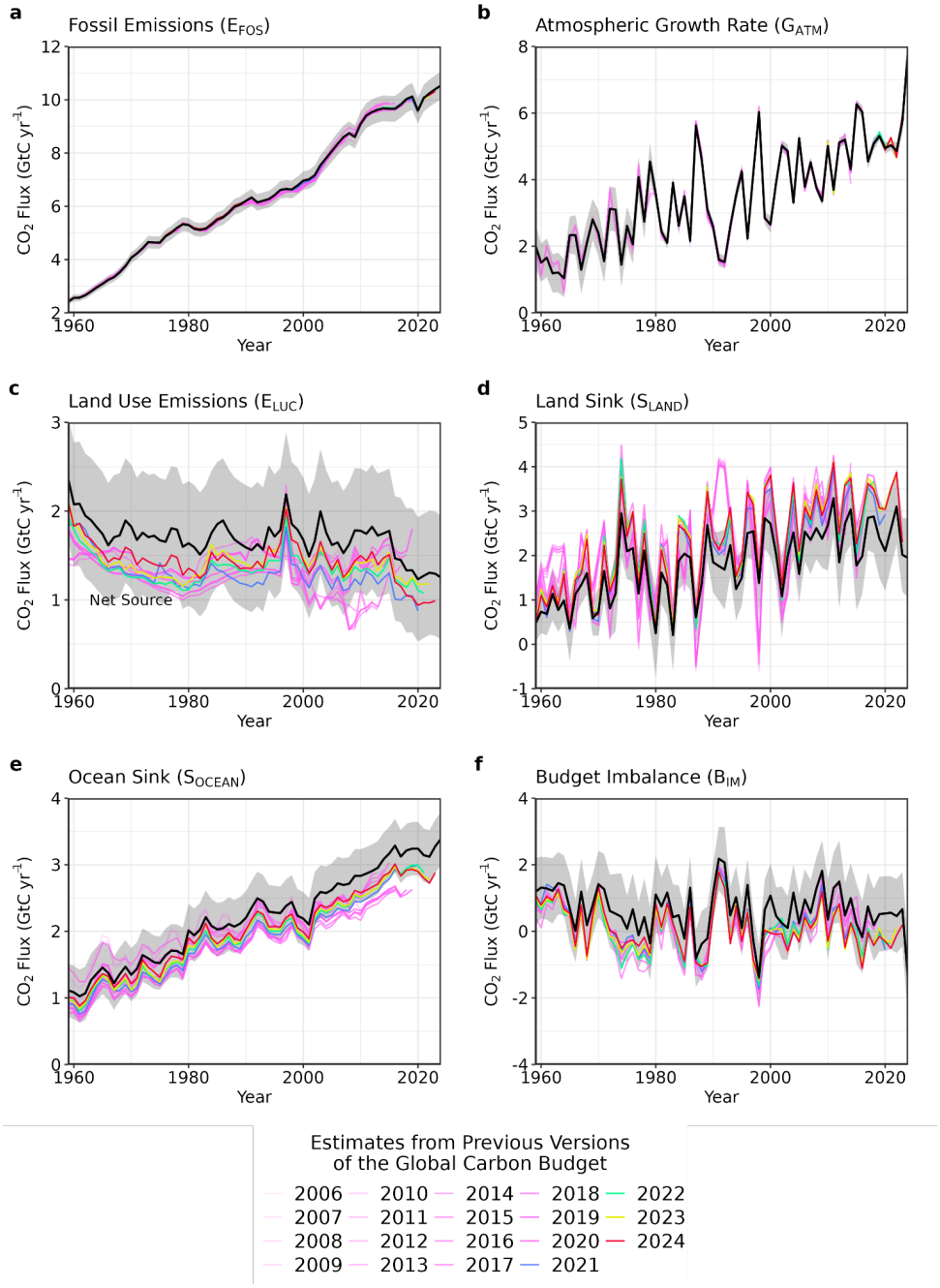

Figure S15. Comparison of the estimates of each component of the global carbon budget in this study (black line) with the estimates released annually by the GCP since 2006. Grey shading shows the uncertainty bounds representing ±1 standard deviation of the current global carbon budget, based on the uncertainty assessments described in Supplement S1 to S4. CO_2 emissions from (a) fossil CO_2 emissions excluding cement carbonation (E_{FOS}), and (b) land-use change (E_{LUC}), as well as their partitioning among (c) the atmosphere (G_{ATM}), (d) the land (S_{LAND}), and (e) the ocean (S_{OCEAN}). See legend for the corresponding years, and Tables 3 and S10 for description of changes in methodology. The budget year corresponds to the year when the budget was first released. All values are in GtC yr^{-1}.

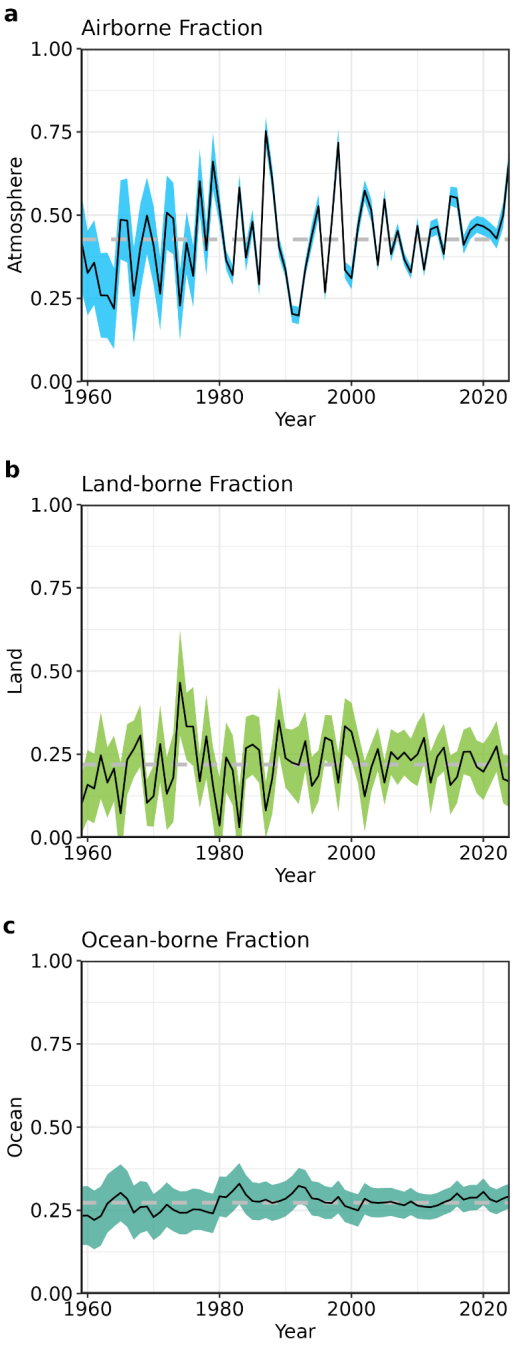

Figure S16. The partitioning of total anthropogenic CO_2 emissions (E_{FOS} + E_{LUC}) across (a) the atmosphere (airborne fraction), (b) land (land-borne fraction), and (c) ocean (ocean-borne fraction). Black lines represent the central estimate, and the coloured shading represents the uncertainty. The grey dashed lines represent the long-term average of the airborne (44%), land-borne (23%) and ocean-borne (27%) fractions during 1959-2024 (with a B_{IM} of 6%).

Figure S17. Kaya decomposition of the main drivers of fossil CO_2 emissions, considering population, GDP per person, Energy per GDP, and CO_2 emissions per energy, for China (top left), USA (top right), EU27 (middle left), India (middle right), Rest of the World (bottom left), and World (bottom right). Black dots are the annual fossil CO_2 emissions growth rate, coloured bars are the contributions from the different drivers to this growth rate. A general trend is that population and GDP growth put upward pressure on emissions (positive values), while energy per GDP and, more recently, CO_2 emissions per energy put downward pressure on emissions (negative values).

Additional references

Adler, R. F., Huffman, G. J., Chang, A., Ferraro, R., Xie, P.-P., Janowiak, J., Rudolf, B., Schneider, U., Curtis, S., Bolvin, D., Gruber, A., Susskind, J., Arkin, P., and Nelkin, E.: The Version-2 Global Precipitation Climatology Project (GPCP) Monthly Precipitation Analysis (1979–Present), J. Hydrometeor, 4, 1147–1167, https://doi.org/10.1175/1525-7541(2003)004<1147:TVGPCP>2.0.CO;2, 2003.

Alemohammad, S. H., Fang, B., Konings, A. G., Aires, F., Green, J. K., Kolassa, J., Miralles, D., Prigent, C., and Gentine, P.: Water, Energy, and Carbon with Artificial Neural Networks (WECANN): a statistically based estimate of global surface turbulent fluxes and gross primary productivity using solar-induced fluorescence, Biogeosciences, 14, 4101–4124, https://doi.org/10.5194/bg-14-4101-2017, 2017.

Alkama, R.: Land Carbon Budget: Intact and Non-Intact Forest NBP from TRENDY-v11 S2 simulations [code], available at: https://github.com/RamAlkama/LandCarbonBudget_IntactAndNonIntactForest, last access: 21 January 2025, 2022.

Amador-Jiménez, M., Millner, N., Palmer, C., Pennington, R. T., and Sileci, L.: The Unintended Impact of Colombia's Covid-19 Lockdown on Forest Fires, Environ Resource Econ, 76, 1081–1105, https://doi.org/10.1007/s10640-020-00501-5, 2020.

Amante, C. and Eakins, B. W.: ETOPO1 Global Relief Model converted to PanMap layer format, PANGAEA [dataset], https://doi.org/10.1594/PANGAEA.769615, 2009.

Andres, R. J., Boden, T. A., Bréon, F.-M., Ciais, P., Davis, S., Erickson, D., Gregg, J. S., Jacobson, A., Marland, G., Miller, J., Oda, T., Olivier, J. G. J., Raupach, M. R., Rayner, P., and Treanton, K.: A synthesis of carbon dioxide emissions from fossil-fuel combustion, Biogeosciences, 9, 1845–1871, https://doi.org/10.5194/bg-9-1845-2012, 2012.

Andres, R. J., Boden, T. A., and Higdon, D.: A new evaluation of the uncertainty associated with CDIAC estimates of fossil fuel carbon dioxide emission, Tellus B: Chemical and Physical Meteorology, 66, 23616, https://doi.org/10.3402/tellusb.v66.23616, 2014.

Andrew, R. M.: Towards near real-time, monthly fossil CO_2 emissions estimates for the European Union with current-year projections, Atmos. Pollut. Res., 12, 12, 101229, https://doi.org/10.1016/j.apr.2021.101229, 2021.

Andrew, R. M. and Peters, G. P.: A multi-region input–output table based on the global trade analysis project database (GTAP-MRIO), Economic Systems Research, 25, 99–121, https://doi.org/10.1080/09535314.2012.761953, 2013.

Arora, V. K., Boer, G. J., Christian, J. R., Curry, C. L., Denman, K. L., Zahariev, K., Flato, G. M., Scinocca, J. F., Merryfield, W. J., and Lee, W. G.: The Effect of Terrestrial Photosynthesis Down Regulation on the Twentieth-Century Carbon Budget Simulated with the CCCma Earth System Model, 22, 6066–6088, https://doi.org/10.1175/2009JCLI3037.1, 2009.

Arora, V. K. and Scinocca, J. F.: Constraining the strength of the terrestrial CO_2 fertilization effect in the Canadian Earth system model version 4.2 (CanESM4.2), Geosci. Model Dev., 9, 2357–2376, https://doi.org/10.5194/gmd-9-2357-2016, 2016.

Bakker, D. C. E., Pfeil, B., Landa, C. S., Metzl, N., O'Brien, K. M., Olsen, A., Smith, K., Cosca, C., Harasawa, S., Jones, S. D., Nakaoka, S., Nojiri, Y., Schuster, U., Steinhoff, T., Sweeney, C., Takahashi, T., Tilbrook, B., Wada, C., Wanninkhof, R., Alin, S. R., Balestrini, C. F., Barbero, L., Bates, N. R., Bianchi, A. A., Bonou, F., Boutin, J., Bozec, Y., Burger, E. F., Cai, W.-J., Castle, R. D., Chen, L., Chierici, M., Currie, K., Evans, W., Featherstone, C., Feely, R. A., Fransson, A., Goyet, C., Greenwood, N., Gregor, L., Hankin, S., Hardman-Mountford, N. J., Harlay, J., Hauck, J., Hoppema, M., Humphreys, M. P., Hunt, C. W., Huss, B., Ibánhez, J. S. P., Johannessen, T., Keeling, R., Kitidis, V., Körtzinger, A., Kozyr, A., Krasakopoulou, E., Kuwata, A., Landschützer, P., Lauvset, S. K., Lefèvre, N., Lo Monaco, C., Manke, A., Mathis, J. T., Merlivat, L., Millero, F. J., Monteiro, P. M. S., Munro, D. R., Murata, A., Newberger, T., Omar, A. M., Ono, T., Paterson, K., Pearce, D., Pierrot, D., Robbins, L. L., Saito, S., Salisbury, J., Schlitzer, R., Schneider, B., Schweitzer, R., Sieger, R., Skjelvan, I., Sullivan, K. F., Sutherland, S. C., Sutton, A. J., Tadokoro, K., Telszewski, M., Tuma, M., van Heuven, S. M. A. C., Vandemark, D., Ward, B., Watson, A. J., and Xu, S.: A multi-decade record of high-quality CO_2 data in version 3 of the Surface Ocean CO_2 Atlas (SOCAT), Earth Syst. Sci. Data, 8, 383–413, https://doi.org/10.5194/essd-8-383-2016, 2016.

Bakker, D. C. E., Alin, S. R., Aramaki, T., Barbero, L., Bates, N. R., Gkritzalis, T., Jones, S. D., Kozyr, A., Lauvset, S. K., Macovei, V., Metzl, N., Munro, D. R., Nakaoka, S.-i., O'Brien, K. M., Olsen, A., Pierrot, D., Steinhoff, T., Sullivan, K. F., Sutton, A. J., Sweeney, C., Wada, C., Wanninkhof, R., Akl, J., Arbilla, L. A., Azetsu-Scott, K., Battisti, R., Beatty, C. M., Becker, M., Benoit-Cattin, A., Berghoff, C. F., Bittig, H. C., Bonin, J. A., Bott, R., Bozzano, R., Burger, E. F., Brunetti, F., Cantoni, C., Castelli, G., Chambers, D. P., Chierici, M., Corbo, A., Cronin, M., Cross, J. N., Currie, K. I., Dentico, C., Emerson, S. R., Enochs, I., Enright, M. P., Enyo, K., Ericson, Y., Evans, W., Fay, A. R., Feely, R. A., Fragiacomo, E., Fransson, A., Gehrung, M., Giani, M., Glockzin, M., Hamnca, S., Holodkov, N., Hoppema, M., Ibánhez, J. S. P., Kadono, K., Kamb, L., Kralj, M., Kristensin, T. O., Laudicella, V. A., Lefèvre, N., Leseurre, C., Lo Monaco, C., Maenner Jones, S. M., Maenza, R. A., McAuliffe, A. M., Mdokwana, B. W., Monacci, N. M., Musielewicz, S., Neill, C., Newberger, T., Nojiri,

Y., Ohman, M. D., Ólafsdóttir, S. R., Olivier, L., Omar, A., Osborne, J., Pensieri, S., Petersen, W., Plueddemann, A. J., Rehder, G., Roden, N. P., Rutgersson, A., Sallée, J.-B., Sanders, R., Sarpe, D., Schirnik, C., Schlitzer, R., Send, U., Skjelvan, I., Sutherland, S., C., T'Jampens, M., Tamsitt, V., Telszewski, M., Theetaert, H., Tilbrook, B., Trull, T., Tsanwani, M., Van de Velde, S., Van Heuven, S. M. A. C., Veccia, M. H., Voynova, Y. G., Weller, R. A., Williams, N. L.: Surface Ocean CO_2 Atlas Database Version 2025 (SOCATv2025) (NCEI Accession 0304549), NOAA National Centers for Environmental Information, Dataset, https://doi.org/10.25921/648f-fv35, 2025a.

Bauer, J. E., Cai, W.-J., Raymond, P. A., Bianchi, T. S., Hopkinson, C. S., and Regnier, P. A. G.: The changing carbon cycle of the coastal ocean, Nature, 504, 61–70, https://doi.org/10.1038/nature12857, 2013.

Beckman, J. and Countryman, A. M.: The Importance of Agriculture in the Economy: Impacts from COVID-19, Am. J. Agr. Econ., 103, 1595–1611, https://doi.org/10.1111/ajae.12212, 2021.

Bellouin, N., Rae, J., Jones, A., Johnson, C., Haywood, J., and Boucher, O.: Aerosol forcing in the Climate Model Intercomparison Project (CMIP5) simulations by HadGEM2-ES and the role of ammonium nitrate, J. Geophys. Res.-Atmos., 116, D20206, https://doi.org/10.1029/2011JD016074, 2011.

Bernardello, R., Sicardi, V., Lapin, V., Ortega, P., Ruprich-Robert, Y., Tourigny, E., and Ferrer, E.: Ocean biogeochemical reconstructions to estimate historical ocean CO2 uptake, Earth Syst. Dynam.,15, 1255–1275, https://doi.org/10.5194/esd-15-1255-2024, 2024.

Bethke, I., Wang, Y., Counillon, F., Keenlyside, N., Kimmritz, M., Fransner, F., ... & Eldevik, T.: NorCPM1 and its contribution to CMIP6 DCPP. Geoscientific Model Development, 14(11), 7073-7116, 2021.

Bilbao, R., S. Wild, P. Ortega et al. (2021). Assessment of a full-field initialised decadal climate prediction system with the CMIP6 version of EC-Earth. Earth Systems Dynamics, doi:10.5194/esd-2020-66. Broecker, W. S.: Ocean chemistry during glacial time, Geochimica et Cosmochimica Acta, 46, 1689–1705, https://doi.org/10.1016/0016-7037(82)90110-7, 1982.

Boucher O., Servonnat, J., Albright,A. L., Aumont, O., Balkanski, Y.,Bastrikov, V., et al.: Presentation and evaluation of the IPSL-CM6A-LRclimate model.Journal of Advances inModeling Earth Systems,12,e2019MS002010, 2020.

Brune, S., A. Düsterhus, H. Pohlmann, W. A. Müller, and J. Baehr: Time dependency of the prediction skill for the north atlantic subpolar gyre in initialized decadal hindcasts. Climate dynamics, 51 (5), 1947–1970, 2018.

Brunner, L., Pendergrass, A. G., Lehner, F., Merrifield, A. L., Lorenz, R., and Knutti, R.: Reduced global warming from CMIP6 projections when weighting models by performance and independence, Earth Syst. Dynam., 11, 995–1012, https://doi.org/10.5194/esd-11-995-2020, 2020.

Cerdeiro, D.A., Komaromi, A., Liu, Y., Saeed, M.: World Seaborne Trade in Real Time: A Proof of Concept for Building AIS-based Nowcasts from Scratch. International Monetary Fund (IMF) WP/20/57, available at: https://www.imf.org/en/Publications/WP/Issues/2020/05/14/World-Seaborne-Trade-in-Real-Time-A-Proof-of-Concept-for-Building-AIS-based-Nowcasts-from-49393, last access: 21 January 2025, 2020.

Chatfield, C.: The Holt-Winters Forecasting Procedure, J. Roy. Stat. Soc. C., 27, 264–279, https://doi.org/10.2307/2347162, 1978.

Chen, Y., Hall, J., van Wees, D., Andela, N., Hantson, S., Giglio, L., van der Werf, G.R., Morton, D.C., and Randerson, J.T. (2023) Multi-decadal trends and variability in burned area from the fifth version of the Global Fire Emissions Database (GFED5). ESSD 15(11), 5227–5259 https://doi.org/10.5194/essd-15-5227-2023

Chini, L., Hurtt, G., Sahajpal, R., Frolking, S., Klein Goldewijk, K., Sitch, S., Ganzenmüller, R., Ma, L., Ott, L., Pongratz, J., and Poulter, B.: Land-use harmonization datasets for annual global carbon budgets, 13, 4175–4189, https://doi.org/10.5194/essd-13-4175-2021, 2021.

Clarke, D., Flachenecker, F., Guidetti, E., and Pionnier, P.-A.: CO2 Emissions from air transport: A near-real-time global database for policy analysis, Organization for Economic Co-operation and Development, Paris OECD Statistics Working Papers 2022/04, available at: https://doi.org/10.1787/ecc9f16b-en, last access: 21 January 2025, 2022.

Clarke, D., Chan P., Dequeljoe, M., Kim, Y., and Barahona, S.: CO2 emissions from global shipping: A new experimental database", OECD Statistics Working Papers, No. 2023/04, OECD Publishing, Paris, https://doi.org/10.1787/bc2f7599-en, 2023

Claverie, M., Matthews, J., Vermote, E., and Justice, C.: A 30+ Year AVHRR LAI and FAPAR Climate Data Record: Algorithm Description and Validation, Remote Sensing, 8, 263, https://doi.org/10.3390/rs8030263, 2016.

Collier, N., Hoffman, F. M., Lawrence, D. M., Keppel-Aleks, G., Koven, C. D., Riley, W. J., et al. (2018). The International Land Model Benchmarking (ILAMB) system: Design, theory, and implementation. Journal of Advances in Modeling Earth Systems, 10, 2731–2754. https://doi.org/10.1029/2018MS001354

Conchedda, G. and Tubiello, F. N.: Drainage of organic soils and GHG emissions: Validation with country data, Biosphere – Biogeosciences, https://doi.org/10.5194/essd-2020-202, 2020.

Cooper, D. J., Watson, A. J., and Ling, R. D.: Variation of pCO_2 along a North Atlantic shipping route (U.K. to the Caribbean): A year of automated observations, Marine Chemistry, 60, 147-164, 1998.

Crippa, M., Janssens-Maenhout, G., Guizzardi, D., Van Dingenen, R., and Dentener, F.: Contribution and uncertainty of sectorial and regional emissions to regional and global PM2.5 health impacts, 19, 5165–5186, https://doi.org/10.5194/acp-19-5165-2019, 2019.

Dai, A. and Trenberth, K. E.: Estimates of Freshwater Discharge from Continents: Latitudinal and Seasonal Variations, J. Hydrometeorol., 3, 660–687, https://doi.org/10.1175/1525-7541(2002)003<0660:EOFDFC>2.0.CO;2, 2002.

Davis, S. J. and Caldeira, K.: Consumption-based accounting of CO2 emissions, Proceedings of the National Academy of Sciences, 107, 5687–5692, https://doi.org/10.1073/pnas.0906974107, 2010.

de Boyer Montégut, C., G. Madec, A. S. Fischer, A. Lazar, and D. Iudicone (2004), Mixed layer depth over the global ocean: An examination of profile data and a profile-based climatology, J. Geophys. Res., 109, C12003, doi:10.1029/2004JC002378.

de Boyer Montégut Clément (2023). Mixed layer depth climatology computed with a density threshold criterion of 0.03kg/m3 from 10 m depth value. SEANOE. https://doi.org/10.17882/91774

De Kauwe, M. G., Disney, M. I., Quaife, T., Lewis, P., and Williams, M.: An assessment of the MODIS collection 5 leaf area index product for a region of mixed coniferous forest, Remote Sensing of Environment, 115, 767–780, https://doi.org/10.1016/j.rse.2010.11.004, 2011.

Dee, D. P., Uppala, S. M., Simmons, A. J., Berrisford, P., Poli, P., Kobayashi, S., ... & Vitart, F.. The ERA-Interim reanalysis: Configuration and performance of the data assimilation system. Quarterly Journal of the royal meteorological society, 137(656), 553-597, 2011.

DeVries, T. (2014), The oceanic anthropogenic CO2 sink: Storage, air-sea fluxes, and transports over the industrial era, Global Biogeochem. Cycles, 28, 631–647, doi:10.1002/2013GB004739.

Dickson, A. G., Sabine, C. L., and Christian, J. R.: Guide to best practices for ocean CO2 measurement. Sidney, British Columbia, North Pacific Marine Science Organization, 191pp. (PICES Special Publication 3; IOCCP Report 8). DOI: https://doi.org/10.25607/OBP-1342, 2007.

Dlugokencky, E. J., Lang, P. M., Masarie, K., Crotwell, A. M., and Crotwell, M. J.: Atmospheric carbon dioxide dry air mole fractions from the NOAA ESRL carbon cycle cooperative global air sampling network, 1968–2012, Version: 2013-08-27, available at: ftp://aftp.cmdl.noaa.gov/data/trace_gases/co2/flask/surface/, 2013.

Dou, X., Wang, Y., Ciais, P., Chevallier, F., Davis, S. J., Crippa, M., Janssens-Maenhout, G., Guizzardi, D., Solazzo, E., Yan, F., Huo, D., Zheng, B., Zhu, B., Cui, D., Ke, P., Sun, T., Wang, H., Zhang, Q., Gentine, P., Deng, Z., and Liu, Z.: Near-real-time global gridded daily CO2 emissions, The Innovation, 3, 100182, https://doi.org/10.1016/j.xinn.2021.100182, 2022.

Döscher, R., Acosta, M., Alessandri, A., Anthoni, P., Arneth, A., Arsouze, T., ... & Zhang, Q.: The EC-earth3 Earth system model for the climate model intercomparison project 6. Geoscientific Model Development Discussions, 2021, 1-90. 2021.

Duce, R. A., LaRoche, J., Altieri, K., Arrigo, K. R., Baker, A. R., Capone, D. G., Cornell, S., Dentener, F., Galloway, J., Ganeshram, R. S., Geider, R. J., Jickells, T., Kuypers, M. M., Langlois, R., Liss, P. S., Liu, S. M., Middelburg, J. J., Moore, C. M., Nickovic, S., Oschlies, A., Pedersen, T., Prospero, J., Schlitzer, R., Seitzinger, S., Sorensen, L. L., Uematsu, M., Ulloa, O., Voss, M., Ward, B., and Zamora, L.: Impacts of Atmospheric Anthropogenic Nitrogen on the Open Ocean, Science, 320, 893–897, https://doi.org/10.1126/science.1150369, 2008.

Eakins, B. W. and Sharman, G. F.: National Geophysical Data Center: Volumes of the World's Oceans from ETOPO1, available at: https://www.ngdc.noaa.gov/mgg/global/etopo1_ocean_volumes.html, last access: 21 January 2025, U.S. Department of Commerce, 2010.

Eurostat: Countries 2020, 1:1 million, available at: https://ec.europa.eu/eurostat/web/gisco/geodata/reference-data/administrative-units-statistical-units/countries, last access: 21 January 2025, 2024.

Eyring, V., Bony, S., Meehl, G. A., Senior, C. A., Stevens, B., Stouffer, R. J., and Taylor, K. E.: Overview of the Coupled Model Intercomparison Project Phase 6 (CMIP6) experimental design and organization, Geosci. Model Dev., 9, 1937–1958, https://doi.org/10.5194/gmd-9-1937-2016, 2016.

EIA: U.S. Energy Information Administration: Short-Term Energy Outlook, available at: http://www.eia.gov/forecasts/steo/outlook, last access: 21 January 2025, 2023.

FAO: Global Forest Resources Assessment 2020: Main report, FAO, Rome, Italy, 184 pp., https://doi.org/10.4060/ca9825en, 2020.

FAO: FAO Statistical Database (FAOSTAT), domains Climate Change, available at: http://www.fao.org/faostat/en/#data/GT, last access: 21 January 2025, 2021.

FAO: Land statistics 2001–2023 – Global, regional and country trends. FAOSTAT Analytical Briefs, No.107. Rome. https://doi.org/10.4060/cd5765en, 2025a.

FAO: FAOSTAT Emissions from Drained organic soils, available at http://www.fao.org/faostat/en/#data/GV, last access: 23 October 2025, 2025b.

FAO: FAOSTAT Emissions totals database, available at https://faostat.fao.org/internal/en/#data/GT, last access: 23 October 2025, FAO2025c.

FAO/UNEP: Food and Agriculture Organisation / United Nations Environment Programme: The state of food and agriculture 1981, available at: https://www.fao.org/3/ap661e/ap661e.pdf, last access: 21 January 2025, 1981.

Fay, A. R., Heimdal, T. H., Acquaviva, V., Shaum, A. P., McKinley, G. A. (2025) Sensitivity of ocean carbon sink estimates to rare observations. Geophysical Research Letters 52, e2025GL117961. doi:10.1029/2025GL117961.

Fay, A. R. and McKinley, G. A.: Global open-ocean biomes: mean and temporal variability, ESSD 6, 273–284, https://doi.org/10.5194/essd-6-273-2014, 2014.

Fischer, G., Nachtergaele, F., Prieler, S., van Velthuizen, H. T., Verelst, L., and Wiberg, D.: Global Agro-ecological Zones Assessment for Agriculture (GAEZ 2008). IIASA, Laxenburg, Austria and FAO, Rome, Italy, available at: https://www.fao.org/soils-portal/data-hub/soil-maps-and-databases/harmonized-world-soil-database-v12/land-cover-data/ar/, last access: 21 January 2025, 2008.

Ford, D. J., Blannin, J., Watts, J., Watson, A. J., Landschützer, P., Jersild, A. and Shutler, J. D.: A comprehensive analysis of air-sea CO2 flux uncertainties constructed from surface ocean data products, Global Biogeochemical Cycles, 38, e2024GB008188, doi: 10.1029/2024GB008188., 2024

Ford, D.J., Shutler, J.D., Blanco-Sacristán, J. et al. Enhanced ocean CO2 uptake due to near-surface temperature gradients. Nat. Geosci. 17, 1135–1140 . https://doi.org/10.1038/s41561-024-01570-7, 2024a

Ford, D. J., Shutler, J. D., Ashton, I.,Sims, R. P., & Holding, T. (2025). Recalculated (depth and temperature consistent) surface ocean CO_2 atlas (SOCAT) version 2025 (v0-1) [Data set]. Zenodo. https://doi.org/10.5281/zenodo.15656803

Fu, W., Moore, J. K., Primeau, F., Collier, N., Ogunro, O. O., Hoffman, F. M., & Randerson, J. T. (2022). Evaluation of ocean biogeochemistry and carbon cycling in CMIP earth system models with the International Ocean Model Benchmarking (IOMB) software system. Journal of Geophysical Research: Oceans, 127, e2022JC018965. https://doi.org/10.1029/2022JC018965

Gasser, T. and Ciais, P.: A theoretical framework for the net land-to-atmosphere CO2 flux and its implications in the definition of "emissions from land-use change", Earth Syst. Dynam., 4, 171–186, https://doi.org/10.5194/esd-4-171-2013, 2013.

GCCA. Concrete Future: The GCCA 2050 Cement and Concrete Industry Roadmap for Net Zero Concrete, available at: https://gccassociation.org/concretefuture/ last access: 2 August 2022, 2021.

Gkritzalis, T., Bakker, D. C. E., Lauvset, S. K. and Steinhoff, T. (2024) SOCAT Quality Control Cookbook – For version 2025 of the Surface Ocean CO2 Atlas. 26 pp. Published on 18/12/2024. Available here: https://socat.info/wp-content/uploads/2025/01/2024_SOCAT_QC_Cookbook_Update.pdf. Last access 22/05/2025.

Goddijn-Murphy, L. M., Woolf, D. K., Land, P. E., Shutler, J. D., and Donlon, C.: The OceanFlux Greenhouse Gases methodology for deriving a sea surface climatology of CO2 fugacity in support of air–sea gas flux studies, 11, 519–541, https://doi.org/10.5194/os-11-519-2015, 2015.

Golar, G., Malik, A., Muis, H., Herman, A., Nurudin, N., and Lukman, L.: The social-economic impact of COVID-19 pandemic: implications for potential forest degradation, Heliyon, 6, e05354, https://doi.org/10.1016/j.heliyon.2020.e05354, 2020.

Good, S. A., Martin, M. J., and Rayner, N. A.: EN4: Quality controlled ocean temperature and salinity profiles and monthly objective analyses with uncertainty estimates, Journal of Geophysical Research: Oceans, 118, 6704–6716, https://doi.org/10.1002/2013JC009067, 2013.

Gouretski, V. and Cheng, L.: Correction for Systematic Errors in the Global Dataset of Temperature Profiles from Mechanical Bathythermographs, Journal of Atmospheric and Oceanic Technology, 37, 841–855, https://doi.org/10.1175/JTECH-D-19-0205.1, 2020.

Gouretski, V. and Reseghetti, F.: On depth and temperature biases in bathythermograph data: Development of a new correction scheme based on analysis of a global ocean database, Deep Sea Research Part I: Oceanographic Research Papers, 57, 812–833, https://doi.org/10.1016/j.dsr.2010.03.011, 2010.

Grassi, G., House, J., Kurz, W. A., Cescatti, A., Houghton, R. A., Peters, G. P., Sanz, M. J., Viñas, R. A., Alkama, R., Arneth, A., Bondeau, A., Dentener, F., Fader, M., Federici, S., Friedlingstein, P., Jain, A. K., Kato, E., Koven, C. D., Lee, D., Nabel, J. E. M. S., Nassikas, A. A., Perugini, L., Rossi, S., Sitch, S., Viovy, N., Wiltshire, A., and Zaehle, S.: Reconciling global-model estimates and country reporting of anthropogenic forest CO2 sinks, Nature Clim Change, 8, 914–920, https://doi.org/10.1038/s41558-018-0283-x, 2018.

Grassi, G., Stehfest, E., Rogelj, J., van Vuuren, D., Cescatti, A., House, J., Nabuurs, G.-J., Rossi, S., Alkama, R., Viñas, R. A., Calvin, K., Ceccherini, G., Federici, S., Fujimori, S., Gusti, M., Hasegawa, T., Havlik, P., Humpenöder, F., Korosuo, A., Perugini, L., Tubiello, F. N., and Popp, A.: Critical adjustment of land mitigation pathways for assessing countries' climate progress, Nat. Clim. Chang., 11, 425–434, https://doi.org/10.1038/s41558-021-01033-6, 2021.

Grassi, G., Conchedda, G., Federici, S., Abad Viñas, R., Korosuo, A., Melo, J., Rossi, S., Sandker, M., Somogyi, Z., and Tubiello, F. N.: Carbon fluxes from land 2000–2020: bringing clarity on countries' reporting, Biogeosciences and biodiversity, https://doi.org/10.5194/essd-2022-104, 2022.

Grassi, G., Schwingshackl, C., Gasser, T., Houghton, R. A., Sitch, S., Canadell, J. G., Cescatti, A., Ciais, P., Federici, S., Friedlingstein, P., Kurz, W. A., Sanz Sanchez, M. J., Abad Viñas, R., Alkama, R., Bultan, S., Ceccherini, G., Falk, S., Kato, E., Kennedy, D., Knauer, J., Korosuo, A., Melo, J., McGrath, M. J., Nabel, J. E. M. S., Poulter, B., Romanovskaya, A. A., Rossi, S., Tian, H., Walker, A. P., Yuan, W., Yue, X., and Pongratz, J.: Harmonising the land-use flux estimates of global models and national inventories for 2000–2020, Earth Syst. Sci. Data, 15, 1093–1114, https://doi.org/10.5194/essd-15-1093-2023, 2023.

Gregg, J. S., Andres, R. J., and Marland, G.: China: Emissions pattern of the world leader in CO 2 emissions from fossil fuel consumption and cement production, Geophys. Res. Lett., 35, L08806, https://doi.org/10.1029/2007GL032887, 2008.

Gregor, Luke; Gruber, Nicolas (2020). OceanSODA-ETHZ: A global gridded dataset of the surface ocean carbonate system for seasonal to decadal studies of ocean acidification (v2023) (NCEI Accession 0220059). [indicate subset used]. NOAA National Centers for Environmental Information. Dataset. https://doi.org/10.25921/m5wx-ja34. Accessed 24 October 2025.

Gürses, Ö., Oziel, L., Karakuş, O., Sidorenko, D., Völker, C., Ye, Y., Zeising, M., Butzin, M., and Hauck, J.: Ocean biogeochemistry in the coupled ocean–sea ice–biogeochemistry model FESOM2.1–REcoM3, Geoscientific Model Development, 16, 4883–4936, https://doi.org/10.5194/gmd-16-4883-2023, 2023.

Hansen, M. C., Potapov, P. V., Moore, R., Hancher, M., Turubanova, S. A., Tyukavina, A., Thau, D., Stehman, S. V., Goetz, S. J., Loveland, T. R., Kommareddy, A., Egorov, A., Chini, L., Justice, C. O., and Townshend, J. R. G.: High-Resolution Global Maps of 21st-Century Forest Cover Change, Science, 342, 850–853, https://doi.org/10.1126/science.1244693, 2013.

Harris, I., Jones, P. D., Osborn, T. J., and Lister, D. H.: Updated high-resolution grids of monthly climatic observations - the CRU TS3.10 Dataset, Int. J. Climatol., 34, 623–642, https://doi.org/10.1002/joc.3711, 2014.

Harris, I., Osborn, T. J., Jones, P., and Lister, D.: Version 4 of the CRU TS monthly high-resolution gridded multivariate climate dataset, Sci Data, 7, 109, https://doi.org/10.1038/s41597-020-0453-3, 2020.

Hashimoto, S., Carvalhais, N., Ito, A., Migliavacca, M., Nishina, K. and Reichstein, M.: Global spatiotemporal distribution of soil respiration modeled using a global database. Biogeosciences, 12(13), pp.4121-4132, 2015.

Hashimoto, S., Ito, A. and Nishina, K.: Divergent data-driven estimates of global soil respiration. Communications Earth & Environment, 4(1), p.460, 2023.

Hefner, M., Marland, G., Boden, T., Andres, R.: Global, Regional, and National Fossil-Fuel CO2 Emissions: 1751-2020 CDIAC-FF, Appalachian Energy Centre [data set], available at: https://energy.appstate.edu/cdiac-appstate/data-products, last access: 21 January 2025, 2023.

Heinimann, A., Mertz, O., Frolking, S., Christensen, A. E., Hurni, K., Sedano, F., Chini, L. P., Sahajpal, R., Hansen, M., and Hurtt, G.: A global view of shifting cultivation: Recent, current, and future extent, PLOS ONE, 12, e0184479, https://doi.org/10.1371/journal.pone.0184479, 2017.

Hersbach, H., Bell, B., Berrisford, P., Hirahara, S., Horányi, A., Muñoz-Sabater, J., ... & Thépaut, J. N.: The ERA5 global reanalysis. Quarterly Journal of the Royal Meteorological Society, 146(730), 1999-2049, 2020.

Hertwich, E. G. and Peters, G. P.: Carbon Footprint of Nations: A Global, Trade-Linked Analysis, Environ. Sci. Technol., 43, 6414–6420, https://doi.org/10.1021/es803496a, 2009.

Ho, D. T., Wanninkhof, R., Schlosser, P., Ullman, D. S., Hebert, D., and Sullivan, K. F.: Toward a universal relationship between wind speed and gas exchange: Gas transfer velocities measured with 3He/SF6 during the Southern Ocean Gas Exchange Experiment, J. Geophys. Res.-Oceans, 116, C00F04, https://doi.org/10.1029/2010JC006854, 2011.

Hobeichi, S., Abramowitz, G., Evans, J., and Beck, H. E.: Linear Optimal Runoff Aggregate (LORA): a global gridded synthesis runoff product, Hydrol. Earth Syst. Sci., 23, 851–870, https://doi.org/10.5194/hess-23-851-2019, 2019.

Hobeichi, S., Abramowitz, G., and Evans, J.: Conserving Land–Atmosphere Synthesis Suite (CLASS), Journal of Climate, 33, 1821–1844, https://doi.org/10.1175/JCLI-D-19-0036.1, 2020.

Houghton, R. A.: Why are estimates of the terrestrial carbon balance so different?, Glob. Change Biol., 9, 500–509, https://doi.org/10.1046/j.1365-2486.2003.00620.x, 2003.

Houghton, R. A. and Nassikas, A. A.: Global and regional fluxes of carbon from land use and land cover change 1850-2015: Carbon Emissions From Land Use, Global Biogeochem. Cycles, 31, 456–472, https://doi.org/10.1002/2016GB005546, 2017.

Hauck, J., Gregor, L., Nissen, C., Patara, L., Hague, M., Mongwe, P., Bushinsky, S., Doney, S. C., Gruber, N., Le Quéré, C., Manizza, M., Mazloff, M., Monteiro, P. M. S., & Terhaar, J.: The Southern Ocean Carbon Cycle 1985–2018: Mean, Seasonal Cycle, Trends, and Storage. Global Biogeochemical Cycles, 37(11), e2023GB007848. https://doi.org/10.1029/2023GB007848, 2023b.

Huang, Z., Wang, J., Bing, L., Qiu, Y., Guo, R., Yu, Y., Ma, M., Niu, L., Tong, D., Andrew, R. M., Friedlingstein, P., Canadell, J. G., Xi, F., and Liu, Z.: Global carbon uptake of cement carbonation accounts 1930–2021, Earth Syst. Sci. Data, 15, 4947–4958, https://doi.org/10.5194/essd-15-4947-2023, 2023.

Hugelius, G., Bockheim, J. G., Camill, P., Elberling, B., Grosse, G., Harden, J. W., Johnson, K., Jorgenson, T., Koven, C. D., Kuhry, P., Michaelson, G., Mishra, U., Palmtag, J., Ping, C.-L., O'Donnell, J., Schirrmeister, L., Schuur, E. A. G., Sheng, Y., Smith, L. C., Strauss, J., and Yu, Z.: A new data set for estimating organic carbon storage to 3 m depth in soils of the northern circumpolar permafrost region, Earth Syst. Sci. Data, 5, 393–402, https://doi.org/10.5194/essd-5-393-2013, 2013.

Hui, D., & Jackson, R. B. (2006). Geographical and interannual variability in biomass partitioning in grassland ecosystems: a modeling analysis. Proceedings of the National Academy of Sciences of the United States of America (PNAS), 103(39), 14271–14275. https://doi.org/10.1073/pnas.0604342103

Humphreys, M. P., Lewis, E. R., Sharp, J. D., and Pierrot, D.: PyCO2SYS v1.8: marine carbonate system calculations in Python, Geosci. Model Dev., 15, 15–43, https://doi.org/10.5194/gmd-15-15-2022, 2022.

Hurtt, G., Chini, L., Sahajpal, R., Frolking, S., Bodirsky, B. L., Calvin, K., Doelman, J., Fisk, J., Fujimori, S., Klein Goldewijk, K., Hasegawa, T., Havlik, P., Heinimann, A., Humpenöder, F., Jungclaus, J., Kaplan, J., Krisztin, T., Lawrence, D., Lawrence, P., Mertz, O., Pongratz, J., Popp, A., Riahi, K., Shevliakova, E., Stehfest, E., Thornton, P., van Vuuren, D., and Zhang, X.: input4MIPs.CMIP6.CMIP.UofMD.UofMD-landState-2-1-h, World Climate Research Programme [dataset], https://doi.org/10.22033/ESGF/input4MIPs.1127, 2017.

Hurtt, G. C., Chini, L. P., Frolking, S., Betts, R. A., Feddema, J., Fischer, G., Fisk, J. P., Hibbard, K., Houghton, R. A., Janetos, A., Jones, C. D., Kindermann, G., Kinoshita, T., Klein Goldewijk, K., Riahi, K., Shevliakova, E., Smith, S., Stehfest, E., Thomson, A., Thornton, P., van Vuuren, D. P., and Wang, Y. P.: Harmonization of land-use scenarios for the period 1500–2100: 600 years of global gridded annual land-use transitions, wood harvest, and resulting secondary lands, Climatic Change, 109, 117–161, https://doi.org/10.1007/s10584-011-0153-2, 2011.

Hurtt, G. C., Chini, L., Sahajpal, R., Frolking, S., Bodirsky, B. L., Calvin, K., Doelman, J. C., Fisk, J., Fujimori, S., Klein Goldewijk, K., Hasegawa, T., Havlik, P., Heinimann, A., Humpenöder, F., Jungclaus, J., Kaplan, J. O., Kennedy, J., Krisztin, T., Lawrence, D., Lawrence, P., Ma, L., Mertz, O., Pongratz, J., Popp, A., Poulter, B., Riahi, K., Shevliakova, E., Stehfest, E., Thornton, P., Tubiello, F. N., van Vuuren, D. P., and Zhang, X.: Harmonization of global land use change and management for the period 850–2100 (LUH2) for CMIP6, Geosci. Model Dev., 13, 5425–5464, https://doi.org/10.5194/gmd-13-5425-2020, 2020.

IEA/OECD: International Energy Agency/Organisation for Economic Cooperation and Development: CO_2 emissions from fuel combustion, available at: https://webstore.iea.org/co2-emissions-from-fuel-combustion-2019-highlights, last access: 21 January 2025, 2019.

Iida, Y., Kojima, A., Takatani, Y., Nakano, T., Sugimoto, H., Midorikawa, T., and Ishii, M.: Trends in pCO_2 and sea–air CO_2 flux over the global open oceans for the last two decades, J Oceanogr, 71, 637–661, https://doi.org/10.1007/s10872-015-0306-4, 2015.

Ilyina, T., Six, K. D., Segschneider, J., Maier-Reimer, E., Li, H., and Núñez-Riboni, I.: Global ocean biogeochemistry model HAMOCC: Model architecture and performance as component of the MPI-Earth system model in different CMIP5 experimental realizations: The Model Hamocc within Mpi-Esm in Cmip5, J. Adv. Model. Earth Syst., 5, 287–315, https://doi.org/10.1029/2012MS000178, 2013.

Inness, A., Ades, M., Agustí-Panareda, A., Barré, J., Benedictow, A., Blechschmidt, A.-M., Dominguez, J. J., Engelen, R., Eskes, H., Flemming, J., Huijnen, V., Jones, L., Kipling, Z., Massart, S., Parrington, M., Peuch, V.-H., Razinger, M., Remy, S., Schulz, M., and Suttie, M.: The CAMS reanalysis of atmospheric composition, 19, 3515–3556, https://doi.org/10.5194/acp-19-3515-2019, 2019.

Intergovernmental Panel on Climate Change (IPCC): Climate Change 2021: The Physical Science Basis. Contribution of Working Group I to the Sixth Assessment Report of the Intergovernmental Panel on Climate Change. Edited by V. Masson-Delmotte, P. Zhai, A. Pirani, S. L. Connors, C. Péan, S. Berger, N. Caud, Y. Chen, L. Goldfarb, M. I. Gomis, M. Huang, K. Leitzell, E. Lonnoy, J. B. R. Matthews, T. K. Maycock, T. Waterfield, O. Yelekçi, R. Yu, and B. Zhou. Cambridge University Press, Cambridge, UK and New York, NY, USA. https://doi.org/10.1017/9781009157896, 2021.

Intergovernmental Panel on Climate Change (IPCC): 2006 IPCC Guidelines for National Greenhouse Gas Inventories, Prepared by the National Greenhouse Gas Inventories Programme, Eggleston H.S., Buendia L., Miwa K., Ngara T. and Tanabe K. (eds). Published: IGES, Japan, 2006.

Ishii, M., and M., Kimoto: Reevaluation of historical ocean heat content variations with time-varying XBT and MBT depth bias corrections. Journal of Oceanography, 65(3), 287–299, 2009.

Iversen, C. M., McCormack, M. L., Powell, A. S., Blackwood, C. B., Freschet, G. T., Kattge, J., Roumet, C., Stover, D. B., Soudzilovskaia, N. A., Valverde-Barrantes, O. J., van Bodegom, P. M., & Violle, C. (2017). A global fine-root ecology database to address below-ground challenges in plant ecology. New Phytologist, 215, 15-26. https://doi.org/10.1111/nph.14486

Jackson, R. B., Lajtha, K., Crow, S. E., Hugelius, G., Kramer, M. G., & Piñeiro, G. (2017). The ecology of soil carbon: pools, vulnerabilities, and biotic and abiotic controls. Annual Review of Ecology, Evolution, and Systematics, 48, 419-445. https://doi.org/10.1146/annurev-ecolsys-112414-054234

Jähne, B.: Air-Sea Gas Exchange, in: Encyclopedia of Ocean Sciences, Elsevier, 1–13, https://doi.org/10.1016/B978-0-12-409548-9.11613-6, 2019.

Jähne, B. and Haußecker, H.: Air-water gas exchange, Annu. Rev. Fluid Mech., 30, 443–468, https://doi.org/10.1146/annurev.fluid.30.1.443, 1998.

JODI: Joint Organisations Data Initiative, available at: https://www. jodidata.org, last access: 21 January 2025, 2022.

Jones, M.W., Andrew, R.M., Peters, G.P. et al., 2021: Gridded fossil CO2 emissions and related O2 combustion consistent with national inventories 1959–2018. Sci Data 8, 2. https://doi.org/10.1038/s41597-020-00779-6

Jones, M. W., Andrew, R. M., Peters, G. P., Janssens-Maenhout, G., De-Gol, A. J., Dou, X., Liu, Z., Pickers, P., Ciais, P., Patra, P. K., Chevallier, F., and Le Quéré, C.: Gridded fossil CO2 emissions and related O2 combustion consistent with national inventories 1959-2022, Zenodo [dataset], https://doi.org/10.5281/zenodo.8386803, 2023.

Jung, M., Reichstein, M., Schwalm, C. R., Huntingford, C., Sitch, S., Ahlström, A., Arneth, A., Camps-Valls, G., Ciais, P., Friedlingstein, P., Gans, F., Ichii, K., Jain, A. K., Kato, E., Papale, D., Poulter, B., Raduly, B., Rödenbeck, C., Tramontana, G., Viovy, N., Wang, Y.-P., Weber, U., Zaehle, S., and Zeng, N.: Compensatory water effects link yearly global land CO2 sink changes to temperature, Nature, 541, 516–520, https://doi.org/10.1038/nature20780, 2017.

Keppler, L., Landschützer, P., Lauvset, S. K., and Gruber, N.: Recent Trends and Variability in the Oceanic Storage of Dissolved Inorganic Carbon, Global Biogeochemical Cycles, 37, e2022GB007677, https://doi.org/10.1029/2022GB007677, 2023.

Keeling, R. F. and Manning, A. C.: 5.15 - Studies of Recent Changes in Atmospheric O2 Content, in: Treatise on Geochemistry (Second Edition), edited by: Holland, H. D. and Turekian, K. K., Elsevier, Oxford, 385–404, https://doi.org/10.1016/B978-0-08-095975-7.00420-4, 2014.

Khatiwala, S., Tanhua, T., Mikaloff Fletcher, S., Gerber, M., Doney, S. C., Graven, H. D., Gruber, N., McKinley, G. A., Murata, A., Ríos, A. F., & Sabine, C. L. (2013). Global ocean storage of anthropogenic carbon. Biogeosciences, 10(4), 2169–2191. https://doi.org/10.5194/bg-10-2169-2013

Klein Goldewijk, K., Beusen, A., Doelman, J., and Stehfest, E.: Anthropogenic land use estimates for the Holocene – HYDE 3.2, Earth Syst. Sci. Data, 9, 927–953, https://doi.org/10.5194/essd-9-927-2017, 2017a.

Klein Goldewijk, K., Dekker, S. C., and van Zanden, J. L.: Per-capita estimations of long-term historical land use and the consequences for global change research, J. Land Use Sci., 12, 313–337, https://doi.org/10.1080/1747423X.2017.1354938, 2017b.

Knauer, J., Zaehle, S., Medlyn, B. E., Reichstein, M., Williams, C. A., Migliavacca, M., De Kauwe, M. G., Werner, C., Keitel, C., Kolari, P., Limousin, J., and Linderson, M.: Towards physiologically meaningful water-use efficiency estimates from eddy covariance data, Global Change Biology, 24, 694–710, https://doi.org/10.1111/gcb.13893, 2018.

Kobayashi, S., Ota, Y., Harada, Y., Ebita, A., Moriya, M., Onoda, H., Onogi, K., Kamahori, H., Kobayashi, C., Endo, H., Miyaoka, K., and Takahashi, K.: The JRA-55 Reanalysis: General Specifications and Basic Characteristics, Journal of the Meteorological Society of Japan, 93, 5–48, https://doi.org/10.2151/jmsj.2015-001, 2015.

Koven, C., Hugelius, G., Lawrence, D. et al. Higher climatological temperature sensitivity of soil carbon in cold than warm climates. Nature Clim Change 7, 817–822,. https://doi.org/10.1038/nclimate3421, 2017,

Lamboll, R. D., Jones, C. D., Skeie, R. B., Fiedler, S., Samset, B. H., Gillett, N. P., Rogelj, J., Forster, P. M.: Modifying emissions scenario projections to account for the effects of COVID-19: protocol for CovidMIP, Geosci. Model Dev., 14, 3683–3695, https://doi.org/10.5194/gmd-14-3683-2021, 2021.

Landschützer, P., Gruber, N., Bakker, D. C. E., and Schuster, U.: Recent variability of the global ocean carbon sink, Global Biogeochem. Cycles, 28, 927–949, https://doi.org/10.1002/2014GB004853, 2014.

Landschützer, P., Laruelle, G. G., Roobaert, A., and Regnier, P.: A uniform pCO_2 climatology combining open and coastal oceans, 12, 2537–2553, https://doi.org/10.5194/essd-12-2537-2020, 2020.

Lasslop, G., Reichstein, M., Papale, D., Richardson, A. D., Arneth, A., Barr, A., Stoy, P., and Wohlfahrt, G.: Separation of net ecosystem exchange into assimilation and respiration using a light response curve approach: critical issues and global evaluation: Separation of NEE into GPP and RECO, Glob. Change Biol., 16, 187–208, https://doi.org/10.1111/j.1365-2486.2009.02041.x, 2010.

Lauvset, S. K., Key, R. M., Olsen, A., van Heuven, S., Velo, A., Lin, X., Schirnick, C., Kozyr, A., Tanhua, T., Hoppema, M., Jutterström, S., Steinfeldt, R., Jeansson, E., Ishii, M., Perez, F. F., Suzuki, T., and Watelet, S.: A new global interior ocean mapped climatology: the 1° × 1° GLODAP version 2, Earth System Science Data, 8, 325–340, https://doi.org/10.5194/essd-8-325-2016, 2016.

Lauvset, S. K., Lange, N., Tanhua, T., Bittig, H. C., Olsen, A., Kozyr, A., Alin, S., Álvarez, M., Azetsu-Scott, K., Barbero, L., Becker, S., Brown, P. J., Carter, B. R., Da Cunha, L. C., Feely, R. A., Hoppema, M., Humphreys, M. P., Ishii, M., Jeansson, E., Jiang, L.-Q., Jones, S. D., Lo Monaco, C., Murata, A., Müller, J. D., Pérez, F. F., Pfeil, B., Schirnick, C., Steinfeldt, R., Suzuki, T., Tilbrook, B., Ulfsbo, A., Velo, A., Woosley, R. J., and Key, R. M.: GLODAPv2.2022: the latest version of the global interior ocean biogeochemical data product, Earth Syst. Sci. Data, 14, 5543–5572, https://doi.org/10.5194/essd-14-5543-2022, 2022.

Lauvset, S. K., Lange, N., Tanhua, T., Bittig, H. C., Olsen, A., Kozyr, A., Álvarez, M., Azetsu-Scott, K., Brown, P. J., Carter, B. R., Cotrim da Cunha, L., Hoppema, M., Humphreys, M. P., Ishii, M., Jeansson, E., Murata, A., Müller, J. D., Pérez, F. F., Schirnick, C., Steinfeldt, R., Suzuki, T., Ulfsbo, A., Velo, A., Woosley, R. J., and Key, R. M.: The annual update GLODAPv2.2023: the global interior ocean biogeochemical data product, Earth Syst. Sci. Data, 16, 2047–2072, https://doi.org/10.5194/essd-16-2047-2024, 2024

Lienert, S. and Joos, F.: A Bayesian ensemble data assimilation to constrain model parameters and land-use carbon emissions, Biogeosciences, 15, 2909–2930, https://doi.org/10.5194/bg-15-2909-2018, 2018.

Li, H., Ilyina, T., Loughran, T., Spring, A., and Pongratz, J.: Reconstructions and predictions of the global carbon budget with an emission-driven Earth system model, Earth Syst. Dyn., 14, 101–119, https://doi.org/10.5194/esd-14-101-2023, 2023.

Liptak, J., Keppel-Aleks, G., and Lindsay, K. (2017) Drivers of multi-century trends in the atmospheric CO2 mean annual cycle in a prognostic ESM. Biogeosciences, 14, 1383–1401 https://bg.copernicus.org/articles/14/1383/2017/bg-14-1383-2017.pdf

Liu, Z., Ciais, P., Deng, Z., Davis, S. J., Zheng, B., Wang, Y., Cui, D., Zhu, B., Dou, X., Ke, P., Sun, T., Guo, R., Zhong, H., Boucher, O., Bréon, F.-M., Lu, C., Guo, R., Xue, J., Boucher, E., Tanaka, K., and Chevallier, F.: Carbon Monitor, a near-real-time daily dataset of global CO2 emission from fossil fuel and cement production, Sci Data, 7, 392, https://doi.org/10.1038/s41597-020-00708-7, 2020a.

Liu, Z., Ciais, P., Deng, Z., Lei, R. Davis, S. J., Feng, S., Zheng, B., Cui, D., Dou, X., Zhu, B., Guo, R., Ke, P., Sun, T., Lu, C., He, P., Wang, Y., Yue, X., Wang, Y., Lei, Y., Zhou, H., Cai, Z., Wu, Y., Guo, R., Han, T., Xue, J., Boucher, O., Boucher, E., Chevallier, F., Tanaka, K., Wei, Y., Zhong, H., Kang, C., Zhang, N., Chen, B., Xi, F., Liu, M., Bréon, F.-M., Lu, Y., Zhang, Q., Guan, D., Gong, P., Kammen, D. M., He, K., and Schellnhuber, H. J.: Near-real-time monitoring of global CO2 emissions reveals the effects of the COVID-19 pandemic, Nat Commun, 11, 5172, https://doi.org/10.1038/s41467-020-18922-7, 2020b.

Locarnini, R.A., A.V. Mishonov, O.K. Baranova, J.R. Reagan, T.P. Boyer, D. Seidov, Z. Wang, H.E. Garcia, C. Bouchard, S.L. Cross, C.R. Paver, and D. Dukhovskoy. World Ocean Atlas 2023, Volume 1: Temperature. A. Mishonov Technical Ed. NOAA Atlas NESDIS 89, doi.org/10.25923/54bh-1613

Lueker, T. J., Dickson, A. G., and Keeling, C. D.: Ocean pCO_2 calculated from dissolved inorganic carbon, alkalinity, and equations for K1 and K2: validation based on laboratory measurements of CO_2 in gas and seawater at equilibrium, Mar. Chem., 70, 105–119, https://doi.org/10.1016/S0304-4203(00)00022-0, 2000.

Ma, L., Hurtt, G. C., Chini, L. P., Sahajpal, R., Pongratz, J., Frolking, S., Stehfest, E., Klein Goldewijk, K., O'Leary, D., and Doelman, J. C.: Global rules for translating land-use change (LUH2) to land-cover change for CMIP6 using GLM2, Geosci. Model Dev., 13, 3203–3220, https://doi.org/10.5194/gmd-13-3203-2020, 2020.

Maki, T., Ikegami, M., Fujita, T., Hirahara, T., Yamada, K., Mori, K., Takeuchi, A., Tsutsumi, Y., Suda, K., and Conway, T. J.: New technique to analyse global distributions of CO2 concentrations and fluxes from non-processed observational data, Tellus B., 62, 797–809, https://doi.org/10.1111/j.1600-0889.2010.00488.x, 2010.

MapBiomas Brasil. Collection 9 of annual maps of land cover and land use in Brazil, accessed on 04/2025 through the link: https://brasil.mapbiomas.org/estatisticas/

MapBiomas Indonesia. Collection 3 of annual maps of land cover and land use in Indonesia, accessed on 03/2025 through the link: https://platform.indonesia.mapbiomas.org/

McCarthy, G. D., Smeed, D. A., Johns, W. E., Frajka-Williams, E., Moat, B. I., Rayner, D., Baringer, M. O., Meinen, C. S., Collins, J., & Bryden, H. L. (2015). Measuring the Atlantic Meridional Overturning Circulation at 26°N. Progress in Oceanography, 130, 91–111. https://doi.org/10.1016/j.pocean.2014.10.006

Mokany, K., Raison, R. J., & Prokushkin, A. S. (2006). Critical analysis of root:shoot ratios in terrestrial biomes. Global Change Biology, 15, 129-144. doi: 10.1111/j.1365-2486.2005.001043.x

Manning, A. and Keeling, R. F.: Global oceanic and land biotic carbon sinks from the Scripps atmospheric oxygen flask sampling network, Tellus B Chem. Phys. Meteorol., 58, 95–116, https://doi.org/10.1111/j.1600-0889.2006.00175.x, 2006.

Marland, G.: Uncertainties in Accounting for CO 2 From Fossil Fuels, J. Indust. Ecol., 12, 136–139, https://doi.org/10.1111/j.1530-9290.2008.00014.x, 2008.

Marland, G., Hamal, K., and Jonas, M.: How Uncertain Are Estimates of CO2 Emissions?, J. Indust. Ecol., 13, 4–7, https://doi.org/10.1111/j.1530-9290.2009.00108.x, 2009.

Martens, B., Miralles, D. G., Lievens, H., Van Der Schalie, R., De Jeu, R. A. M., Fernández-Prieto, D., Beck, H. E., Dorigo, W. A., and Verhoest, N. E. C.: GLEAM v3: satellite-based land evaporation and root-zone soil moisture, Geosci. Model Dev., 10, 1903–1925, https://doi.org/10.5194/gmd-10-1903-2017, 2017.

Mauritsen, T. et al.: Developments in the MPI-M Earth System Model version 1.2 (MPI-ESM1. 2) and its response to increasing CO2. Journal of Advances in Modeling Earth Systems, 11 (4), 998–1038, 2019.

McNeil, B. I.: Anthropogenic CO2 Uptake by the Ocean Based on the Global Chlorofluorocarbon Data Set, Science, 299, 235–239, https://doi.org/10.1126/science.1077429, 2003.

Mikaloff Fletcher, S. E., Gruber, N., Jacobson, A. R., Doney, S. C., Dutkiewicz, S., Gerber, M., Follows, M., Joos, F., Lindsay, K., Menemenlis, D., Mouchet, A., Müller, S. A., and Sarmiento, J. L.: Inverse estimates of anthropogenic CO2 uptake, transport, and storage by the ocean, Glob. Biogeochem. Cycles, 20, GB2002, https://doi.org/10.1029/2005GB002530, 2006.

Miralles, D. G., Holmes, T. R. H., De Jeu, R. A. M., Gash, J. H., Meesters, A. G. C. A., and Dolman, A. J.: Global land-surface evaporation estimated from satellite-based observations, Hydrol. Earth Syst. Sci., 15, 453–469, https://doi.org/10.5194/hess-15-453-2011, 2011.

Moat B.I.; Smeed D.A.; Rayner D.; Johns W.E.; Smith, R.; Volkov, D.; Elipot S.; Petit T.; Kajtar J.; Baringer M. O.; and Collins, J. (2025). Atlantic meridional overturning circulation observed by the RAPID-MOCHA-WBTS (RAPID-Meridional Overturning Circulation and Heatflux Array-Western Boundary Time Series) array at 26N from 2004 to 2024 (v2024.1),

British Oceanographic Data Centre - Natural Environment Research Council, UK. doi: 10.5285/3f24651e-2d44-dee3-e063-7086abc0395e

Mu, Q., Zhao, M., and Running, S. W.: Improvements to a MODIS global terrestrial evapotranspiration algorithm, Remote Sensing of Environment, 115, 1781–1800, https://doi.org/10.1016/j.rse.2011.02.019, 2011.

Müller, J. and Joos, F.: Global peatland area and carbon dynamics from the Last Glacial Maximum to the present – a process-based model investigation, Biogeosciences, 17, 5285–5308, https://doi.org/10.5194/bg-17-5285-2020, 2020.

Müller, J. and Joos, F.: Committed and projected future changes in global peatlands – continued transient model simulations since the Last Glacial Maximum, Biogeosciences, 18, 3657–3687, https://doi.org/10.5194/bg-18-3657-2021, 2021.

Myneni, R. B., Ramakrishna, R., Nemani, R., and Running, S. W.: Estimation of global leaf area index and absorbed par using radiative transfer models, IEEE Trans. Geosci. Remote Sensing, 35, 1380–1393, https://doi.org/10.1109/36.649788, 1997.

Naegler, T.: Reconciliation of excess 14C-constrained global CO2 piston velocity estimates, Tellus B., 61, 372–384, https://doi.org/10.1111/j.1600-0889.2008.00408.x, 2009.

Nakamura, T., Yamazaki, K., Iwamoto, K., Honda, M., Miyoshi, Y., Ogawa, Y., and Ukita, J.: A negative phase shift of the winter AO/NAO due to the recent Arctic sea-ice reduction in late autumn, J. Geophys. Res. Atmos., 120, 3209–3227, https://doi.org/10.1002/2014JD022848, 2015.

Narayanan, B., Aguiar, A., and McDougall, R.: Global Trade, Assistance, and Production: The GTAP 9 Data Base, Cent. Glob. Trade Anal. Purdue Univ., available at: https:// www.gtap.agecon.purdue.edu/databases/v9/default.asp, last access: 21 January 2025, 2015.

Nightingale, P. D., Liss, P. S., and Schlosser, P.: Measurements of air-sea gas transfer during an open ocean algal bloom, Geophys. Res. Lett., 27, 2117–2120, https://doi.org/10.1029/2000GL011541, 2000.

Ogunro, O. O., Elliott, S. M., Wingenter, O. W., Deal, C., Fu, W., Collier, N., & Hoffman, F. M. (2018). Evaluating Uncertainties in Marine Biogeochemical Models: Benchmarking Aerosol Precursors. Atmosphere, 9(5), 184. https://doi.org/10.3390/atmos9050184

Orr, J. C., Najjar, R. G., Aumont, O., Bopp, L., Bullister, J. L., Danabasoglu, G., Doney, S. C., Dunne, J. P., Dutay, J.-C., Graven, H., Griffies, S. M., John, J. G., Joos, F., Levin, I., Lindsay, K., Matear, R. J., McKinley, G. A., Mouchet, A., Oschlies, A., Romanou, A., Schlitzer, R., Tagliabue, A., Tanhua, T., and Yool, A.: Biogeochemical protocols and diagnostics for the CMIP6 Ocean Model Intercomparison Project (OMIP), 10, 2169–2199, https://doi.org/10.5194/gmd-10-2169-2017, 2017.

Ortega, P., E. Guilyardi, D. Swingedouw, J. Mignot, and S. Nguyen: Reconstructing extreme amoc events through nudging of the ocean surface: a perfect model approach. Climate Dynamics, 49 (9), 3425–3441, 2017.

Peters, G. P., Andrew, R., and Lennox, J.: Constructing an environmentally-extended multi-regional input–output table using the GTAP database, Economic Systems Research, 23, 131–152, https://doi.org/10.1080/09535314.2011.563234, 2011b.

Peters, G. P., Davis, S. J., and Andrew, R.: A synthesis of carbon in international trade, Biogeosciences, 9, 3247–3276, https://doi.org/10.5194/bg-9-3247-2012, 2012b.

Pongratz, J., Smith, S. M., Schwingshackl, C., Dayathilake, L., Gasser, T., Grassi, G. and Pilli, R.: Chapter 7: Current levels of CDR. in The State of Carbon Dioxide Removal 2024 – 2nd Edition, https://doi.org/10.17605/OSF.IOZXSKB, 2024.

Poorter, H., Niklas, K. J., Reich, P. B., Oleksyn, J., Poot, P., & Mommer, L. (2012): Biomass allocation to leaves, stems and roots: meta-analyses of interspecific variation and environmental control. New Phytologist, 193, 30–50. https://doi.org/10.1111/j.1469-8137.2011.03952.x

Potapov, P., Hansen, M. C., Laestadius, L., Turubanova, S., Yaroshenko, A., Thies, C., Smith, W., Zhuravleva, I., Komarova, A., Minnemeyer, S., and Esipova, E.: The last frontiers of wilderness: Tracking loss of intact forest landscapes from 2000 to 2013, Sci. Adv., 3, e1600821, https://doi.org/10.1126/sciadv.1600821, 2017.

Poulter, B., Freeborn, P. H., Jolly, W. M., and Varner, J. M.: COVID-19 lockdowns drive decline in active fires in southeastern United States, PNAS, 118, e2105666118, https://doi.org/10.1073/pnas.2105666118, 2021.

Prather, M.: Interactive comment on "Carbon dioxide and climate impulse response functions for the computation of greenhouse gas metrics: a multi-model analysis" by F. Joos et al., Atmospheric Chem. Phys. Discuss., 12, C8465, 2012.

Prosperi, P., Bloise, M., Tubiello, F. N., Conchedda, G., Rossi, S., Boschetti, L., Salvatore, M., and Bernoux, M.: New estimates of greenhouse gas emissions from biomass burning and peat fires using MODIS Collection 6 burned areas, Climatic Change, 161, 415–432, https://doi.org/10.1007/s10584-020-02654-0, 2020.

Qin, Z., Zhu, Y., Canadell, J.G., Chen, M., Li, T., Mishra, U. and Yuan, W.: Global spatially explicit carbon emissions from land-use change over the past six decades (1961–2020). One Earth, 7(5), pp.835-847, 2024.

Qiu, C., Ciais, P., Zhu, D., Guenet, B., Peng, S., Petrescu, A. M. R., Lauerwald, R., Makowski, D., Gallego-Sala, A. V., Charman, D. J., and Brewer, S. C.: Large historical carbon emissions from cultivated northern peatlands, Sci. Adv., 7, eabf1332, https://doi.org/10.1126/sciadv.abf1332, 2021.

Raich, J.W., Potter, C.S. and Bhagawati, D.: Interannual variability in global soil respiration, 1980–94. Global Change Biology, 8(8), pp.800-812, 2002.

Rayner, N. A., Parker, D. E., Horton, E. B., Folland, C. K., Alexander, L. V., Rowell, D. P., Kent, E. C., and Kaplan, A.: Global analyses of sea surface temperature, sea ice, and night marine air temperature since the late nineteenth century, Journal of Geophysical Research: Atmospheres, 108, https://doi.org/10.1029/2002JD002670, 2003.

Rayner, P. J., Enting, I. G., Francey, R. J., and Langenfelds, R.: Reconstructing the recent carbon cycle from atmospheric CO2, δ13C and O2/N2 observations*, Tellus B, 51, 213–232, https://doi.org/10.1034/j.1600-0889.1999.t01-1-00008.x, 1999.

Reagan, J.R., D. Seidov, Z. Wang, D. Dukhovskoy, T.P. Boyer, R.A. Locarnini, O.K. Baranova, A.V. Mishonov, H.E. Garcia, C. Bouchard, S.L. Cross, and C.R. Paver. World Ocean Atlas 2023, Volume 2: Salinity. A. Mishonov, Technical Editor, NOAA Atlas NESDIS 90, doi.org/10.25923/70qt-9574

Regnier, P., Friedlingstein, P., Ciais, P., Mackenzie, F. T., Gruber, N., Janssens, I. A., Laruelle, G. G., Lauerwald, R., Luyssaert, S., Andersson, A. J., Arndt, S., Arnosti, C., Borges, A. V., Dale, A. W., Gallego-Sala, A., Goddéris, Y., Goossens, N., Hartmann, J., Heinze, C., Ilyina, T., Joos, F., LaRowe, D. E., Leifeld, J., Meysman, F. J. R., Munhoven, G., Raymond, P. A., Spahni, R., Suntharalingam, P., and Thullner, M.: Anthropogenic perturbation of the carbon fluxes from land to ocean, Nature Geosci, 6, 597–607, https://doi.org/10.1038/ngeo1830, 2013.

Reichstein, M., Papale, D., Valentini, R., Aubinet, M., Bernhofer, C., Knohl, A., Laurila, T., Lindroth, A., Moors, E., Pilegaard, K., and Seufert, G.: Determinants of terrestrial ecosystem carbon balance inferred from European eddy covariance flux sites, Geophys. Res. Lett., 34, L01402, https://doi.org/10.1029/2006GL027880, 2007.

Rhein, M., Rintoul, S. R., Aoki, S., Campos, E., Chambers, D., Feely, R. A., Gulev, S., Johnson, G. C., Josey, S. A., Kostianoy, A., Mauritzen, C., Roemmich, D., and Talley, L. D.: Observations: Ocean, in: Climate Change 2013: The Physical Science Basis. Contribution of Working Group I to the Fifth Assessment Report of the Intergovernmental Panel on Climate Change [Stocker, T. F., Qin, D., Plattner, G.-K., Tignor, M., Allen, S. K., Boschung, J., Nauels, A., Xia, Y., Bex, V., and Midgley, P. M. (eds.)], Cambridge University Press, 255–316, ISBN: 9781107057991, 2013.

Rödenbeck, C., Bakker, D. C. E., Gruber, N., Iida, Y., Jacobson, A. R., Jones, S., Landschützer, P., Metzl, N., Nakaoka, S., Olsen, A., Park, G.-H., Peylin, P., Rodgers, K. B., Sasse, T. P., Schuster, U., Shutler, J. D., Valsala, V., Wanninkhof, R., and Zeng, J.: Data-based estimates of the ocean carbon sink variability – first results of the Surface Ocean CO2 Mapping intercomparison (SOCOM), Biogeosciences, 12, 7251–7278, https://doi.org/10.5194/bg-12-7251-2015, 2015.

Rödenbeck, C., DeVries, T., Hauck, J., Le Quéré, C., and Keeling, R. F.: Data-based estimates of interannual sea–air CO2 flux variations 1957–2020 and their relation to environmental drivers, Biogeosciences, 19, 2627–2652, https://doi.org/10.5194/bg-19-2627-2022, 2022.

Roobaert, A., Laruelle, G. G., Landschützer, P., and Regnier, P.: Uncertainty in the global oceanic CO2 uptake induced by wind forcing: quantification and spatial analysis, 15, 1701–1720, https://doi.org/10.5194/bg-15-1701-2018, 2018.

Rossi, S., Brandão De Melo, J., Ceccherini, G., Alkama, R., and Grassi, G. JRC global proxy maps of managed and unmanaged forest (Version 1.0). Zenodo. https://doi.org/10.5281/zenodo.14549036. 2024.

Rypdal, K., Paciornik, N., Eggleston, S., Goodwin, J., Irving, W., Penman, J., and Woodfield, M.: Volume 1: Introduction to the 2006 Guidelines in: 2006 IPCC guidelines for national greenhouse gas inventories, available at: https://www.ipcc-nggip.iges.or.jp/public/2006gl/vol1.html, last access: 21 January 2025, 2006.

Saatchi, S. S., Harris, N. L., Brown, S., Lefsky, M., Mitchard, E. T. A., Salas, W., Zutta, B. R., Buermann, W., Lewis, S. L., Hagen, S., Petrova, S., White, L., Silman, M., and Morel, A.: Benchmark map of forest carbon stocks in tropical regions across three continents, Proceedings of the National Academy of Sciences, 108, 9899–9904, https://doi.org/10.1073/pnas.1019576108, 2011.

Sallée, JB., Pellichero, V., Akhoudas, C. et al. Summertime increases in upper-ocean stratification and mixed-layer depth. Nature 591, 592–598 (2021). https://doi.org/10.1038/s41586-021-03303-x

Santoro, M., and Cartus, O. (2021) ESA Biomass Climate Change Initiative (Biomass_cci): Global datasets of forest above-ground biomass for the years 2010, 2017 and 2018, v3, NERC EDS Centre for Environmental Data Analysis, http://dx.doi.org/10.5285/5f331c418e9f4935b8eb1b836f8a91b8

Santoro, M., Cartus, O., Quegan, S., Kay H., Lucas, R. M., Araza, A., Herold, M., Labrière, N., Chave, J., Rosenqvist, Å., Tadono, T., Kobayashi, K., Kellndorfer, J., Avitabile, V., Brown, H., Carreiras, J., Campbell, M. J., Cavlovic, J., Conceição Bispo, P., Gilani, H., Khan, M. L., Kumar, A., Lewis, S. L., Jingjing Liang, J., Mitchard, E. T. A., Pacheco-Pascagaza, A. M., Phillips, O. L., Ryan, C. M., Saikia, P., Schepaschenko, D., Sukhdeo, H., Verbeeck, H., Vieilledent, G., Wijaya, A., Willcock, S. and Seifert, F.M. (2024) Design and performance of the Climate Change Initiative Biomass global retrieval algorithm. Science of Remote Sensing. https://doi.org/10.1016/j.srs.2024.100169

Sarmiento, J. L., Orr, J. C., and Siegenthaler, U.: A perturbation simulation of CO2 uptake in an ocean general circulation model, J. Geophys. Res.-Oceans., 97, 3621–3645, https://doi.org/10.1029/91JC02849, 1992.

Sato, M., Hansen, J. E., McCormick, M. P., and Pollack, J. B.: Stratospheric aerosol optical depths, 1850–1990, Geophys. Res.-Atmos., 98, 22987–22994, https://doi.org/10.1029/93JD02553, 1993.

Saunois, M., Stavert, A. R., Poulter, B., Bousquet, P., Canadell, J. G., Jackson, R. B., Raymond, P. A., Dlugokencky, E. J., Houweling, S., Patra, P. K., Ciais, P., Arora, V. K., Bastviken, D., Bergamaschi, P., Blake, D. R., Brailsford, G., Bruhwiler, L., Carlson, K. M., Carrol, M., Castaldi, S., Chandra, N., Crevoisier, C., Crill, P. M., Covey, K., Curry, C. L., Etiope, G., Frankenberg, C., Gedney, N., Hegglin, M. I., Höglund-Isaksson, L., Hugelius, G., Ishizawa, M., Ito, A., Janssens-Maenhout, G., Jensen, K. M., Joos, F., Kleinen, T., Krummel, P. B., Langenfelds, R. L., Laruelle, G. G., Liu, L., Machida, T., Maksyutov, S., McDonald, K. C., McNorton, J., Miller, P. A., Melton, J. R., Morino, I., Müller, J., Murguia-Flores, F., Naik, V., Niwa, Y., Noce, S., O'Doherty, S., Parker, R. J., Peng, C., Peng, S., Peters, G. P., Prigent, C., Prinn, R., Ramonet, M., Regnier, P., Riley, W. J., Rosentreter, J. A., Segers, A., Simpson, I. J., Shi, H., Smith, S. J., Steele, L. P., Thornton, B. F., Tian, H., Tohjima, Y., Tubiello, F. N., Tsuruta, A., Viovy, N., Voulgarakis, A., Weber, T. S., van Weele, M., van der Werf, G. R., Weiss, R. F., Worthy, D., Wunch, D., Yin, Y., Yoshida, Y., Zhang, W., Zhang, Z., Zhao, Y., Zheng, B., Zhu, Q., Zhu, Q., and Zhuang, Q.: The Global Methane Budget 2000–2017, Earth Syst. Sci. Data, 12, 1561–1623, https://doi.org/10.5194/essd-12-1561-2020, 2020.

Schuldt, K. N., Mund, J., Aalto, T., Abshire, J. B., Aikin, K., Allen, G., Andrews, A., Apadula, F., Arnold, S., Baier, B., Bakwin, P., Bartyzel, J., Bentz, G., Bergamaschi, P., Beyersdorf, A., Biermann, T., Biraud, S. C., Blanc, P.-E., Boenisch, H., Bowling, D., Brailsford, G., Brand, W. A., Brunner, D., Bui, T. P., Bäni, L., Calzolari, F., Chang, C. S., Chen, H., Chen, G., Chmura, L., Clark, S., Climadat, S., Colomb, A., Commane, R., Conen, F., Conil, S., Couret, C., Cristofanelli, P., Cuevas, E., Curcoll, R., Daube, B., Davis, K. J., De Mazière, M., De Wekker, S., Dean-Day, J. M., Della Coletta, J., Delmotte, M., Di Iorio, T., DiGangi, E., DiGangi, J. P., Elkins, J. W., Elsasser, M., Emmenegger, L., Fang, S., Fischer, M. L., Forster, G., France, J., Frumau, A., Fuente-Lastra, M., Galkowski, M., Gatti, L. V., Gehrlein, T., Gerbig, C., Gheusi, F., Gloor, E., Goto, D., Griffis, T., Hammer, S., Hanisco, T. F., Hanson, C., Haszpra, L., Hatakka, J., Heimann, M., Heliasz, M., Heltai, D., Henne, S., Hensen, A., Hermans, C., Hermansen, O., Hintsa, E., Hoheisel, A., Holst, J., Iraci, L. T., Ivakhov, V., Jaffe, D. A., Jordan, A., Joubert, W., Karion, A., Kawa, S. R., Kazan, V., Keeling, R. F., Keronen, P., Kim, J., Klausen, J., Kneuer, T., Kolari, P., Kominkova, K., Kort, E., Kozlova, E., Krummel, P. B., Kubistin, D., Kulawik, S. S., Kumps, N., Labuschagne, C., Lam, D. H., Lan, X., Langenfelds, R. L., Lanza, A., Laurent, O., Laurila, T., Lauvaux, T., Lavric, J., Law, B. E., Lee, J., Lehner, I., Lehtinen, K., Leppert, R., Leskinen, A., Leuenberger, M., Leung, W. H., Levin, I., Levula, J., Lin, J., Lindauer, M., Lindroth, A., Loh, Z. M., Lopez, M., Lunder, C. R., Löfvenius, M. O., Machida, T., Mammarella, I., Manca, G., Manning, A., Manning, A., Marek, M. V., Marklund, P., Marrero, J. E., Martin, D., Martin, M. Y., Martins, G. A., Matsueda, H., McKain, K., Meijer, H., Meinhardt, F., Merchant, L., Metzger, J.-M., Mihalopoulos, N., Miles, N. L., Miller, J. B., Miller, C. E., Mitchell, L., Monteiro, V., Montzka, S., Moore, F., Moossen, H., Morgan, E., Morgui, J.-A., Morimoto, S., Munger, J. W., Munro, D., Mutuku, M., Myhre, C. L., Mölder, M., Müller-Williams, J., Necki, J., Newman, S., Nichol, S., Nisbet, E., Niwa, Y., Njiru, D. M., Noe, S. M., Nojiri, Y., O'Doherty, S., Obersteiner, F., Paplawsky, B., Parworth, C. L., Peischl, J., Peltola, O., Peters, W., Philippon, C., Piacentino, S., Pichon, J. M., Pickers, P., Piper, S., Pitt, J., Plass-Dülmer, C., Platt, S. M., Prinzivalli, S., Ramonet, M., Ramos, R., Reyes-Sanchez, E., Richardson, S. J., Rigouleau, L.-J., Riris, H., Rivas, P. P., Rothe, M., Roulet, Y.-A., Ryerson, T., Ryoo, J.-M., Sargent, M., Sasakawa, M., Scheeren, B., Schmidt, M., Schuck, T., Schumacher, M., Seibel, J., Seifert, T., Sha, M. K., Shepson, P., Shook, M., Sloop, C. D., Smith, P. D., Spain, G., St. Clair, J. M., Steger, D., Steinbacher, M., Stephens, B., Sweeney, C., Sørensen, L. L., Taipale, R., Takatsuji, S., Tans, P., Thoning, K., Timas, H., Torn, M., Trisolino, P., Turnbull, J., Vermeulen, A., Viner, B., Vitkova, G., Walker, S., Watson, A., Weiss, R., Weyrauch, D., Wofsy, S. C., Worsey, J., Worthy, D., Xueref-Remy, I., Yates, E. L., Young, D., Yver-Kwok, C., Zaehle, S., Zahn, A., Zellweger, C., Zimnoch, M., de Souza, R. A., di Sarra, A. G., van Dinther, D., and van den Bulk, P. (2023) Multi-laboratory compilation of atmospheric carbon dioxide data for the period 1957-2022; obspack_co2_1_GLOBALVIEWplus_v9.0_2023-09-09; NOAA Earth System Research Laboratory, Global Monitoring Laboratory. http://doi.org/10.25925/20230801.

Schuldt, K. N., Jacobson, A. R., Aalto, T., Andrews, A., Apadula, F., Arnold, S., Bakwin, P., Bartyzel, J., Bergamaschi, P., Biermann, T., Biraud, S. C., Blanc, P.-E., Bäni, L., Calzolari, F., Chen, H., Chmura, L., Colomb, A., Condori, L., Conen, F., Conil, S., Couret, C., Cristofanelli, P., Cuevas, E., De Mazière, M., De Wekker, S., Della Coletta, J., Delmotte, M., Di Iorio,

T., Elsasser, M., Emmenegger, L., Fischer, M. L., Forster, G., Frumau, A., Fuente-Lastra, M., Galkowski, M., Gheusi, F., Hammer, S., Hatakka, J., Heliasz, M., Heltai, D., Hensen, A., Hermans, C., Hermansen, O., Hoheisel, A., Holst, J., Jaffe, D. A., Karion, A., Kazan, V., Keronen, P., Kneuer, T., Kolari, P., Kominkova, K., Krummel, P. B., Kubistin, D., Kumps, N., Lan, X., Langenfelds, R. L., Lanza, A., Laurent, O., Laurila, T., Lee, J., Lehner, I., Lehtinen, K., Leskinen, A., Leuenberger, M., Levin, I., Levula, J., Lindauer, M., Lindroth, A., Loh, Z. M., Lopez, M., Lunder, C. R., Löfvenius, M. O., Mammarella, I., Manca, G., Manning, A., Manning, A., Marek, M. V., Marklund, P., McKain, K., Meijer, H., Meinhardt, F., Metzger, J.-M., Miller, C. E., Miller, J. B., Myhre, C. L., Mölder, M., Müller-Williams, J., Necki, J., O'Doherty, S., Peltola, O., Philippon, C., Piacentino, S., Pichon, J. M., Pickers, P., Pitt, J., Plass-Dülmer, C., Platt, S. M., Ramonet, M., Ramos, R., Reyes-Sanchez, E., Rigouleau, L.-J., Rivas, P. P., Roulet, Y.-A., Scheeren, B., Schmidt, M., Schumacher, M., Sha, M. K., Sloop, C. D., Smith, P. D., Steger, D., Steinbacher, M., Sweeney, C., Sørensen, L. L., Taipale, R., Tans, P., Thoning, K., Trisolino, P., Turnbull, J., Vermeulen, A., Viner, B., Vitkova, G., Weyrauch, D., Worthy, D., Xueref-Remy, I., Young, D., Yver-Kwok, C., Zimnoch, M., di Sarra, A. G., van Dinther, D., and van den Bulk, P. (2024) Multi-laboratory compilation of atmospheric carbon dioxide data for the period 2023-2024; obspack_co2_1_NRT_v9.2_2024-03-25; NOAA Earth System Research Laboratory, Global Monitoring Laboratory. http://doi.org/10.25925/20240215.

Sharp, J. D., Pierrot, D., Humphreys, M. P., Epitalon, J.-M., Orr, J. C., Lewis, E. R., and Wallace, D. W. R.: CO2SYSv3 for MATLAB, , https://doi.org/10.5281/ZENODO.3950563, 2020.

Smith, T. M., Reynolds, R. W., Peterson, T. C., & Lawrimore, J.: Improvements to NOAA's historical merged land–ocean surface temperature analysis (1880–2006). Journal of climate, 21(10), 2283-2296, 2008.

Sospedra-Alfonso, R., W. J. Merryfield, G. J. Boer, V. V. Kharin, W.-S. Lee, C. Seiler, and J. R. Christian: Decadal climate predictions with the canadian earth system model version 5 (canesm5). Geoscientific Model Development, 14 (11), 6863–6891, 2021.

Souza, C. M., Z. Shimbo, J., Rosa, M. R., Parente, L. L., A. Alencar, A., Rudorff, B. F. T., Hasenack, H., Matsumoto, M., G. Ferreira, L., Souza-Filho, P. W. M., de Oliveira, S. W., Rocha, W. F., Fonseca, A. V., Marques, C. B., Diniz, C. G., Costa, D., Monteiro, D., Rosa, E. R., Vélez-Martin, E., Weber, E. J., Lenti, F. E. B., Paternost, F. F., Pareyn, F. G. C., Siqueira, J. V., Viera, J. L., Neto, L. C. F., Saraiva, M. M., Sales, M. H., Salgado, M. P. G., Vasconcelos, R., Galano, S., Mesquita, V. V., and Azevedo, T.: Reconstructing Three Decades of Land Use and Land Cover Changes in Brazilian Biomes with Landsat Archive and Earth Engine, Remote Sens., 12, 2735, https://doi.org/10.3390/rs12172735, 2020.

Steinhoff, T., Gkritzalis, T., Jones, S., Macovei, V.A., Neill, C., Schuster, U., Akl, J., Arruda, R., Atamanchuk, D., Barry, M., Beaumont, L., Cantoni, C., Dickson, A., Fahning, J., Fought, J., Frangoulis, C., Gutiérrez-Loza, L., Hagan, C., Honkanen, M., Kielosto, S., Kinski, N., Körtzinger, A., Landschützer, P., Lauvset, S.K., Lawrence-Slavas, N., Li, Q., Luchetta, A., Malarde, D., Paulsen, M., Ritschel, M., Rutgersson, A., Sanders, R., Shitashima, K., Spaulding, R., Stamataki, N., Stenbäck, K., Sutton, A., Tatkiewicz, W., Telszewski, M., Theetaert, H., Tilbrook, B., Wanninkhof, R.: The ICOS OTC pCO_2 instrument intercomparison. Limnology and Oceanography: Methods, 1-66, http://doi.org/10.1002/lom3.10727, 2025.

Swart, N. C. et al.: The Canadian Earth System Model version 5 (CanESM5. 0.3). Geoscientific Model Development, 12 (11), 4823–4873, 2019.

Tang, X., Fan, S., Zhang, W., Gao, S., Chen, G. and Shi, L.: Global variability in belowground autotrophic respiration in terrestrial ecosystems. Earth System Science Data, 11(4), pp.1839-1852, 2019.

Tang, X., Fan, S., Du, M., Zhang, W., Gao, S., Liu, S., Chen, G., Yu, Z. and Yang, W., 2020. Spatial and temporal patterns of global soil heterotrophic respiration in terrestrial ecosystems. Earth System Science Data, 12(2), pp.1037-1051.

Tatebe, H. et al.: The initialization of the MIROC climate models with hydrographic data assimilation for decadal prediction. Journal of Meteorological Society of Japan, 90A, 275–294, 2012.

Thomason, L. W., Ernest, N., Millán, L., Rieger, L., Bourassa, A., Vernier, J.-P., Manney, G., Luo, B., Arfeuille, F., and Peter, T.: A global space-based stratospheric aerosol climatology: 1979–2016, 10, 469–492, https://doi.org/10.5194/essd-10-469-2018, 2018.

Thurner, M., Beer, C., Santoro, M., Carvalhais, N., Wutzler, T., Schepaschenko, D., Shvidenko, A., Kompter, E., Ahrens, B., Levick, S. R., and Schmullius, C.: Carbon stock and density of northern boreal and temperate forests, Global Ecology and Biogeography, 23, 297–310, https://doi.org/10.1111/geb.12125, 2014.

Tian, H., Yao, Y., Li, Y., Shi, H., Pan, S., Najjar, R. G., Pan, N., Bian, Z., Ciais, P., Cai, W., Dai, M., Friedrichs, M. A. M., Li, H., Lohrenz, S., and Leung, L. R.: Increased Terrestrial Carbon Export and CO2 Evasion From Global Inland Waters Since the Preindustrial Era, Global Biogeochemical Cycles, 37, e2023GB007776, https://doi.org/10.1029/2023GB007776, 2023.

Tohjima, Y., Mukai, H., Machida, T., Hoshina, Y., and Nakaoka, S.-I.: Global carbon budgets estimated from atmospheric O2/N2 and CO2 observations in the western Pacific region over a 15-year period, 19, 9269–9285, https://doi.org/10.5194/acp-19-9269-2019, 2019.

Tramontana, G., Jung, M., Schwalm, C. R., Ichii, K., Camps-Valls, G., Ráduly, B., Reichstein, M., Arain, M. A., Cescatti, A., Kiely, G., Merbold, L., Serrano-Ortiz, P., Sickert, S., Wolf, S., and Papale, D.: Predicting carbon dioxide and energy fluxes across global FLUXNET sites withregression algorithms, Biogeosciences, 13, 4291–4313, https://doi.org/10.5194/bg-13-4291-2016, 2016.

Tubiello, F., Pekkarinen, A., Branthomme, A., Piccoli, M., Obli-Laryea, G., Ramadan, N., and Conchedda, G.: New FAOSTAT forest emissions and removals estimates: 1990–2025, Earth Syst. Sci. Data Discuss. [preprint], https://doi.org/10.5194/essd-2025-635, in review, 2025.

UN: United Nations Statistics Division: National Accounts Main Aggregates Database, available at: http://unstats.un.org/unsd/snaama/Introduction.asp, last access: 21 January 2025, 2021.

Uppala, S. M., Kållberg, P. W., Simmons, A. J., Andrae, U., Bechtold, V. D. C., Fiorino, M., ... & Woollen, J.: The ERA-40 re-analysis. Quarterly Journal of the Royal Meteorological Society: A journal of the atmospheric sciences, applied meteorology and physical oceanography, 131(612), 2961-3012, 2005.

van der Werf, G. R., Randerson, J. T., Giglio, L., van Leeuwen, T. T., Chen, Y., Rogers, B. M., Mu, M., van Marle, M. J. E., Morton, D. C., Collatz, G. J., Yokelson, R. J., and Kasibhatla, P. S.: Global fire emissions estimates during 1997–2016, Earth Syst. Sci. Data, 9, 697–720, https://doi.org/10.5194/essd-9-697-2017, 2017

Vermote, E. and NOAA CDR Program: NOAA Climate Data Record (CDR) of AVHRR Leaf Area Index (LAI) and Fraction of Absorbed Photosynthetically Active Radiation (FAPAR), Version 5, https://doi.org/10.7289/V5TT4P69, 2018.

Viovy, N.: CRUNCEP data set, available at: ftp://nacp.ornl.gov/synthesis/2009/frescati/temp/land_use_change/original/readme.htm, last access: 21 January 2025, 2016.

Wanninkhof, R.: Relationship between wind speed and gas exchange over the ocean, J. Geophys. Res.-Oceans., 97, 7373–7382, https://doi.org/10.1029/92JC00188, 1992.

Wanninkhof, R.: Relationship between wind speed and gas exchange over the ocean revisited, Limnol. Oceanogr. Methods., 12, 351–362, https://doi.org/10.4319/lom.2014.12.351, 2014.

Wanninkhof, R., Park, G.-H., Takahashi, T., Sweeney, C., Feely, R., Nojiri, Y., Gruber, N., Doney, S. C., McKinley, G. A., Lenton, A., Le Quéré, C., Heinze, C., Schwinger, J., Graven, H., and Khatiwala, S.: Global ocean carbon uptake: magnitude, variability and trends, Biogeosciences, 10, 1983–2000, https://doi.org/10.5194/bg-10-1983-2013, 2013.

Watanabe, M., H. Tatebe, H. Koyama, T. Hajima, M. Watanabe, and M. Kawamiya: Importance of El Nĩ no reproducibility for reconstructing historical CO2 flux variations in the equatorial Pacific. Ocean Science, 16, 1431–1442, 2020.

Weiss, R. F. and Price, B. A.: Nitrous oxide solubility in water and seawater, Marine Chemistry, 8, 347–359, https://doi.org/10.1016/0304-4203(80)90024-9, 1980.

Woolf, D. K., P. E. Land, J. D. Shutler, L. M. Goddijn-Murphy, and C. J. Donlon: On the calculation of air-sea fluxes of CO2 in the presence of temperature and salinity gradients, J. Geophys. Res. Oceans, 121, 1229–1248, https://doi.org/10.1002/2015JC011427, 2016.

Xia, J., Chen, Y., Liang, S., Liu, D., and Yuan, W.: Global simulations of carbon allocation coefficients for deciduous vegetation types, Tellus B, 67, 28016, https://doi.org/10.3402/tellusb.v67.28016, 2015.

Xu, L., Saatchi, S.S., Yang, Y., Yu, Y., Pongratz, J., Bloom, A.A., Bowman, K., Worden, J., Liu, J., Yin, Y., Domke, G., McRoberts, R.E., Woodall, C., Nabuurs, G.-J., de-Miguel, S., Keller, M., Harris, N., Maxwell, S., & Schimel, D. (2021), Zenodo, doi:10.5281/zenodo.4161694

Yu, Z., Ciais, P., Piao, S., Houghton, R. A., Lu, C., Tian, H., Agathokleous, E., Kattel, G. R., Sitch, S., Goll, D., Yue, X., Walker, A., Friedlingstein, P., Jain, A. K., Liu, S., and Zhou, G.: Forest expansion dominates China's land carbon sink since 1980, Nat. Commun., 13, 5374, https://doi.org/10.1038/s41467-022-32961-2, 2022.

Zeng, J., Nojiri, Y., Landschützer, P., Telszewski, M., and Nakaoka, S.-I.: A global surface ocean fCO2 climatology based on a feed forward neural network, J. Atmos. Ocean. Tech., 31, 1838–1849, https://doi.org/10.1175/JTECH-D-13-00137.1, 2014.

Zeng J., Matsunaga T., Tan Z-H., Saigusa N., Shirai T., Tang Y., Peng S. and Fukuda Y.: Global terrestrial carbon fluxes of 1999–2019 estimated by upscaling eddy covariance data with a random forest, Sci. Data, 7, 1–11, https://doi.org/10.1038/s41597-020-00653-5, 2020.

Zheng, B., Chevallier, F., Yin, Y., Ciais, P., Fortems-Cheiney, A., Deeter, M. N., Parker, R. J., Wang, Y., Worden, H. M., and Zhao, Y.: Global atmospheric carbon monoxide budget 2000–2017 inferred from multi-species atmospheric inversions, Earth Syst. Sci. Data, 11, 1411–1436, https://doi.org/10.5194/essd-11-1411-2019, 2019.

Zuo, H., Balmaseda, M. A., Tietsche, S., Mogensen, K., & Mayer, M.: The ECMWF operational ensemble reanalysis–analysis system for ocean and sea ice: a description of the system and assessment. Ocean science, 15(3), 779-808, 2019.